

LIBRARY Michigan State University

This is to certify that the dissertation entitled

GENERALIZED FINITE ELEMENT METHOD FOR ELECTROMAGNETIC ANALYSIS

presented by

Chuan Lu

has been accepted towards fulfillment of the requirements for the

Ph	. D.	degree in	Electrical and Computer Engineering
		Shark	ß
•		Major Pro	fessor's Signature
		0	2-04-2008
			Date

MSU is an affirmative-action, equal-opportunity employer

PLACE IN RETURN BOX to remove this checkout from your record.

TO AVOID FINES return on or before date due.

MAY BE RECALLED with earlier due date if requested.

DATE DUE	DATE DUE	DATE DUE

5/08 K:/Proj/Acc&Pres/CIRC/DateDue indd

GENERALIZED FINITE ELEMENT METHOD FOR ELECTROMAGNETIC ANALYSIS

 $\mathbf{B}\mathbf{y}$

Chuan Lu

A DISSERTATION

Submitted to
Michigan State University
in partial fulfillment of the requirements
for the degree of

DOCTOR OF PHILOSOPHY

Electrical and Computer Engineering

2008

ABSTRACT

GENERALIZED FINITE ELEMENT METHOD FOR ELECTROMAGNETIC ANALYSIS

By

Chuan Lu

The generalized finite element method (GFEM), first introduced by Babuska, is a partition of unity-based solver for scalar partial differential equations (PDEs). To date, they have been applied extensively to the solution of elliptic and parabolic PDEs. This technique is a generalization of a host of well known methods for solving PDEs, specially the classical finite element method(FEM), element free galerkin(EFG), hp clouds, etc. The main goal of this dissertation is for developing a similar methodology for vector electromagnetic problems. Developing a solution to these problems necessitates addressing the following problems: (i) The vector nature of the problem and the different continuity requirements on each component imply that basis functions developed should share similar characteristics; (ii) The basis functions have to be able to represent divergence free electromagnetic fields (in a source free region). (iii) Development of appropriate boundary conditions to truncate the computational domain is necessary. (iv) High condition number of the resulting system also plagues GFEM solver, as it does other high order solvers. Solution to these problems, and the developments of the GFEM solver is presented here for both time and frequency domains. In any case, the h- and p- convergence of the method is presented.

To My Dear Parents

ACKNOWLEDGMENTS

I'd like to take this opportunity to express my gratitude to all my friends and colleagues who helped me to complete this dissertation and who have played important roles in my life at Michigan State University.

At first, I should thank my parents for your continuous and unconditional support for my life and study since childhood. Especially in the last few months you take care of my daily life and help me concentrate on my work.

I like to thank my advisor, Dr. Shanker Balasubramaniam, for leading me to this interesting research area. You taught me every skills useful for the project; you helped and encouraged me with open-minded discussion and creative ideas; you also helped me improve my presentation and writing skills. In four years in this group, I have grown up from a student with little electromagnetic background and poor English to an experienced researcher with skills necessary for a successful career. It would have been impossible without your help and continuously pushing me to be better.

Thanks to Dr. Leo Kempel for your valuable suggestion in group discussion and your contribution to HPC system, which is very helpful for my research. Thanks to Dr. Nyquist for your reviewing my research in group meeting and comprehensive exam. Thanks to Dr. Guowei Wei for giving me suggestion for my career. Thanks to Dr. Edward Rothwell for consolidating my background and theory in advanced electromagnetics research, your book was crucial for portion of my research. Special thanks to Dr. Satish and Dr. Lalita for taking care of my research and study in my first year in US.

A thank you also goes to my teammates, Jun Gao, Jun Yuan, He Huang, Gregory Kobidze, Tuncer Ozgur, Naveen Nair and Vikram Reddy, Jorge M. Villa, Carlos A. Jaramillo and Pedro Barba. I am always happy to discuss with you and learn a great deal from it. You are one reason I like being in the office. It's also exciting to have dinner, play table tennis and practice with you together.

TABLE OF CONTENTS

LIST O	F FIGURES	iii
LIST O	F TABLES	xi
KEY TO	O SYMBOLS AND ABBREVIATIONS	cii
CHAPT Introduc	ER 1	1
CHAPT Scalar C	ER 2 Generalized Finite Element Method	8
2.1		8
2.2	Basic framework of GFEM solver	10 10 17
2.3	2.3.1 Neumann Boundary Condition:	20 21 21 24 28
2.4	Numerical experiments	29
CHAPT Vector (49
3.1		-0 49
3.2	GFEM solver for homogeneous domain	51 52 57 64
3.3	GFEM solver for piecewise homogeneous domain with flat interface . 3.3.1 Basis function	78 78 83 84
3.4		87 87 95
3.5	Overcoming linear dependence and condition number issues)5

CHAPT	TER 4
Time de	omain Generalized Finite Element Method
4.1	Introduction
4.2	Formulation for Time domain GFEM solver
4.3	Analysis of stability
4.4	Iterative Solver
4.5	Numerical Experiments
CHAPT Conclus	ER 5 ion and areas for future work

LIST OF FIGURES

Figure 1.1	Meshes for FEM	1
Figure 2.1	Construction of the computational domain	12
Figure 2.2	One dimensional partition of unity function.	15
Figure 2.3	Construction of one dimensional Basis function.	16
Figure 2.4	Subdivision of the domain of integration based on piecewise weight function W_i	17
Figure 2.5	Subdivision of D^n_{ij} based on the number of patches at different location	18
Figure 2.6	Integration in the sub-patch E_{ij}^n that overlaps with boundary of computation domain Γ	19
Figure 2.7	Geometry transform	20
Figure 2.8	(a) Definition of geometry for imposing the boundary integral; (b) Definition of the geometry for application of the PML	25
Figure 2.9	Error in the L_2 norm of the numerical and analytical solutions of the PDE with the Neumann boundary condition	31
Figure 2.10	h,p convergence of the numerical scheme applied to the solution of a PDE with Neumann boundary conditions	31
Figure 2.11	Error in the L_2 norm of the numerical and analytical solutions of the PDE with the Dirichlet boundary condition	32
Figure 2.12	h,p convergence of the numerical scheme applied to the solution of a PDE with Dirichlet boundary condition	32
Figure 2.13	h,p convergence of GFEM-BI (CFIE)	35
Figure 2.14	Error in E-field over a range of ka with GFEM-BI (EFIE)	38
Figure 2.15	Error in E-field over a range of ka with GFEM-BI (CFIE)	38
Figure 2.16	Comparison between numerical and analytical data obtained for scattering from a perfectly conducting cylinder of radius 2.7 λ : (a) the electric field at Γ_e ; (b) Echo-width of the cylinder	39
Figure 2.17	Comparison between numerical and analytical data obtained for scattering from the coated perfectly conducting cylinder if radius 2.88 λ : (a) the electric field at Γ_e ; (b) Echo-width of the cylinder.	40
Figure 2.18	Comparison between numerical and analytical data obtained for scattering from a coated perfectly conducting cylinder of radius 3.84 λ : (a) the electric field at Γ_e ; (b) Echo-width	41
Figure 2.19	Comparison of data obtained for scattering from an L-shaped object using GFEM-BI and GFEM-PML.	42
Figure 2.20	Geometric description of the wedge	43

Figure 2.21	Analytical result and graph of error for scalar wedge problem	44
Figure 2.22	Error plot of scalar wedge problem	45
Figure 2.23	Error of FEM and GFEM solver	46
Figure 2.24	Error plot of FEM solver	47
Figure 2.25	Error plot of GFEM solver	48
Figure 3.1	Patch cross the material interface	52
Figure 3.2	Vector plots of homogeneous local approximation function \mathbf{v}_i	56
Figure 3.3	Convergence graphs for vector Neumann and Dirichlet BVPs by \mathbf{u}_{ap}^1	68
Figure 3.4	Convergence graphs for vector Neumann and Dirichlet BVPs by \mathbf{u}_{ap}^2	69
Figure 3.5	Convergence graphs for 3D homogeneous vector Neumann BVPs .	71
Figure 3.6	Convergence graphs for 3D homogeneous vector Neumann BVPs (Plane Wave)	71
Figure 3.7	Geometric description of the wedge	73
Figure 3.8	Analytical result for scattering from a wedge and error plot for y componnet	75
Figure 3.9	Analytical result for scattering from a wedge and error plot for y component	76
Figure 3.10	h, p convergence for wedge problem	77
Figure 3.11	Interface of two media	79
Figure 3.12	Vector plots of inhomogeneous local approximation function \mathbf{v}_i .	82
Figure 3.13	Convergence graphs for 2D inhomogeneous vector Neumann and Dirichlet BVPs	86
Figure 3.14	Convergence graphs for 3D inhomogeneous vector Dirichlet BVPs	87
Figure 3.15	Figure of patch on the curved structure	89
Figure 3.16	Local coordinate of patch on the curved structure	91
Figure 3.17	Vector plots of inhomogeneous local approximation function \mathbf{v}_i for curved interface	92
Figure 3.18	Geometric transform	94
Figure 3.19	Figure of patch on the curved structure	96
Figure 3.20	h-, p- convergence of the local approximation	96
Figure 3.21	Figure of rotated curved structure	98
Figure 3.22	Error with different curved surface	98
Figure 3.23	Geometric description of dielectric-coated PEC cylinder	99

Figure 3.24	Convergence graphs of GFEM solver with Dirichlet BC 99
Figure 3.25	Analytical and numerical result of ρ component of the field 100
Figure 3.26	Analytical and numerical result of ϕ component of the field 101
Figure 3.27	Figure of patch on the curved structure
Figure 3.28	Analytical and numerical result of large 2D inhomogeneous problem in the interface
Figure 3.29	Analytical and numerical result of large 2D inhomogeneous prob- lem out of the interface
Figure 3.30	Condition number of system with differen order of basis functions (p = 1,,4) $\dots \dots \dots$
Figure 3.31	Error of the solver with differen order of basis functions 108
Figure 3.32	Condition number of system with different order of basis functions (p = 1,,10)
Figure 4.1	APSW function in time and frequency domain 114
Figure 4.2	Stability of system with $N_{samp}=4$
Figure 4.3	Stability of system with $N_{samp} = 5$
Figure 4.4	Stability of system with $N_{samp}=4$
Figure 4.5	Stability of system with $N_{samp} = 5$
Figure 4.6	Analytical and numerical result with Dirichlet BC
Figure 4.7	Analytical and numerical result with Neumann BC $\dots \dots 128$
Figure 4.8	Analytical and numerical result with Impedance BC $\dots \dots 129$
Figure 4.9	h- p - convergence of the spatial basis function
Figure 4.10	Convergence of different temporal scheme in 2D homogeneous problem
Figure 4.11	Convergence of different temporal scheme in 2D inhomogeneous problem
Figure 4.12	Convergence of different temporal scheme in 3D homogeneous problem
Figure 4.13	Convergence of different temporal scheme in 3D inhomogeneous problem
Figure 4.14	Error with iterative solver
Figure 4.15	Number of iterative steps in each time step

LIST OF TABLES

Table 2.1	Error of eigenvalues in rectangular waveguide	3
Table 2.2	Error of eigenvalues in circular waveguide	4
Table 2.3	Error of eigenvalues in coaxial waveguide	14
Table 3.1	Error in eigenvalues computed using \mathbf{u}_{ap}^1	'2
Table 3.2	Error in eigenvalues computed using \mathbf{u}_{ap}^2	'2
Table 3.3	Error in eigenvalues computed using \mathbf{u}_{ap}^1	38
Table 4.1	The coefficients of characteristic equation	<u>!</u> 1

KEY TO SYMBOLS AND ABBREVIATIONS

FDTD: Finite-Difference Time-Domain

MoM: Method of Moments

FEM: Finite Element Method

FMM: Fast Multiple Method

PDE: Partial Differential Equation

GFEM: Generalized Finite Element Method

SPH: Smooth Particle Hydrodynamics

DEM: Diffuse Element Method

EFG: Element Free Galerkin

MLS: Moving Least Square

APSW: Approximate Prolate Spheroidal Wave

PML: Perfectly Matched Layer

SVD: Singular Value Decomposition

CFIE: Combined Field Integral Equation

EFIE: Electric Field Integral Equation

PEC: Perfect electrically conductor

EW: Echo Width

TE: Transverse Electric

TM: Transverse Magnetic

MOT: Matching On Time

CHAPTER 1

INTRODUCTION

Computational electromagnetics has grown over the last few decades, in terms of both development of the underlying tools and application to the design of practical systems. Typical methods of analysis are either based on integral equation or differential equation. As is well known, method of moment(MOM) and other integral equation-based method is expensive in terms of both memory and CPU-time. Augmenting this with fast multiple method(FMM) has considerably alleviated the cost. In differential equation based methods, the most popular are the finite difference time domain(FDTD) and finite element method(FEM).

The state of art of FEM tools [1] for electromagnetic analysis has grown by leaps and bounds over the past few decades. Classical methods require an underlying tesselation on which basis functions are defined. These basis functions are based on a span of polynomials, have finite support, and obey conditions at inter-element boundaries. For instance, Figure 1.1 shows the discretization of elliptical computation domain. Here, the edge of the meshes coincide with each other and they also coincide with the boundary of the computation domain as well.



Figure 1.1. Meshes for FEM

In classical FEM, the basis function is interpolatory. FEM solvers using this

basis have found widespread applications in solving problem in mechanical injury, stress strain, vibration analysis, heat transfer, etc [2, 3]. In the electromagnetics, early application of FEM did focus on directly using these space of functions [4, 5]. However, it was discovered that these basis functions do result in spurious modes as some conditions in the **E** and **H** are not satisfied. Furthermore, it is not possible to readily impose the boundary conditions.

Fortunately, vector basis function, e.g. edge element vector developed in 1980s [6, 7] is free of all the previous shortcomings. The zero order basis function is divergence free, as its tangential component is continuous across the edge of the mesh. In homogeneous domain, the normal component of the basis function is not continuous across the edge of the mesh, but the continuity of the normal component of numerical solution is enforced by the variation formula of the vector wave equation.

High order vector basis function are defined in two ways: hierarchical [8] and interpolatory [9]. Both have continuous tangential component cross the edge of the mesh, but they are not divergence free. Until now, high order basis functions have been continually refined [10, 11]. Likewise, basis functions that can be used in a h, p-convergence setting have been presented and applied to several engineering problems. Indeed, in a series of excellent papers, it has been shown that it is possible to have true h, p-convergence [12, 13].

But there are some limitation of classical FEM, that may prove to be a bottleneck. First, it requires a simplical structure. The edge of the mesh has to coincide with each other and the edge of the mesh has to coincide with the boundary of the computation domain as well. Having good quality meshes is also necessary for accuracy of the FEM solver. Both properties make mesh generation laborious and time consuming. When millions of unknowns are needed, time required for mesh generation might be over 90% of total CPU time. Developing h, p-convergence meshes or analyzing time varying phenomena that requires re-meshing at every time instant can be even more laborious. Another handicap of classical FEM is that the ansatz space used

to approximate the local behavior is a span of polynomials. It implies that solving problems in non-Lipschitzian domain is difficult. This is due to the fact that the field or its derivative are singular at the geometric singularity. This can not be simulated well by a span of polynomials even in dense meshes. If analytic local behavior is known, then it might be possible to use functions other than polynomials to approximate local behavior.

Those limitations result from the inter-element continuity requirements. The polynomial basis functions can enforce the requirements by its conforming property. There are still a variety of methods to realize it with non-polynomial basis. One is proposed by [14, 15]. Around the geometric singularity, there are one layer of meshes supporting the singular basis functions. Those basis functions are conformal to the neighboring regular elements. In this approach, the size of such meshes has to be almost one wavelength. Another category of totally different methods, hybrid methods, can construct the local function space in each mesh separately based on the physical analysis of the solution and enforce the inter element continuity requirements by additional constraints [16, 17]. In [16], lagrange multiplier is introduced to enforce it. This results in a larger linear system cause of the addition unknowns related to basis functions and the number of unknowns related to multipliers.

In this dissertation, I will introduce a new method that is free of the mentioned shortcoming. This method will be referred to as the generalized finite element method(GFEM)[18]. Comparing this method with regular FEM and hybrid methods, regular FEM enforces inter element continuity requirements by conformal finite elements but lacks the capability of physics of the problem. Hybrid methods have the freedom of choosing local approximation but additional constraints between elements are necessary. In one of hybrid methods, the function space for multiplier has to be defined carefully. GFEM shares both of the above advantages, e.g. any function space can be chosen to fit for the prior knowledge with conformal elements

enforcing the inter elements continuity requirements intrinsically which is free of above drawbacks.

GFEM belongs to the category of meshless methods [19]. The starting point of Meshless method is smooth particle hydrodynamics (SPH) method by Lucy in 1977 [20], The objective of meshless method is to eliminate the mesh generation procedure by constructing the approximation around the nodes. After that, the rate of publication about this topic was very modest until about the 1990s. In 1992, Nayroles [21] used the moving least square (MLS) approximations in a Galerkin method and called his method diffuse element method (DEM). Two years later, Belytschko [22] redefined and modified this method, and called it element free galerking(EFG). In 1996, there was a leap forward in the development of meshless methods with the introduction of GFEM by Babuska and Melenk [18, 23]. This method is based on partition of unity function and propose to a very powerful extension of the EFG approximation. In the same year, Duarte and Oden [24] extend the concept of partition of unity function to the MLS shape function and called it hp-cloud method. With this improvement, the EFG method based on MLS can be regarded as special instance of GFEM.

While meshless methods are well developed in some research area such as mechanical engineer, civil engineer, etc, they are largely used to solve scalar equation and usually solve the elliptic or parabolic PDEs. More specifically, it is used for specialized application such as crack propagation, etc [25]. The application of this technique to solving problems in electromagnetics has not been extensive. Principally (this is not a complete list), research has been conducted by [26–37]. The work in this area by Shanker and his colleagues revolved around developing meshless methods for solving the diffusion equation in both the frequency and time domain as applied to non-destructive evaluation [27–29]. The basis functions used in this analysis relied on the element free galerkin method (EFG) [19]. The method, particularly its scalar implementation, has been gaining a foothold in the research landscape

insofar as application to magnetic field analysis. Recently, they have explored the viability of suitably modifying the EFG method to enable the analysis of vector fields [31] and have developed meshless-PMLs to enable the analysis of open region problems [38] within the context of the EFG method. However, while the EFG method can be thought of as a subset of GFEM, it does not lend itself readily to hp-adaptivity, whereas this is inherent in other GFEM methods.

The above solvers are developed for the scalar differential equation. As was mentioned earlier, extending this to the vector differential equation that are encountered in EM results in spurious modes. These modes can be readily identified by studying the eigenfunction of same operator for defined geometry. Two kinds of modes can be distinguished. One is divergence free and another has high divergence value. The latter non physical modes plagued EM simulation and is known as spurious modes. The main reason of spurious problem is that the scalar FEM can not impose the divergence free criteria and satisfy the continuity requirements intrinsically. In classical FEM, several ways have been suggested for years to remove the spurious modes in FEM such as penalizing the divergence [39, 40] or using divergence free criteria to reduce 1/3 of dependent unknowns in three dimension [41–43]. The introduction of Whitney basis function, that is divergence free and tangentially continuous, provided the method to overcome this deficiency.

It follows from the above discussion that the vector GFEM solver should satisfy the following criteria:

The basis function developed should be able to approximate the field which is (i)divergence free (ii)satisfying all the continuity requirements on the material interface.

Except for the spurious problem, another problem is to impose essential boundary condition in GFEM solver when it's trivial in classical FEM. It also results in the difficulties to implement the boundary integral techniques with EFIE formula.

Another problem that plagues GFEM, as it does any higher order method is the

condition number of the resulting system. Indeed, this is more of a problem here as opposed to classical FEM as the space of basis functions is not interpolatory.

Tsukerman [35] tried to develop the vector basis function which can be used in a GFEM solver, but he did not demonstrate the convergence of the GFEM solver and the basis function can not handle inhomogeneous domain.

The objective of this dissertation is to develop vector GFEM method for EM analysis. The new method should be able to simulate the vector fields with high order accuracy. The principal goals of this research are as follows:

- Develop a scheme for implementing GFEM for the Helmholtz equation.
- When solving closed domain problem, an adaptation of Nitsche's method is developed for implementing the Dirichlet boundary condition. When solving open domain problem, the hybrid GFEM-BI method for domain truncation is developed.
- Develop vector basis function to approximate the divergence free field in homogeneous domain and prove bounds on their convergence.
- Develop basis functions for inhomogeneous domain that will enable the satisfaction of boundary conditions across flat and curved material interfaces. These conditions will be on the tangential components of the fields and their normal derivatives, and the normal component of the fields and their normal derivatives. We will mathematically prove the accuracy of the proposed method and demonstrate the convergence of the method for two dimension and three dimension.
- Develop a preconditioning scheme to solve the ill-conditioned system resulting from the high order system, and derive error bound and cost of this scheme.
- Develop time domain GFEM solver and prove and demonstrate the convergence of this method.

 Propose high order time stepping schemes based on approximate prolate spheroidal wave (APSW) and analyze the stability of the high order time stepping scheme. Demonstrate the convergence of the proposed scheme.

This dissertation is organized as followings: in the chapter 2, basic framework of GFEM method is introduced. The techniques for imposing different boundary conditions for both open domain and closed domain are elucidated. In chapter 3, vector GFEM method is developed for homogeneous domain and piecewise homogeneous domain with flat and curved material interface. The convergence of the solver will be proved and demonstrated in both two dimension and three dimension problems. A preconditioning scheme is also introduced in the same chapter with error bound and running cost provided. In chapter 4, high order time stepping schemes are proposed and demonstrated in two dimension and three dimension. Stability of high order time stepping schemes are analyzed. Finally, in chapter 5, a summary of the work and area for future research are collected.

CHAPTER 2

SCALAR GENERALIZED FINITE ELEMENT METHOD

2.1 Introduction

Intuitively, GFEM solver works as follows: the domain being considered is partitioned into a union of patches or a "partition of unity," and on these patches, the local approximation is constructed using a span of functions [44]. Thus, the representation of the function is achieved via two functions; one that is defined on the partitions of unity and the other on each of the patches. The basis functions describing the unknowns inherits the higher order nature of approximation from the local basis functions and the smoothness of the functions defined on the partition of unity. As with classical FEM, using a span of different local approximations in different regions is also possible. Thus, GFEM retains several features of classical FEM, provides additional flexibility in terms of functions that are used and obfuscates the need for a simplical partition of the domain.

The mathematical foundation of GFEM has been laid out in great detail [18, 23, 45], and it has been shown that h-, p- and hp-adaptivity is easily achieved. Likewise, the efficacy of using a space of harmonic functions as local approximants have been demonstrated [45]. Nevertheless, when some meshless solver has been developed for solving the diffusion equation in both the frequency and time domain as applied to non-destructive evaluation [27–29], it does not lend itself readily to hp-adaptivity.

Proper understanding of the sources of error and the means through which one may control them is important. We have found that in most of the implementation, reason that the convergence is not of the same order of the underlying scheme is largely due to the improper imposition of boundary conditions. Proper imposition of boundary conditions within a meshless scheme is challenging. Unlike classical FEM, the space of approximation functions are not *interpolatory*. This poses severe

challenges in imposing Dirichlet boundary conditions. More specifically, one cannot use the Lagrange multiplier technique as the approximation spaces have to obey the inf-sup condition, and it is not always possible to construct such spaces for meshless methods. This deficiency is directly linked to the difficulty in truncating the computational domain using boundary integrals. This is due to two facts; (i) to solve the hybrid problem, one typically defines an auxiliary set of basis functions and unknowns to represent the tangential components of the fields [1]. It implies from the above discussion [46] that these basis functions, together with those used in the interior, should satisfy the inf-sup (Babuska-Brezzi) condition, and (ii) there are practical situations wherein one uses a first kind Fredholm integral equation as the boundary is not closed. In these cases, the BI enforces a Dirichlet type condition. Thus, the principal content of this chapter is four fold:

- 1. A scheme for implementing GFEM for the Helmholtz equation is presented.
- 2. An adaptation of Nitsche's method for implementing the Dirichlet boundary condition is developed.
- Hybrid GFEM-BI technique for domain truncation for both open and closed domains is presented.
- 4. Methodology wherein local boundary conditions can be integrated with GFEM-more specifically, the perfectly matched layer (PML), is presented. The development of this technique is a by-product of the need to have an additional modality of validating the results obtained by the GFEM-BI scheme.

The rationale for embarking upon this specific problem is as follows: (a) This approach presented in this chapter (basis functions/means to impose boundary conditions, etc) can readily used for solution of quasi-static electromagnetic phenomena and scalar wave equations; (b) It permits us to work out several mathematical and numerical hurdles—the principal being the application of Dirichlet boundary condi-

tion and the accurate evaluation of integrals; (c) it is equally important to understand the manner in which boundary integral based techniques can be hybridized with this scheme. The advantage of hybridizing GFEM with BI is readily apparent; it imposes an exact boundary condition for open domain problems, and the computational cost can be amortized using recent advances in the integral equation technology, namely the fast multipole method or a host of FFT-based schemes.

This chapter proceeds along the following lines; in the next section, we formulate the problem in detail. Here, we introduce the concepts of GFEM, discretization of the domain, basis functions, methods for integration, and methods for implementing various boundary condition. The last includes different types of boundary integral techniques and a local absorbing boundary condition. Next, we demonstrate the accuracy and convergence of the GFEM and GFEM-BI via a series of analytical comparisons. We shall also demonstrate the accuracy of this scheme by comparing the results obtained against those obtained by truncating the domain using a PML as an absorbing boundary condition. Finally, we will demonstrate the advantages of GFEM solver by scattering analysis with geometric singularity.

2.2 Basic framework of GFEM solver

2.2.1 Formula of basis function

Consider a multiply connected domain Ω whose interior boundaries are denoted by $\partial\Omega := \Gamma = \bigcup_i \Gamma_i$. It is assumed that this domain is embedded in a domain Ω_e and its exterior boundary Γ_e is defined as $\Gamma_e := \Omega_e \cap \bar{\Omega}$. Interior to the domain Ω , the function $u(\mathbf{r})$ satisfies

$$\left(\nabla \cdot [\alpha(\mathbf{r})\nabla] + \omega^2 \gamma(\mathbf{r})\right) u(\mathbf{r}) = f(\mathbf{r})$$

$$\mathcal{B}_i \{u(\mathbf{r})\} = g_i(\mathbf{r}) \text{ for } \mathbf{r} \in \Gamma_i$$

$$\mathcal{B}_e \{u(\mathbf{r})\} = g_e(\mathbf{r}) \text{ for } \mathbf{r} \in \Gamma_e$$
(2.1)

In the above equations, it is assumed that $\mathbf{r} \in \mathbb{R}^d$, \mathcal{B}_e and \mathcal{B}_i are differential operators, and $g_i(\mathbf{r})$ is the function that is imposed on Γ_i . Here, d=2,3, and $\alpha(\mathbf{r})$ and $\gamma(\mathbf{r})$ are material parameters. The function of interest, $u(\mathbf{r})$, is used to denote the \hat{z} component of either the electric or magnetic field. The rationale of defining Γ_e explicitly is to impose appropriate boundary conditions that enable the analysis of scattering problems. The parameters $\alpha(\mathbf{r})$ and $\beta(\mathbf{r})$ can stand for either the permittivity or permeability, depending on the variable that $u(\mathbf{r})$ represents. Solution to this problem using the standard finite element method requires an underlying tesselation on which basis functions are defined. These basis functions are based on a span of polynomials, have finite support, and obey conditions at inter-element boundaries. For instance, Whitney elements that are typically used in computational electromagnetics satisfy either tangential or normal continuity across inter-element boundaries. Higher order basis functions based on these elements have also been presented and have been continually refined [10, 11]. Likewise, basis functions that can be used in a h, p-convergence setting have been presented and applied to several engineering problems. Indeed, in a series of excellent papers, it has been shown that it is possible to have true hp-adaptivity [12, 13]. On the other hand, meshless methods attach a patch or volumina to each point whose union forms an open covering of the domain. The local shape functions are constructed within each domain. Several different flavors of these methods exists [23]. In this dissertation we will base our development on the generalized finite element method (GFEM) [23].

Our presentation of the fundamentals of basis functions is a repetition of those in [45, 47]. GFEM is based on a set of N nodes located at \mathbf{r}_i in the vicinity of the domain Ω such that $\left\{\mathbf{r}_i \in \mathbb{R}^d : \mathbf{r}_i \in \Omega, i=1,\cdots,N\right\}$. Associated with each of these nodes is a patch or volumina denoted by Ω_i of size h_i such that $\Omega \subset C_\Omega := \bigcup_i \Omega_i$ and $\Omega_i = \left\{\mathbf{r} \in \mathbb{R}^d : ||\mathbf{r} - \mathbf{r}_i|| \le h_i\right\} \subset \mathbb{R}^d$. Specifically, a patch Ω_i is defined as $\Omega_i = \bigotimes_{k=1}^d \Omega_i^{(k)}$, $\Omega_i^{(k)} = \{r^{(k)} \in \mathbb{R}, |r_i^{(k)} - r^{(k)}| \le h_i^{(k)}\}$. Figure 2.1 describes such a construction. Typically, there are no restrictions on the shape of the domain.

To a large extent, these are chosen depending on the underlying basis functions.

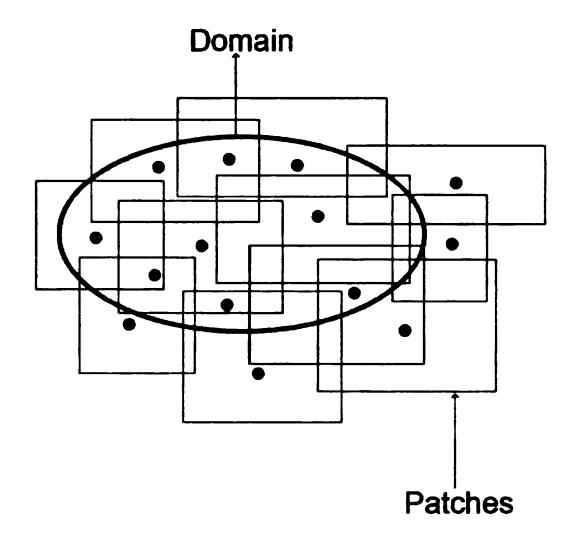


Figure 2.1. Construction of the computational domain.

Associated with each patch are basis functions that will be used for Galerkin testing and source. The basis function is a product of two functions, $\psi_i(\mathbf{r})$ and $v_i(\mathbf{r})$: functions $\psi_i(\mathbf{r})$ form a partition of unity subordinate to the cover Ω_i , and a space of functions $v_i(\mathbf{r}) \in span\{v_i^m(\mathbf{r})\}$ that are local to the domain Ω_i .

The global approximation of the variable is then a space of functions denoted by $V_i(\mathbf{r}) = \psi_i(\mathbf{r})v_i(\mathbf{r})$. The basic theory of the GFEM method using this space of functions was originally developed by Babuska and Melenk [45] and is summarized below. Note that the definitions listed below are key to some of the proposed tasks.

Definition 2.1:

Let $\Omega \in \mathbb{R}^d$ be an open set, and let Ω_i be an open cover of Ω satisfying a pointwise overlap condition

$$\exists M \in N \ \forall \mathbf{r} \in \Omega \ card \{i | \mathbf{r} \in \Omega_i\} \le M \tag{2.2}$$

Definition 2.2:

Let $\{\psi_i\}$ be a Lipchitz partition of unity subordinate to the cover $\{\Omega_i\}$ satisfying the following conditions: (i) $\operatorname{supp}(\psi_i) \subset \Omega_i$ for all i; (ii) $\sum_i \psi_i \equiv 1$ on Ω ; (iii) $||\psi_i||_{L^\infty(\mathbb{R}^d)} \leq C_\infty$; and (iv) $||\nabla \psi_i||_{L^\infty(\mathbb{R}^d)} \leq C_\nabla / \operatorname{diam}(w_i)$. Here C_∞ and C_∇ are two constants. Then $\{\psi_i\}$ is called an (M, C_∞, C_∇) partition of unity subordinate to $\{\Omega_i\}$. The partition of unity is said to be of degree k if $\psi_i \in \mathcal{C}^k(\mathbb{R}^d)$. The covering sets Ω_i are called patches.

Assume that the space of functions $V(\mathbf{r}) = span \{\psi_i v_i\}$ is given. Let the function $u_{ap} := \sum_i \psi_i v_i \in V \subset H^1(\Omega)$ be an approximation to $u(\mathbf{r})$. The upper bounds on the error in the function and its gradient have been derived in [45].

The choice of the functions $\psi_i(\mathbf{r})$ and $v_i(\mathbf{r})$ can vary from patch to patch, and is usually dictated by the geometry of the problem. More specifically, the functions $v_i(\mathbf{r})$ can theoretically be modified to include logarithmic singularities. However, the first step of implementing this method is the construction of the patches Ω_i of size h_i that form the open cover for the domain. In general, we allow h_i^j , for $j=1,\cdots,d$ to be different in each dimension. In this dissertation, we have restricted ourselves to rectangular domains. As the patches Ω_i are to be used in a Galerkin scheme, it is necessary for $\bigcup_i \Omega_i \supset \Omega$. In other words, for any $\mathbf{r} \in \Omega$ there exists at least one patch Ω_i that contains \mathbf{r} . The following steps is utilized to realize it [47]:

- N nodes are chosen randomly in the computation domain and \tilde{h}_i is chosen initially as the size of the i^{th} patch. With circle-shaped patch, the \tilde{h}_i can be the radius of the circle; with rectangle-shaped patch, \tilde{h}_i can be half of the side length.
- Much more denser testing points are uniformly distributed in the computation domain. The testing points has to be at least 10^d times denser than the nodes.
 Each testing point should be covered by at least one patch. If any testing point

is not covered by one patch, then look for the node which is closest to it. Then increasing the size of the patch \tilde{h}_j to make j^{th} patch covers that testing point.

• When each testing point can be covered by at least one patch, true patch size h_i can be derived as $h_i = \alpha \tilde{h}_i$ where $\alpha > 1$. Number α is used to assure the enough overlapping between the patches so that the smoothness of the partition of unity function ψ_i can be maintained.

This will ensure that for $\mathbf{r} \in \Omega$ there exists at least one patch such that $\mathbf{r} \in \Omega_i$. Next, the partition of unity functions ψ_i are defined in each Ω_i . By definition, $\sum_{i} \psi_{i}(\mathbf{r}) = 1 \ \forall \ \mathbf{r} \in \Omega_{i}$. To construct these functions, we use a localized version of Shepard's method [48] that relies on defining a function $W_i(\mathbf{r})$ with respect to each characteristic point $\mathbf{r}_i \in \Omega_i$ such that $\mathcal{W}_i(\mathbf{r}) = 0 \ \forall \mathbf{r} \in \partial \Omega_i$. In other words, these functions are different from zero only for $\mathbf{r} \in \Omega_i$. Several choices for these functions exist; the most common are B-splines of different orders, Gaussian, regularized Lagrangians, etc. The choice of the functions \mathcal{W}_i depends on shape of the patch. In this dissertation, we restrict ourselves to rectangular domains, and therefore, to B-splines of different orders. Then in d-dimensions we construct a function $W_i(\mathbf{r})$ using a tensor product of 1-D functions; i.e., $\mathcal{W}_i(\mathbf{r}) = \prod_{l=1}^d \mathcal{W}\left((\mathbf{r} - \mathbf{r}_i^l)/(h_i^l)\right)$. Next, the functions $\psi_i(\mathbf{r})$ are defined by $\psi_i(\mathbf{r}) = (W_i(\mathbf{r}))/(\sum_{\Omega_k \in C_i} W_k(\mathbf{r}))$, wherein $C_i := \left\{ \Omega_i \in C_{\Omega} | \Omega_i \cap \Omega_j \neq 0 \right\}$. Here defined partition of unity function $\psi_i(\mathbf{r})$ satisfy the criteria $\sum_i \psi_i(\mathbf{r}) = 1 \forall \mathbf{r}$. Figure 2.2 shows a one dimension example of the partition of unity function. As is evident from the figure, patches overlap with each other, and there is one partition of unity function in each patch. The summation of all partition of unity functions in one patch equals one at any point. We can also create the partition of unity function based on MLS functions [49], when high order basis functions are used, the error of Shepard and MLS functions are almost the same though MLS functions are much more complicated in terms of formulation [49].

The partition of unity functions are consistent to first order and higher order

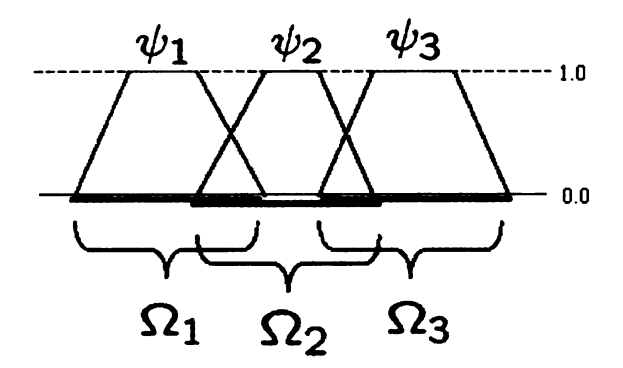


Figure 2.2. One dimensional partition of unity function.

approximations are obtained by defining higher order local functions, $v_i(\mathbf{r})$. As mentioned in [45], local approximating functions can be chosen such that they better capture the local behavior of the current. However, in this chapter, we have restricted our choices to Legendre polynomials of order P. Thus, in any domain Ω_i the functions $v_i(\mathbf{r}) = span\left\{\prod_{l=1}^d f_{p(l)}\left((r^{(l)}-r_i^{(l)})/(h_i^{(l)})\right)\right\}$ where $p(l)=0,\cdots,P$.

Figure 2.3 shows a one dimension example of the construction of the scalar basis function. The three local approximation functions are chosen as 0^{th} , 1^{st} and 2^{nd} order Legendre polynomials. Basis functions, $\psi_i(\mathbf{r})v_i^m(\mathbf{r})$, decay to zero at the edge of the patch, which assure the continuity of the numerical solution. Since there is no restriction on the choice of the basis functions, they can be chosen such that they best approximate the local physics. For instance, around the smooth geometry plane wave can be chosen as local approximation, around the geometric singularity eigenfunction of the singular structure can be used, etc.

It is well known that bilinear form of the differential equation (4.1) on $H^1(\Omega)$ is

$$\mathcal{A}(u, w) = (f, w) \ \forall \ (u \text{ and } w) \in H^{1}(\Omega)$$
 (2.3a)

$$\mathcal{A}(u,w) = -(\alpha \nabla u, \nabla w) + \omega^{2}(\gamma u, w)$$
 (2.3b)

where (\cdot,\cdot) denotes the standard inner product in $L^2(\Omega)$. It is apparent that we

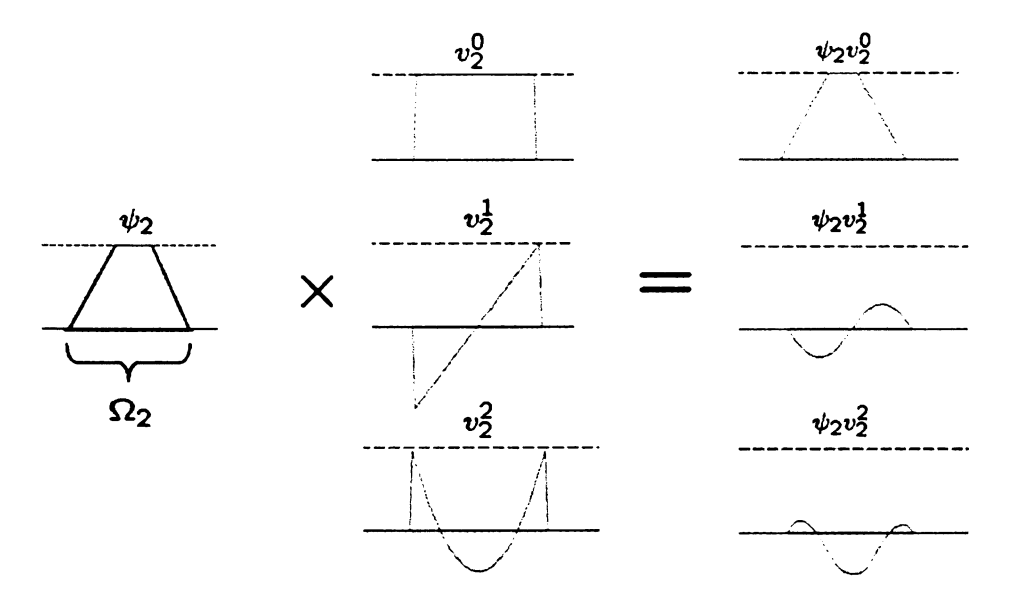


Figure 2.3. Construction of one dimensional Basis function.

have not yet incorporated the boundary conditions; the means by which various boundary conditions are incorporated into the variational form will be dealt with exhaustively in Section 2.3. Using the definitions of basis functions elaborated upon thusfar, $u(\mathbf{r})$ can be now approximated as $u(\mathbf{r}) = \sum_{i}^{N} I_{i}V_{i}$, where N is the total degrees of freedom. Using Galerkin method, the discrete version of this bilinear form can be written as

$$\mathcal{A}\left(u_{i,n}, w_{j,m}\right) = \mathcal{A}\left(\psi_{i} v_{i}^{n}, \psi_{j} v_{j}^{m}\right)$$
(2.4a)

$$(f, w_{j,m}) = \left(f, \psi_j v_j^m\right) \tag{2.4b}$$

Above equations (2.3) indicate that the $\nabla u_{i,n}$ need to be evaluated. Here we use

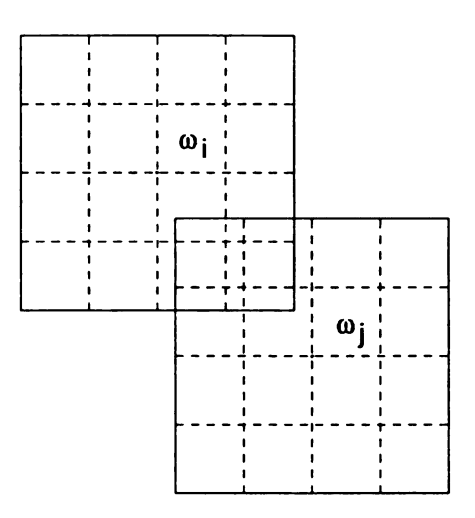


Figure 2.4. Subdivision of the domain of integration based on piecewise weight function W_i .

the following formula to evaluate it:

$$\nabla u_{i}^{n} = \nabla (\psi_{i} v_{i}^{n})$$

$$= \nabla (\frac{\mathcal{W}_{i}}{\sum_{\Omega_{k} \in C_{i}} \mathcal{W}_{k}} v_{i}^{n})$$

$$= \frac{\nabla \mathcal{W}_{i} \sum_{\Omega_{k} \in C_{i}} \mathcal{W}_{k} v_{i}^{n} - \mathcal{W}_{i} \sum_{\Omega_{k} \in C_{i}} \nabla \mathcal{W}_{k} v_{i}^{n}}{(\sum_{\Omega_{k} \in C_{i}} \mathcal{W}_{k})^{2}}$$

$$+ \frac{\mathcal{W}_{i}}{\sum_{\Omega_{k} \in C_{i}} \mathcal{W}_{k}} \nabla v_{i}^{n}$$
(2.5)

Note, that the equations (2.4) indicate that the interaction between any two domains form block matrices. However, what is crucial in the process is the evaluation of the inner products; this will be dealt with next.

2.2.2 Evaluation of inner products

The basis functions $V_i(\mathbf{r})$ that were introduced earlier are piecewise rational functions. This is immediately apparent when one examines the construction of $\psi_i(\mathbf{r})$; a different number of functions $W_i(\mathbf{r})$ may contribute to $\psi_i(\mathbf{r})$ at different location. This implies that the quadrature rules must be such that they respect these dis-

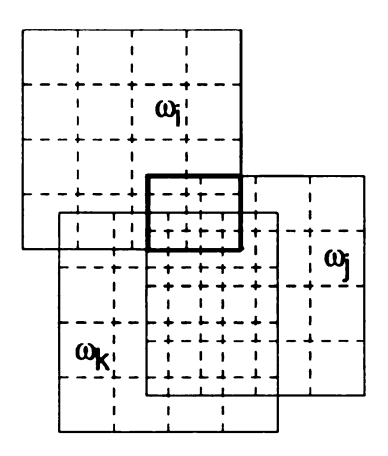


Figure 2.5. Subdivision of D_{ij}^n based on the number of patches at different location.

continuities. To overcome these deficiencies, we have followed a method similar to the one proposed by Schweitzer [50]. Here the domain of integration is subdivided into smaller domains where the integrand can be represented as a product two rational functions. Note that the integrands comprise of products of both $\psi_i(\mathbf{r})v_i^m(\mathbf{r})$ and their derivatives. To illustrate the decomposition of the domain, consider two patches Ω_i and Ω_j that overlap; the domain of overlap is denoted by $C_{ij} := \Omega_i \cap \Omega_j$. Further assume that in each domain, the weight functions $W_i(\mathbf{r})$ and $W_j(\mathbf{r})$ are polynomials of degree l. Then in Ω_i , the function $\mathcal{W}_i(\mathbf{r})$ is piecewise rational in $(l+1)^d$ -domains. As the function $\psi_i(\mathbf{r})$ is a combination of both $\mathcal{W}_i(\mathbf{r})$ and $\mathcal{W}_j(\mathbf{r})$ for $\mathbf{r} \in \Omega_i$, we can partition the intersection C_{ij} into $C_{ij} = \bigcup_n D_{ij}^n$ disjoint subcells as in Figure 2.4, and $\psi_i(\mathbf{r})$ is piecewise rational in each subcell. The process becomes more involved when more than two patches overlap. Such a scenario is illustrated in Figure 2.5. Assume $E_{ijk}:=\Omega_j\cap\Omega_j\cap\Omega_k$ denotes the domain of intersection of these three domains. It follows that $\bigcup_m F^m_{ijk} \subseteq \bigcup_n D^n_{ij}$ denotes the union of domains wherein the function $\psi_i(\mathbf{r})$ is piecewise continuous. Recursive identification of domains where the function $\psi_i(\mathbf{r})$ is piecewise rational ensures the appropriate

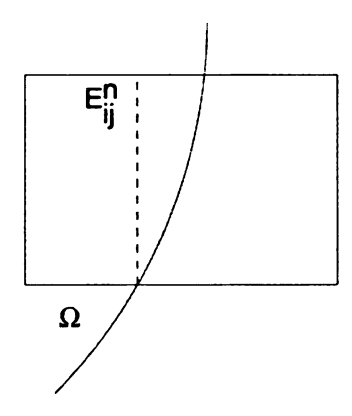


Figure 2.6. Integration in the sub-patch E_{ij}^n that overlaps with boundary of computation domain Γ .

construction of quadrature rules.

The above procedure works well for intersection between two domains $C_{ij} := \Omega_i \cap \Omega_j \subset \Omega$. However, if Γ dissects C_{ij} , then it can no longer be considered a union of rectangular domains; see Figure 2.6. As before, assume that $C_{ij} = \bigcup_n D_{ij}^n$, and in each D_{ij}^n the functions ψ_i and ψ_j are rational functions. The cells D_{ij}^n are be partitioned into two sets; those that are fully contained within Ω and those that intersect Γ . For the former, we shall use the standard quadrature rules; the latter can be be evaluated through adaptive quadrature. In this chapter, we have restricted ourselves to boundaries that are circular. The geometric choice permits the division into rectangular domains and curvilinear triangles as shown in Figure 2.6. As before, we use standard quadrature rules in the rectangles, and coordinate transformation and higher order integration in the triangles [1]. Thus, the prescribed procedure enables higher order evaluation of all the inner products in the variational form.

Here is the brief explanation of the higher order integration in the curvilinear triangle. As shown in Figure 2.7, a curvilinear triangle in xy-domain can be mapped

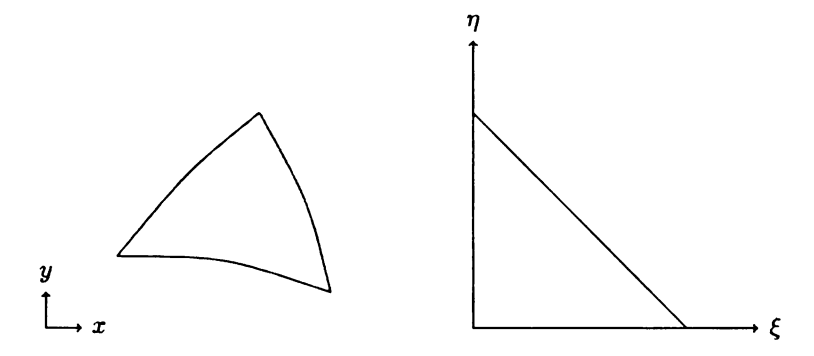


Figure 2.7. Geometry transform

to a regular triangle in $\xi\eta$ -plane. Transform functions

$$x = x(\xi, \eta)$$

$$y = y(\xi, \eta)$$
(2.6)

are known. So to the related two points (x_p, y_p) and (ξ_p, η_p) in xy-plane and $\xi\eta$ plane. Given the definition of Jacobian matrix of the transform

$$[\mathbf{J}] = \begin{bmatrix} \frac{\partial x}{\partial \xi} & \frac{\partial y}{\partial \xi} \\ \frac{\partial x}{\partial \eta} & \frac{\partial y}{\partial \eta} \end{bmatrix}$$
(2.7)

and $|\mathbf{J}|$ is Jacobian, then

$$u(x_p, y_p) = u(\xi_p, \eta_p)$$

$$\mathbf{u}(x_p, y_p) = [\mathbf{J}]^{-1} \cdot \mathbf{u}(\xi_p, \eta_p)$$

$$dxdy = |\mathbf{J}| d\xi d\eta$$
(2.8)

2.3 Imposing boundary conditions

It is evident from the above exposition, that (i) the basis functions V_i are NOT interpolatory; (ii) $\Omega \subset \bigcup_n \text{supp } \{V_n\}$. These two facts make imposition of boundary

conditions more difficult than those for classical h, p convergence FEM methods. In this section, we will discuss the imposition of both the Nuemann and Dirichlet boundary conditions, as well as the truncation of the domain using boundary integrals.

2.3.1 Neumann Boundary Condition:

First, consider the differential equation in (2.1) with $\mathcal{B}_i\{u(\mathbf{r})\} = \alpha u_n = \alpha \hat{n} \cdot \nabla u(\mathbf{r}) = g_n(\mathbf{r}) \ \forall \mathbf{r} \in \Gamma$. Here, \hat{n} denotes the outward pointing normal from the domain Ω . This boundary condition implies that the bilinear form is to be modified as

$$\mathcal{A}(u,w) = (f,w) - \int_{\Gamma} d\Gamma g_n(\mathbf{r}) w(\mathbf{r})$$
 (2.9)

From the above, it is apparent that it is sufficient for the trial and basis functions to be in $H^1(\Omega)$. There are no additional constraints, and the basis do not have to satisfy the boundary conditions. Hence, incorporation of Neumann boundary condition is no different than that in classical FEM.

2.3.2 Dirichlet Boundary Condition:

Next, assume that $\mathcal{B}_i\{u(\mathbf{r})\}=u(\mathbf{r})=g(\mathbf{r})\ \forall \mathbf{r}\in\Gamma$, i.e., Dirichlet boundary condition explicitly imposes the values of $u(\mathbf{r})$ on the boundary of the domain. Alternatively, the problem may be cast as follows: "find $u(\mathbf{r})\in H^1(\Omega)$ such that $u(\mathbf{r})=g(\mathbf{r})\ \forall\ \mathbf{r}\in\Gamma$ " and the bilinear form for $w\in H^1(\Omega)$

$$\mathcal{A}(u,w) = -\int_{\Gamma} d\Gamma \alpha(\mathbf{r}) w(\mathbf{r}) \hat{n} \cdot \nabla u(\mathbf{r}) + (f,w)$$
 (2.10)

This statement is not very different from that posed for standard FEM albeit with a couple of differences: in classical FEM (1) $w \in H_0^1(\Omega)$ which implies that the integral over the boundary vanishes; (ii) the basis functions are interpolatory. Hence, imposing the boundary conditions is tantamount to modifying the linear system. In GFEM, both the trial and test function do not satisfy either of these properties.

Thus, imposing Dirichlet boundary conditions is not as straightforward. This has been a topic of considerable discussion [51].

Several Methods attempted are introduced here. (i) to hybridize meshless methods with classical FEM; (ii) use a penalty function method; (iii) use a Lagrange multiplier technique, and (iv) use Nitsche's method. Of the four methods, we have chosen to use Nitsche's method to impose the boundary condition. While we shall discuss this method detail, we shall also dwell briefly on other three as it will shed light on the constraints on imposing a global boundary condition.

When hybridizing meshless methods with classical FEM, FEM meshes is generated around the boundary. When far away from the boundary, EFG basis functions are constructed. On the interface of two basis functions, FEM basis are as usual and in meshless methods, shape functions take care of the consistency of the approximation.

The formulation using penalty function is stated as: $u(\mathbf{r}) \in H^1(\Omega)$, find the solution to

$$\mathcal{A}_h(u, w) = \mathcal{F}_h \ \forall w \in V_N \tag{2.11a}$$

$$\mathcal{A}_{h}(u, w) = -\left(\alpha \nabla u, \nabla w\right) + \beta \int_{\Gamma} d\Gamma \ uw \tag{2.11b}$$

$$\mathcal{F}_h = (f, w) + \beta \int_{\Gamma} d\Gamma \ gw \tag{2.11c}$$

This method has two advantages. The dimension of the final system is not increased, the system is symmetric and positive definite. But the Dirichlet is imposed weakly and results in ill-conditioned matrix system.

Solving the problem using Lagrange multipliers involves finding a solution $(u, \lambda) \in H^{(\Omega)} \times H^{-1/2}(\Gamma)$. The formulation can than be stated as follows: given

 $u(\mathbf{r}) \in H^1(\Omega)$ and $\lambda \in H^{-1/2}(\Gamma)$ find the solution to

$$\mathcal{A}_h(u,\lambda;w,\mu) = \mathcal{F}_h \ \forall \ (w \ \text{and} \ \mu) \in H^1(\Omega) \times H^{-1/2}(\Gamma)$$
 (2.12a)

$$\mathcal{A}_{h} = -\left(\alpha \nabla u, \nabla w\right) + \omega^{2} \left(\gamma u, w\right) + \left\langle \lambda, w \right\rangle + \left\langle u, \mu \right\rangle \tag{2.12b}$$

$$\mathcal{F}_h = (f, w) + \langle g, \mu \rangle \tag{2.12c}$$

Solution to the discrete version of this equation in the GFEM setting is not trivial. It is well-known that for this problem to converge, it is necessary for both the interior and multiplier spaces to fulfill the Babuska-Brezzi condition. The Babuska-Brezzi condition can be expressed as:

$$Inf_{\lambda \in H^{-1/2}(\Gamma)} Sup_{u \in H^1(\Omega)} \frac{(\nabla \cdot u, \lambda)}{||u||_{H^1(\Omega)} ||\lambda||_{H^{-1/2}(\Gamma)}} \le \gamma > 0$$
 (2.13)

while it's easy to find λ when using classical FEM, but it is difficult to design such multiplier space that satisfies this condition [52–54], especially for the space of basis functions being considered here. Moreover, Lagrange multiplier based techniques lead to indefinite systems. An alternative to this could be a stabilized-Lagrange multiplier technique [55]. However, in what follows, we use the Nitsche's technique for imposing the Dirichlet boundary condition. This method is related to the stabilized Largrange multiplier technique with two advantages: (i) it is relatively straightforward to implement in a numerical scheme, and (ii) one does not need to define an additional space of functions in $H^{-1/2}(\Gamma)$. The method proceeds as follows: find

an approximate solution such that $u(\mathbf{r}) \in V_N \subset H^1(\Omega)$ such that

$$\mathcal{A}_h(u, w) = \mathcal{F}_h \ \forall w \in V_N \tag{2.14a}$$

$$\mathcal{A}_{h}(u,w) = -\left(\alpha \nabla u, \nabla w\right) + \omega^{2} \left(\gamma u, w\right) + \int_{\Gamma} d\Gamma \,\alpha u \hat{n} \cdot \nabla w \tag{2.14b}$$

$$+ \int_{\Gamma} dx \; \alpha w \hat{n} \cdot \nabla u - \beta \int_{\Gamma} dx \; uw \qquad (2.14c)$$

$$\mathcal{F}_{h} = (f, w) + \int_{\Gamma} dx \alpha g \hat{n} \cdot \nabla w - \beta \int_{\Gamma} d\Gamma g w \qquad (2.14d)$$

where β is chosen such that it guarantees coercivity. Rigorous estimates exist for β [50]. As is also apparent from the above equations, the resulting system is symmetric.

2.3.3 Global Radiation Boundary Condition:

The above exposition has a significant impact on the development of a global boundary condition. In standard FEM-BI expositions [1], one defines equivalent currents on Γ_e , and uses the radiation boundary integral to impose either the electric field or the magnetic field or a combination of both. The equivalent current are of both the electric and magnetic types. As $u(\mathbf{r})$ represents one field (either the electric or magnetic field), either the magnetic or electric currents can be easily obtained. One typically prescribes basis functions for all $\mathbf{r} \in \Gamma_e$ to represent currents. However, from our preceding discussion it is apparent that basis functions prescribed on Γ_e have to belong to $H^{-1/2}(\Gamma_e)$, and these functions together with those used in the interior have to satisfy the Babuska-Brezzi condition. While such a space can be easily developed in the case of standard tesselation, it is perhaps not possible for GFEM. Therefore, prescribing additional unknowns on the boundary is ruled out. The method that we use for hybridizing will depend on whether $\Gamma_e = \partial \Omega$ or $\Gamma_e \subset \partial \Omega$. In the former case, the domain of integration encloses a volume, and in the latter, it is open. When the domain is closed, it is sufficient to prescribe conditions such that the solution is unique; i.e., one does not excite the interior resonance modes. While this is a solved problem, it is implementing this condition within the context of GFEM that causes problems. If $\Gamma_e \subset \partial \Omega$, then imposing conditions is considerably more challenging, as imposing the BI is similar to prescribing a Dirichlet boundary condition. This is challenging on two counts; (i) the basis functions V_i are NOT interpolatory; (ii) $\Omega \subset \bigcup_n \sup \{V_n\}$. Therefore, techniques that were used earlier to overcome this problem [1] need to be modified to impose the boundary condition.

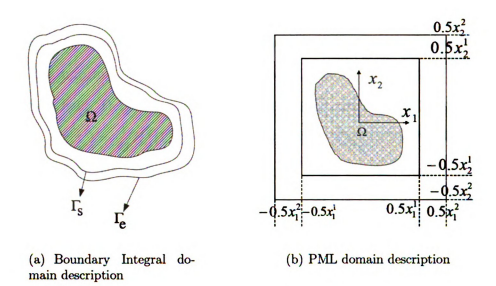


Figure 2.8. (a) Definition of geometry for imposing the boundary integral; (b) Definition of the geometry for application of the PML.

Our formulation proceeds as follows: Assume that just inside the boundary, one can define another surface Γ_s that completely encloses all the inhomogeneities in Ω ; see Figure 2.8(a). For the purposes of discussion, assume that $u(\mathbf{r})$ refers to the electric field. Then $\forall \mathbf{r} \in \Gamma_e$,

$$u(\mathbf{r}) = u^{inc}(\mathbf{r}) + \mathcal{L}\left\{u(\mathbf{r})\right\}$$
 (2.15a)

$$\partial_n u(\mathbf{r}) = \partial_n u^{inc}(\mathbf{r}) + \mathcal{K} \{u(\mathbf{r})\}$$
 (2.15b)

$$\mathcal{L}\left\{u(\mathbf{r})\right\} := -\int_{\Gamma_{S}} d\Gamma_{S} \left(\partial_{n'} u(\mathbf{r'}) g(\mathbf{r}, \mathbf{r'}) - u(\mathbf{r'}) \partial_{n'} g(\mathbf{r}, \mathbf{r'})\right)$$
(2.15c)

$$\mathcal{K}\left\{u(\mathbf{r})\right\} := \int_{\Gamma_{s}} d\Gamma_{s} \left(\partial_{n'} u(\mathbf{r'}) \partial_{n} g(\mathbf{r}, \mathbf{r'}) - u(\mathbf{r'}) g_{t}(\mathbf{r}, \mathbf{r'})\right)$$
(2.15d)

where $\partial_{n'}$ and ∂_n are used to denote the normal derivatives with respect to the primed and unprimed coordinates, respectively, $\hat{t} = -\hat{n} \times \hat{z}$, and $u^{inc}(\mathbf{r})$ denotes the incident field. Denoting $\mathbf{r} = \mathbf{r} - \mathbf{r}'$ where $\mathbf{r} \in \mathbb{R}^2$, the Green's functions may be written as $g(\mathbf{r}, \mathbf{r}') = \frac{1}{4j}H_0^2(k|\mathbf{r}|)$ and $g_t(\mathbf{r}, \mathbf{r}') = k^2(\hat{t} \cdot \hat{t}')g(\mathbf{r}, \mathbf{r}') + \hat{t}' \cdot (\nabla \nabla g(\mathbf{r}, \mathbf{r}')) \cdot \hat{t}$ where \hat{t} and \hat{t}' are the tangent vectors at \mathbf{r} and \mathbf{r}' , respectively. These equations are essentially derived from surface equivalence theorems (or Huygen's principle). Note, the surfaces Γ_e and Γ_s can be arbitrarily close to each other; however, if they are very close to each other, the integral operators in (2.15) may be singular/hyper-singular, and one should evaluate these with care. Techniques for doing so are similar to those prescribed in [56]. Next, to incorporate the global boundary condition within the differential equation solver, one needs to specify the differential operator $\mathcal{B}_e\{u(\mathbf{r})\}$ in (4.1). The simplest is to specify that $\mathcal{B}_e\{u(\mathbf{r})\} = u(\mathbf{r}) = u^{inc}(\mathbf{r}) + \mathcal{L}\{u(\mathbf{r})\} \ \forall \mathbf{r} \in \Gamma_e$. This is, of course, a Dirichlet type boundary condition, and has to be incorporated

using Nitsche's method; more specifically by implementing the following

$$\mathcal{A}_{h}(u,w) = \mathcal{F}_{h} \ \forall w \in V_{N}$$

$$\mathcal{A}_{h}(u,w) = -\left(\alpha \nabla u, \nabla w\right) + \omega^{2} \left(\gamma u, w\right) + \int_{\Gamma} d\Gamma \ \alpha u \hat{n} \cdot \nabla w + \int_{\Gamma} d\Gamma \ \alpha w \hat{n} \cdot \nabla u$$

$$(2.16b)$$

$$-\beta \int_{\Gamma} d\Gamma \ uw - \int_{\Gamma} d\Gamma \alpha \mathcal{L} \left\{ u(\mathbf{r}) \right\} \hat{n} \cdot \nabla w + \beta \int_{\Gamma} d\Gamma \omega \mathcal{L} \left\{ u(\mathbf{r}) \right\}$$

$$\mathcal{F}_{h} = (f, w) + \int_{\Gamma} d\Gamma \alpha u^{inc} \hat{n} \cdot \nabla w - \beta \int_{\Gamma} d\Gamma \ u^{inc} w \qquad (2.16c)$$

Alternatively, one can specify $\mathcal{B}_e\{u(\mathbf{r})\} = \partial_n u(\mathbf{r}) = \partial_n u^{inc}(\mathbf{r}) + \mathcal{K}\{u(\mathbf{r})\} \ \forall \mathbf{r} \in \Gamma_e$. As before, this is the Neumann type boundary condition, and can be incorporated by appropriately modifying the variational formulation. However, it is well known that both global boundary conditions do not yield unique solutions at all frequencies. These frequencies correspond to the null spaces of the appropriate operators [1]. Among the several methods prescribed [1] to overcome this deficiency, one is to combine the two operators; i.e., use a combined field formulation. Thus, the method proceeds as follows: find an approximate solution $u(\mathbf{r}) \in H^1(\Omega)$ such that

$$\mathcal{A}_h(u, w) = \mathcal{F}_h \ \forall w \in H^1(\Omega)$$
 (2.17a)

$$\mathcal{A}_{h}(u, w) = -\left(\alpha \nabla u, \nabla w\right) + \omega^{2} \left(\gamma u, w\right) - jk \int_{\Gamma_{e}} d\Gamma w(\mathbf{r}) u(\mathbf{r}) + \tag{2.17b}$$

$$\int_{\Gamma_{e}} d\Gamma \ w(\mathbf{r}) \left[jk\mathcal{L} \left\{ u(\mathbf{r}) \right\} + \mathcal{K} \left\{ u(\mathbf{r}) \right\} \right]$$
 (2.17c)

$$\mathcal{F}_{h} = (f, w) - \int_{\Gamma_{e}} d\Gamma w(\mathbf{r}) \left[jku^{inc}(\mathbf{r}) + \partial_{n}u^{inc}(\mathbf{r}) \right]$$
 (2.17d)

In the above exposition, we have essentially focused on imposing the boundary condition at Γ_e . As in (2.1), another condition might need to be imposed in the interior boundaries. However, as is apparent, the bilinear form for imposing these conditions may be derived trivially using material presented thusfar. Evaluation of the integrals over the boundary may be carried out using several different methods.

In our implementation, we proceed as follows: The domain of integration (either Γ_s or Γ_e can be partitioned into a union of subdomains over with the basis function is piecewise smooth. Then over each such subdomain, we use a Gauss-Legendre quadrature. While this is not truly optimal and one may construct better quadrature rules, we did obtain convergent results.

2.3.4 Local Radiation Boundary Condition:

Our interest in implementing the local boundary condition is purely to develop another measure of validating the results obtained using global boundary condition. As we will show, the results obtained using GFEM-BI converge exponentially to analytical solutions. However, as these solutions are available only for canonical problems, it is of interest to know that the fields obtained using the afore-developed scheme and those obtained using a local boundary condition agree with each other. There is a wealth of local boundary conditions that are available [1, 57]. Here we implement a perfectly matched layer (PML) within GFEM. The literature on PML is extensive, and our goal is to present a rudimentary development that can be used as a validation modality. The approach that we use to implement this relies on the stretched coordinate system first introduced in [58]. Using this technique results in a slight change in $\alpha(\mathbf{r})$ in that it becomes a tensor of rank 2, i.e., $\bar{\alpha}(\mathbf{r}) = \alpha_0 \alpha_{ij}(\mathbf{r})$. The quantity $\bar{\gamma}(\mathbf{r})$ and the non-zero elements of $\bar{\alpha}(\mathbf{r})$ are

$$\alpha_{11}(\mathbf{r}) = \alpha_0 \frac{s_1(\mathbf{r})}{s_2(\mathbf{r})} \qquad \alpha_{22}(\mathbf{r}) = \alpha_0 \frac{s_2(\mathbf{r})}{s_1(\mathbf{r})}$$

$$\tilde{\gamma}(\mathbf{r}) = \gamma_0 s_1(\mathbf{r}) s_2(\mathbf{r})$$
(2.18)

where $\mathbf{r} = (x_1, x_2)$, α_0 and γ_0 are appropriate constants when all stretching parameters are one, and

$$s_1(\mathbf{r}) = 1 - j \frac{\sigma_{11}(x_1)}{\omega \varepsilon_0} \quad s_2(\mathbf{r}) = 1 - j \frac{\sigma_{22}(x_2)}{\omega \varepsilon_0}$$
 (2.19)

In these equations, s_1 and s_2 are stretching coordinates, and $\sigma_{ij}(\mathbf{r})$ denotes the conductivity tensor of the domain. As is apparent, this tensor is chosen to be diagonal. The domain of application of the PML is denoted using $\Omega_{PML} = \Omega_0 - \Omega_i$, where the rectangular domains Ω_0 and Ω_i are defined as $\Omega_0 = x_1^2 \times x_2^2$ and $\Omega_i = x_1^1 \times x_2^1$; see Figure 2.8(b). The conductivity profiles are chosen to be zero inside the Γ_i and vary quadratically in the direction of the outward normal to the boundary Γ_i . σ_{11} is nonzero in domain $(-0.5x_1^2, -0.5x_1^1) \times (-0.5x_2^2, 0.5x_2^2)$ and $(0.5x_1^1, 0.5x_1^2) \times (-0.5x_2^2, 0.5x_2^2)$, σ_{22} is nonzero in domain $(-0.5x_1^2, 0.5x_1^2) \times (-0.5x_2^2, 0.5x_2^2)$ and $(0.5x_1^2, 0.5x_2^2)$. Finally, the computational domain is truncated by imposing the condition

$$\hat{n} \cdot \nabla u^s + jk\cos(\theta_a)u^s = 0 \tag{2.20}$$

on Γ_0 . Here, θ_a denotes the angle of perfect absorption and is chosen to be $\theta_a = \frac{\pi}{3}$ in our simulation. Note that in this formulation, the unknown is scattered field u^s . With these changes, the bilinear form may now be written as

$$\mathcal{A}_h(u^s, w) = \mathcal{F}_h \ \forall w \in V_N \tag{2.21a}$$

$$\mathcal{A}_{h}(u^{s}, w) = -\left(\bar{\alpha} \cdot \nabla u^{s}, \nabla w\right) + \omega^{2}\left(\tilde{\gamma}u^{s}, w\right) - jkcos(\theta_{a}) \int_{\Gamma} d\Gamma \ u^{s}w \qquad (2.21b)$$

$$\mathcal{F}_{h} = (f, w) - \left(\alpha \nabla^{2} u^{inc}, w\right) - \omega^{2} \left(\gamma u^{inc}, w\right)$$
 (2.21c)

2.4 Numerical experiments

In what follows, we shall present a series of numerical experiments that will serve to demonstrate the accuracy and convergence of the method presented herein. In all examples presented below, we have chosen d=2 merely for demonstration purposes, and extension to d=3 will be exploited in the next chapter. First, we shall demonstrate h, p convergence for problems wherein either the Dirichlet or Neumann boundary conditions are specified. Next, we shall demonstrate similar convergence for our hybrid GFEM-BI scheme and also demonstrate that our scheme is free from

corruption due to interior resonance modes. In these examples, global boundary conditions are used to truncate the computational domain, and Dirichlet boundary conditions are imposed in the interior of the domain. After that, we present a set of results that analyze electrically large problems, and compare these against either analytical results or against GFEM augmented with local boundary truncation schemes. Finally, we will analyze the scattering from PEC wedge with mode-based GFEM solver. While meshless methods offer a host of advantages, one significant hurdle/unsolved problem is the conditioning of the resultant linear system as the order of the basis function increases. This is an issue when we are trying to demonstrate h, p convergence. In these cases, we resort to an singular value decomposition(SVD)-based solver. However, in the analysis of electrically large objects, wherein we are satisfied with an error in the L_2 -norm = 1e-4, we use a non-stationary iterative solver like TFQMR [59] with block preconditioners.

In the next two examples, we demonstrate h,p convergence of this method when imposing either the Neumann or the Dirichlet boundary condition. The domain of analysis of both problems are the same and defined as follows: the domain of interest $\Omega = (0,1)^2$, and the boundary $\Gamma = \bigcup_i^4 \Gamma_i$ where $\{\Gamma_1 : \mathbf{r} \in 0 \times (0,1)\}$, $\{\Gamma_2 : \mathbf{r} \in (0,1) \times 1\}$, $\{\Gamma_3 : \mathbf{r} \in 1 \times (0,1)\}$, and $\{\Gamma_4 : \mathbf{r} \in (0,1) \times 0\}$.

In the first example, the Neumann boundary conditions are imposed on all four walls. More specifically, \mathcal{B}_i $\{u(\mathbf{r})\} = \partial_n u(\mathbf{r})|_{\forall \mathbf{r} \in \Gamma_i} = g_i(\mathbf{r})$. Denoting $\mathbf{r} = (x_1, x_2)$, $g_i(\mathbf{r}) = 0, -2.97\cos(4x_1), \ 3.0272\sin(3x_2), 3\cos(4x_1), \ \text{for } i = 1, \cdots.4$. The above boundary conditions permit analytical solution of the (2.1). In this experiment, uniformly distributed nodes and rectangular patches are used. The size of each patch is 1.5 times the distance between the nodes. The weight functions $\mathcal{W}_i(\mathbf{r})$ is a product rooftops, and the approximation is a tensor product of Legendre polynomials. Two sets of results are shown. First, we demonstrate the error between analytical and numerical solutions in Figure 2.9 for $h = 0.11\lambda$ and p = 4. We also demonstrate h, p convergence in Figure 2.10. As is evident from the graphs, the results are excellent.

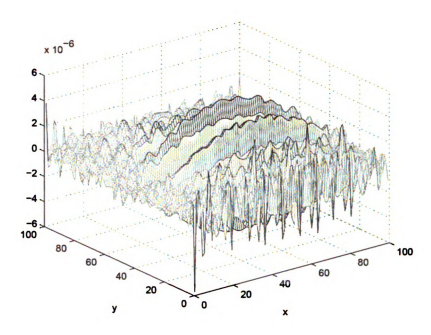


Figure 2.9. Error in the L_2 norm of the numerical and analytical solutions of the PDE with the Neumann boundary condition.

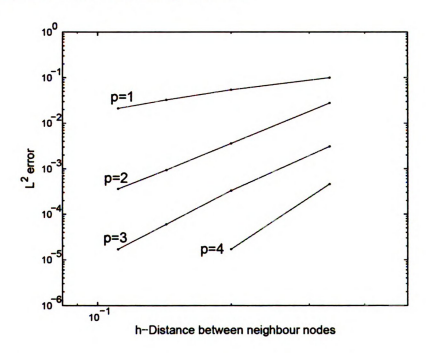


Figure 2.10. h,p convergence of the numerical scheme applied to the solution of a PDE with Neumann boundary conditions.

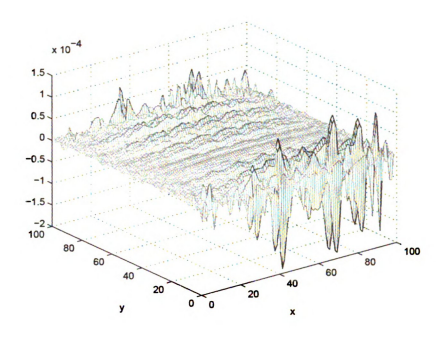


Figure 2.11. Error in the L_2 norm of the numerical and analytical solutions of the PDE with the Dirichlet boundary condition.

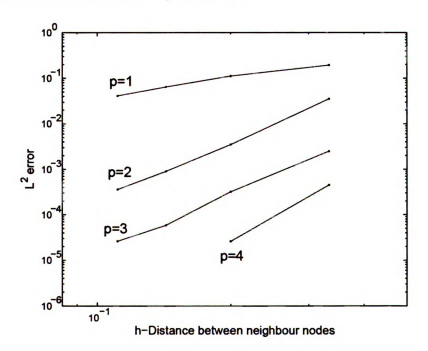


Figure 2.12. h,p convergence of the numerical scheme applied to the solution of a PDE with Dirichlet boundary condition.

TE	Principal Mode		p=1	p=2	p=3	p=4
		h = 1/4	0.0244	5.49e-4	2.61e-6	9.67e-9
		h = 1/6	0.0151	1.07e-4	2.42e-7	3.84e-10
	First 8	h = 1/4	0.087	8.44e-3	1.62e-4	3.02e-6
	modes	h = 1/6	0.0533	1.67e-3	1.58e-5	1.05e-7
ТМ	Principal	h = 1/4	0.0567	3.78e-4	3.10e-6	7.79e-9
	Mode	h = 1/6	0.0285	8.14e-5	2.59e-7	3.20e-10
	First 8	h = 1/4	0.1557	0.0142	3.20e-3	1.99e-5
	Modes	h = 1/6	0.1122	5.27e-3	1.85e-4	2.28e-6

Table 2.1. Error of eigenvalues in rectangular waveguide

Next, the Dirichlet boundary condition is imposed on all four walls. More specifically, $\mathcal{B}_i \{u(\mathbf{r})\} = u(\mathbf{r})|_{\forall \mathbf{r} \in \Gamma_i} = g_i(\mathbf{r})$. Denoting $\mathbf{r} = (x_1, x_2)$, $g_i(\mathbf{r}) = \sin(3x_2)$, 0.1411 $\cos(4x_1)$, $-0.6536\sin(3x_2)$, 0, for $i = 1, \dots, 4$. All the parameters used in the computation are the same as those used for imposing the Neumann boundary condition. Again, the Figure 2.11 plots the relative value of the error in the entire computational domain when using $h = 0.11\lambda$ and p = 4. Also, the errors for different values for h and p are shown in Figure 2.12. It is evident that Nitsche's method for imposing the boundary conditions shows excellent convergence.

Next, we compute the eigenmodes in a rectangular waveguide. The dimensions of the waveguide are chosen to be $1m \times 1m$. The convergence data (error in L^2 norm) for both TE^z and TM^z modes are presented in the Table 2.1. As is evident from this data, the results obtained converge rapidly with increasing order and refinement.

Next, we compute the eigenmodes in a circular waveguide. The radius of circle is chosen to be 1m. Table 2.2 show the error of eigenvalues for both TE^z and TM^z modes. Again, the results obtained converge rapidly with increasing h and p.

Then, we compute the eigenmodes in a coaxial waveguide. The radius of inner and outer circles are chosen to be 0.5m and 1m. The error of eigenvalues are presented in the Table 2.3. The results is excellent.

Next, we examine the accuracy of imposing the boundary integral to truncate

TE	Principal Mode		p = 1	p = 2	p=3	p=4
		h = 1/4	0.0191	4.43e-4	2.19e-6	6.09e-7
		h = 1/6	0.0127	9.14e-5	5.72e-7	4.20e-7
	First 5	h = 1/4	0.1137	0.0157	1.20e-3	3.26e-5
	modes	h = 1/6	0.0817	4.52e-3	1.12e-4	2.11e-6
ТМ	Principal	h = 1/4	0.0677	9.47e-4	9.97e-6	5.84e-7
	Mode	h = 1/6	0.0351	2.14e-4	4.56e-7	4.42e-7
	First 5	h = 1/4	0.175	0.291	0.040	2.12e-4
	Modes	h = 1/6	0.131	0.090	4.21e-4	7.41e-6

Table 2.2. Error of eigenvalues in circular waveguide

TE	Principal Mode		p = 1	p=2	p=3	p=4
		h = 1/4	0.0311	2.91e-3	3.09e-4	3.69e-5
		h = 1/6	0.0205	5.61e-4	2.98e-5	1.26e-6
	First 5	h = 1/4	0.1062	0.0307	5.35e-3	8.31e-4
	modes	h = 1/6	0.693	0.0101	7.10e-4	5.51e-5
ТМ	Principal	h = 1/4	0.2137	0.0103	2.41e-3	2.23e-5
	Mode	h = 1/6	0.1369	2.96e-3	2.73e-4	6.36e-7
	First 5	h = 1/4	0.2169	0.0402	8.64e-3	1.91e-3
	Modes	h = 1/6	0.1529	0.0165	2.23e-3	1.31e-4

Table 2.3. Error of eigenvalues in coaxial waveguide

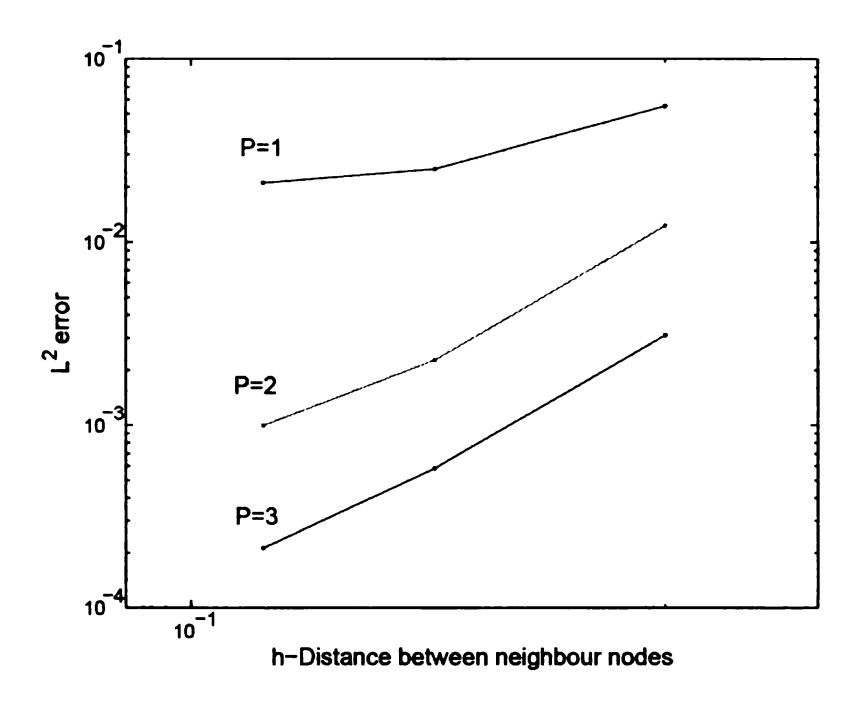


Figure 2.13. h, p convergence of GFEM-BI (CFIE)

the domain. To do so we analyze scattering from a perfect electrically conducting (PEC) cylinder with radius 0.1λ and the truncation boundary is placed 0.1λ away from the surface. Given the configuration of the problem, we need to apply the BI (CFIE) (2.17a) and Dirichlet boundary condition on the truncation boundary Γ_e and the inner boundary, respectively. We compare these results against that obtained analytically to obtain the h,p convergence graphs in Figure 2.13. As is evident, the scheme presented in this chapter demonstrates the anticipated convergence characteristics. The next, we analyze scattering from a PEC cylinder over a range of frequencies. The outer boundary is truncated using the EFIE specified in (2.16a), and the inner boundary is truncated using a Dirichlet boundary condition. We know that truncating the outer boundary with the EFIE would lead to unique values for all values of ka except those that correspond to interior resonance modes of a cylinder with a PEC wall at the outer boundary. Thus, to satisfy ourselves that

this is indeed the case, and to show that the variational form that imposes the EFIE formulation presented in this chapter is valid (note: EFIE is imposed using Nitsche's method), we analyze scattering from a cylinder over a range ka varying from 2.0 to 8.0 in steps of 0.05. Additionally, values of ka that are within three digits of the resonance frequencies corresponding to TM^2 modes of the cylinder whose radius corresponds to that of Γ_e are chosen. In total, we ran this simulation for a total of 128 frequency points. In all cases, $h = 0.1\lambda$ and p = 3. Figure 2.14 compares the error in the field values within the computational domain to analytical data. As is expected, Figure 2.14 shows the results obtained are accurate except at resonance frequencies. So, the next challenge is to ensure that our results are free of corruption by spurious modes. Again, we analyze scattering from a PEC cylinder over a range of frequencies with combined boundary integral formula. It is apparent from Figure 2.15 that the error is fairly constant over the entire band of frequencies. It should be noted that in all the cases mentioned thus far, we are quoting the error in the field values at a sufficient dense set of samples inside the computational domain. These error are NOT in the echo width data, as they tend to be significantly smaller.

Next, we demonstrate the applicability of this technique to various scattering problems. In all three examples described, the incident plane wave propagates along the \hat{x} direction and is polarized along \hat{z} . First, scattering from a cylinder of radius 2.7λ is analyzed. The source boundary Γ_s and fictitious boundary Γ_e are at 2.85λ and 3.0λ , respectively, and $h=0.11\lambda$ and p=3. The analytical and numerical data of electric field on fictitious boundary and echo width (EW) are compared in Figure 2.16. As is evident from these graphs, the results are excellent. Next, scattering from dielectric-coated PEC cylinder is analyzed. The radius of the PEC cylinder is 2.82λ , and the thickness of the dielectric coating is 0.06λ . The relative permittivity of dielectric is 2.0. The source boundary Γ_s and fictitious boundary Γ_e are at 2.94λ and 3.0λ , respectively, where λ is the free space wavelength and $h=0.12\lambda$ and p=3. The analytical and numerical data of the electric field on fictitious boundary

and echo width (EW) are compared in Figure 2.17. As is evident from these graphs, the results are excellent. Finally, we analyze scattering from a coated cylinder that is considerably larger. The radius of cylinder PEC and dielectric coating are 3.76λ and 3.84λ , respectively. The source boundary Γ_8 and fictitious boundary Γ_e are at 3.92λ and 4.0λ , respectively. As before, λ is the free-space wavelength, $\varepsilon_r=2$, $h=0.15\lambda$ and p=3. Our discretization in this case is considerably coarser, however, as is evident from Figure 2.18 (a,b), both the fields on the fictitious surface and the echo-width agree very well with the analytical data.

In the next example, we compare the results obtained using GFEM-BI with those obtained by analyzing the same object using GFEM-PML. As is well known, the principal advantage of the boundary integral is that realized by a reduced computational domain. This, of course, implies that the cost of application of the BI can be reduced to something that scales almost linearly with the number of unknowns on the boundary. This is indeed possible by augmenting the BI with acceleration techniques, notably by the fast multipole technique [60]. The object that we choose for simulation is a L-shaped dielectric scatterer. The length and width of each arm is 1λ and 0.3λ , respectively, and the arms are oriented along the \hat{x} and \hat{y} directions. The truncation boundary Γ_e for the BI is conformal to the scatterer and is at a distance of 0.25λ away from the scatterer. When employing the PML, the scatterer is embedded in an rectangular domain of size $\Omega_i = 5.4 \times 5.4 \lambda^2$, and the thickness of the PML is 0.95λ . In both simulations, $h = 0.08\lambda$ and p = 3, and the relative dielectric constant $\varepsilon_r = 2$. The incident field is \hat{z} polarized and propagates along $\hat{k} = -1/\sqrt{2} \, (\hat{x} + \hat{y})$. Figure 2.19(a,b) show the fields obtained by both methods. As is evident, they are identical to each other. Indeed, the relative error in the field values at a set of points in the domain is 2.3e-3, indicating that both techniques compare very well with each other.

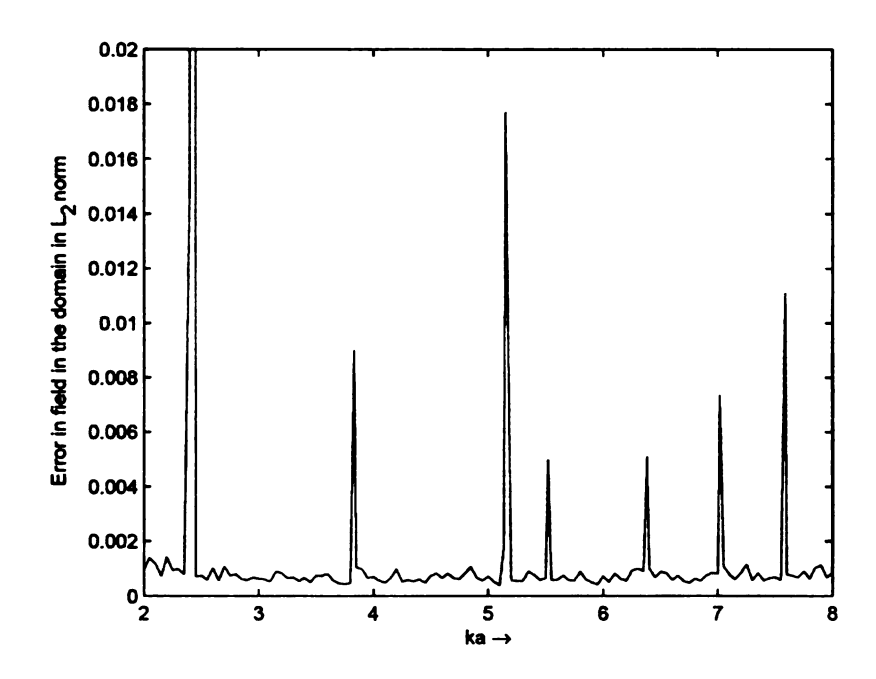


Figure 2.14. Error in E-field over a range of ka with GFEM-BI (EFIE)

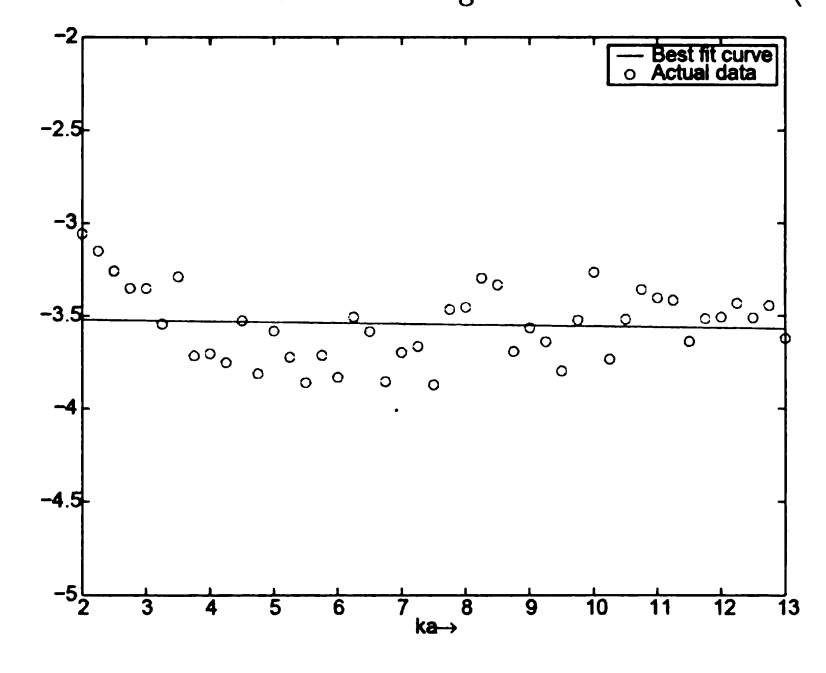
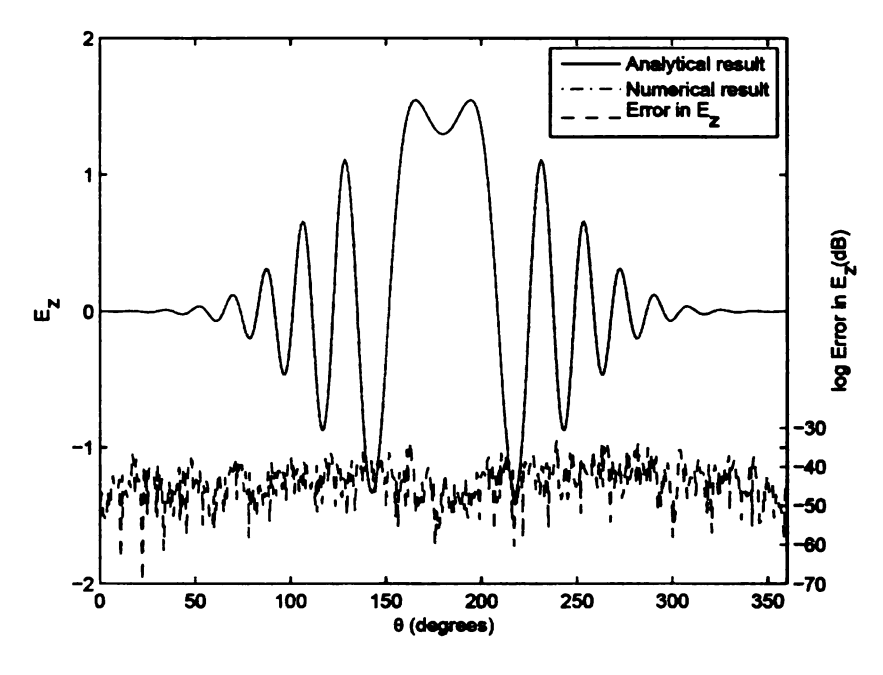


Figure 2.15. Error in E-field over a range of ka with GFEM-BI (CFIE)



(a) E_z on fictitious boundary Γ_e

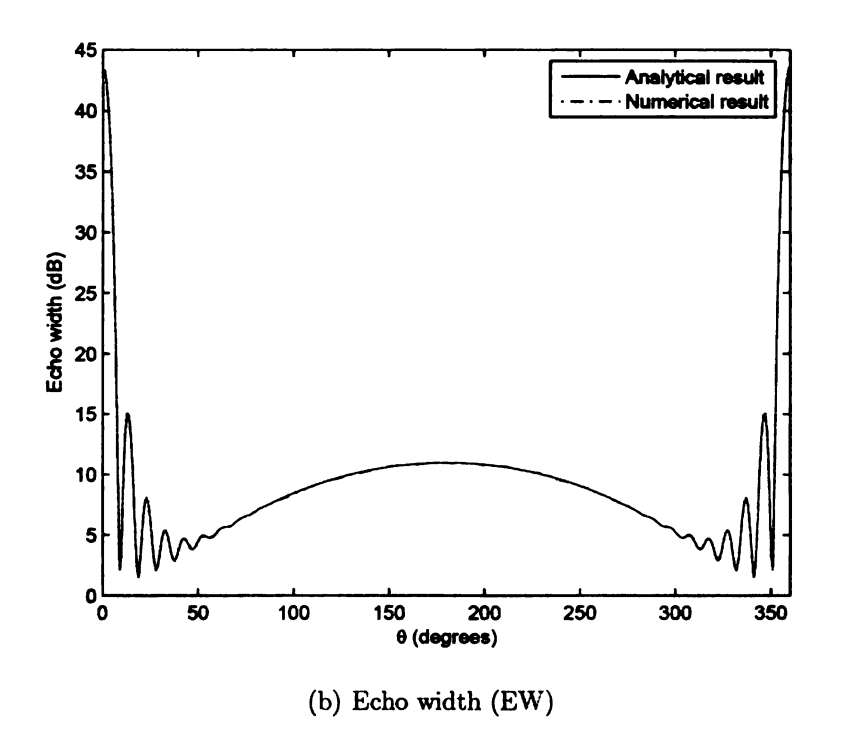
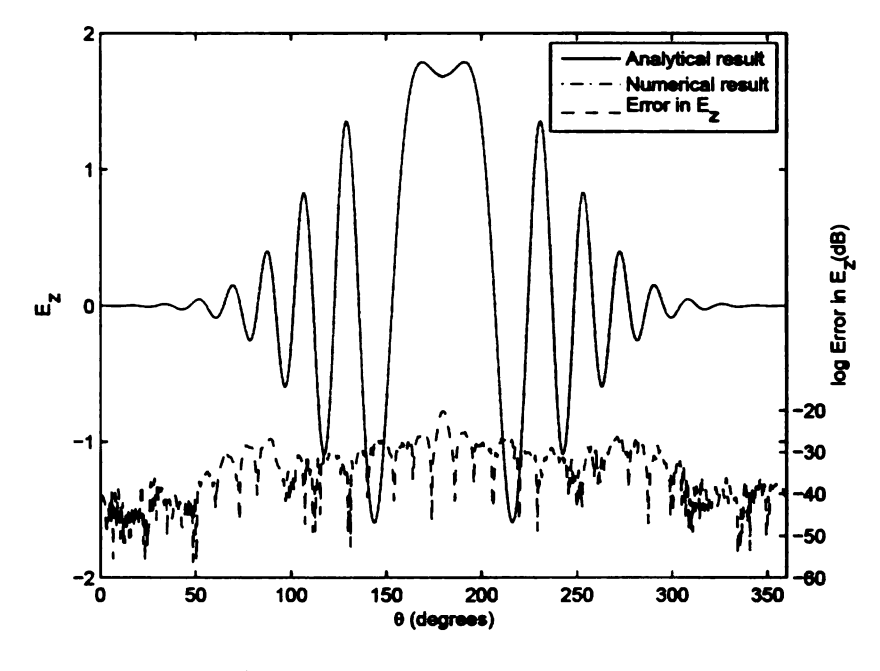
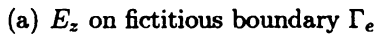


Figure 2.16. Comparison between numerical and analytical data obtained for scattering from a perfectly conducting cylinder of radius 2.7 λ : (a) the electric field at Γ_e ; (b) Echo-width of the cylinder.





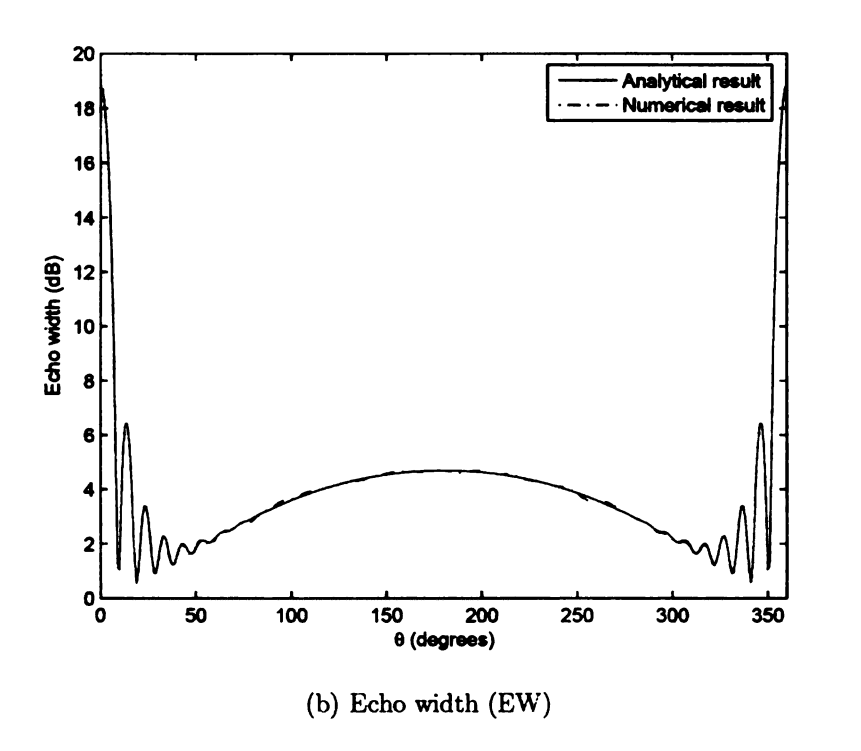
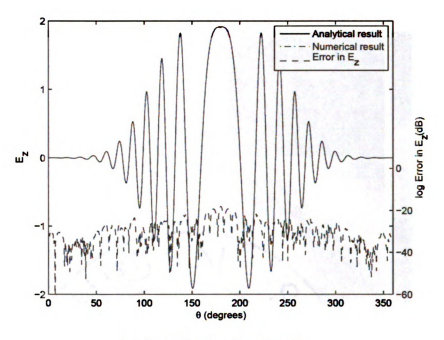


Figure 2.17. Comparison between numerical and analytical data obtained for scattering from the coated perfectly conducting cylinder if radius 2.88 λ : (a) the electric field at Γ_e ; (b) Echo-width of the cylinder.





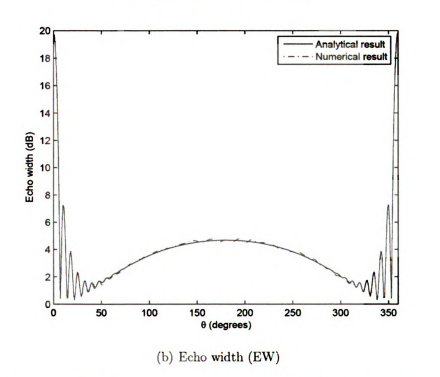


Figure 2.18. Comparison between numerical and analytical data obtained for scattering from a coated perfectly conducting cylinder of radius 3.84 λ : (a) the electric field at Γ_e ; (b) Echo-width.

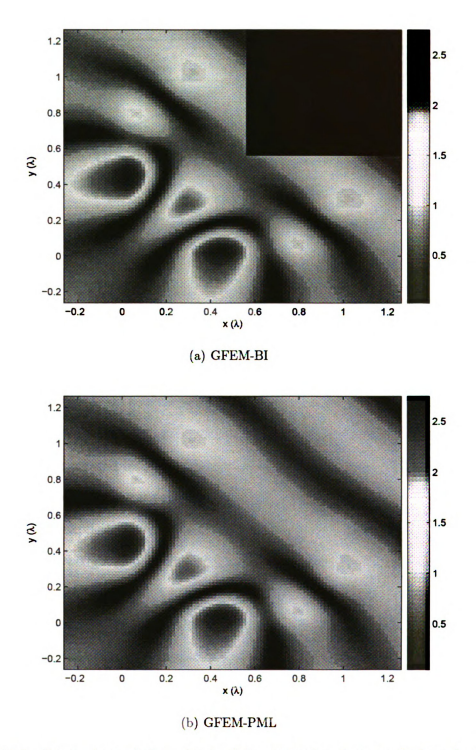


Figure 2.19. Comparison of data obtained for scattering from an L-shaped object using GFEM-BI and GFEM-PML.

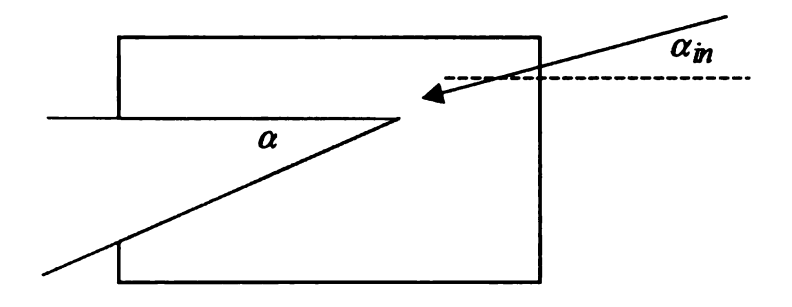
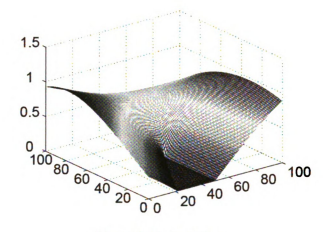
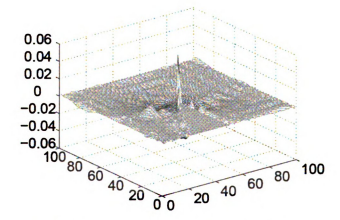


Figure 2.20. Geometric description of the wedge

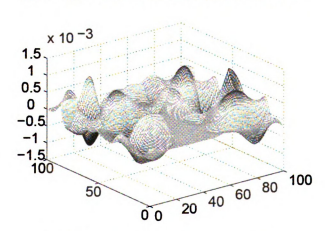
Until now, the basis functions used in all the examples have been based on tensor products of polynomials. The power of GFEM, however, is the ability to include analytical behavior, if known, into the approximation space. To test this idea, To test this idea, we analyze scattering from a wedge. The analytical response of this structure is well known [61]. Indeed, [15] developed singular basis functions that can be incorporated into the function space of the classical FEM methods (see references therein for other approaches to constructing singular functions). In what follows, we will explicitly incorporate the known functional behavior. Consider a two dimensional wedge with angle $\frac{\pi}{6}$ that is located in a rectangular computational domain $\Omega = (-1.0, 1.0) \times (-1.0, 1.0)$. The tip of the wedge coincides with the origin of the computational domain and one side lies in the y=0 plane. A field that is polarized along the \hat{z} and propagating along $\hat{k}=-0.9659\hat{x}-0.2588\hat{y}$ is incident upon the wedge, and the wavenumber $k_0=3$; this geometric configuration is shown in Figure 3.7.



(a) Analytical solution



(b) Graph of error based on polynomial function



(c) Graph of error based on eigen function

Figure 2.21. Analytical result and graph of error for scalar wedge problem

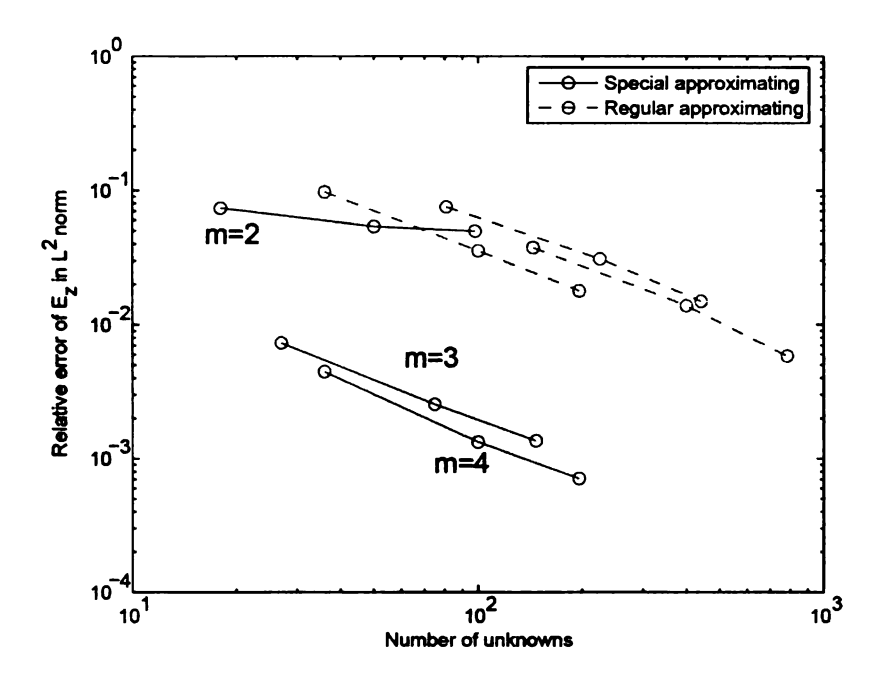


Figure 2.22. Error plot of scalar wedge problem

It can be easily shown that the fields are given by

$$E_{z} = \frac{4\pi E_{0}}{2\pi - \alpha} \sum_{v} j^{v} J_{v}(k\rho) sin[v(\alpha_{in} + \pi - \alpha)] sin[v(\phi + \pi - \alpha)]$$

$$v = \frac{m\pi}{2\pi - \alpha} \qquad m = 1, 2, \cdots$$

$$(2.22)$$

Modes $J_v(k\rho)sin[v(\phi+\pi-\alpha)]$ are used as scalar local approximating function. The infinite extent of the wedge is simulated by imposing analytical solutions for the infinite wedge as Dirichlet boundary conditions. The relative error is computed using L^2 norm of error in the electric field at 100×100 sample points that are uniformly distributed along \hat{x} and \hat{y} direction. In this example, tensor product of polynomials are also used as local approximating function for the purpose of comparison. Figure 2.22 show the efficiency of new basis function. From those figures, we can find that traditional basis function creat largest error at the tip of the wedge, it also happens when we use traditional FEM method. But with new basis function, the

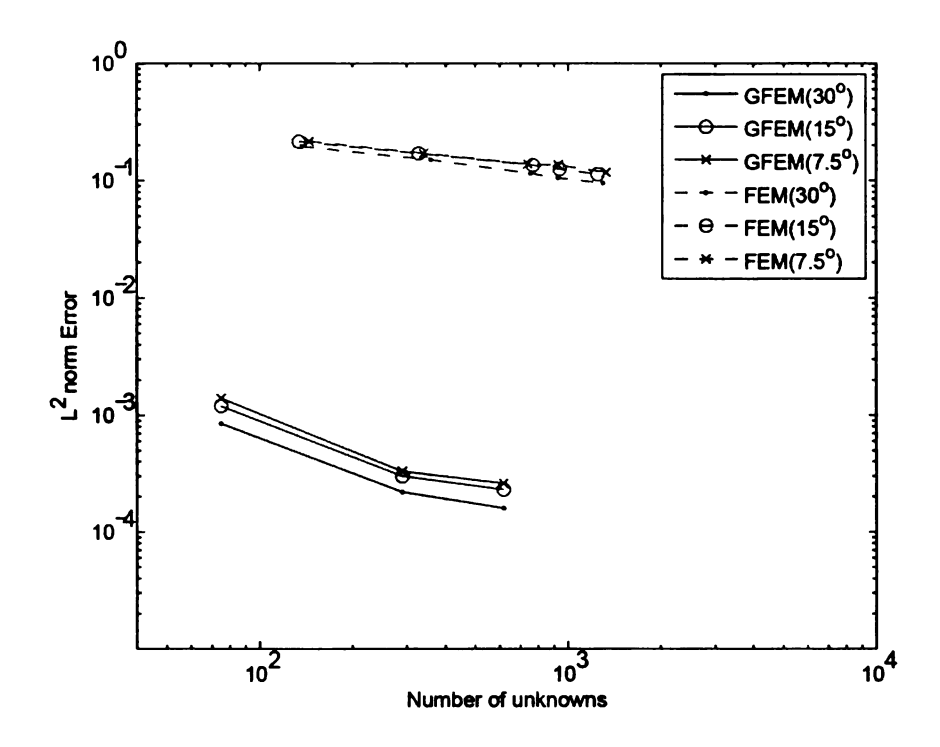


Figure 2.23. Error of FEM and GFEM solver

error aroung the tip of the wedge is reduced efficiently. Figure 2.21 show the relative error with respect to the number of unknowns. Obviously, error with new basis function convergence much faster than those with tradition basis functions.

Finally, we compare the error of scattering from wedge by GFEM solver and FEM solver. The parameters of the problem are mentioned following. The angle of wedge α is chosen as $\frac{\pi}{3}$, $\frac{\pi}{6}$ and $\frac{\pi}{12}$ respectively and the angle of incident field α_{in} is zero in all three cases. The relative error is computed by L^2 norm of error of E-field at 100×100 sample points which are uniformly distributed along x and y direction separately. Figure 2.23 shows the relative error of E field by GFEM and FEM solver with respect to the number of unknowns when the angle of wedge is changing. In GFEM, the number of modes in each patch is fixed to 6. We can see that the result of GFEM is much better than FEM. Figure 2.24, Figure 2.25 are error graph of FEM and GFEM. From Figure 2.24, The error in FEM around the

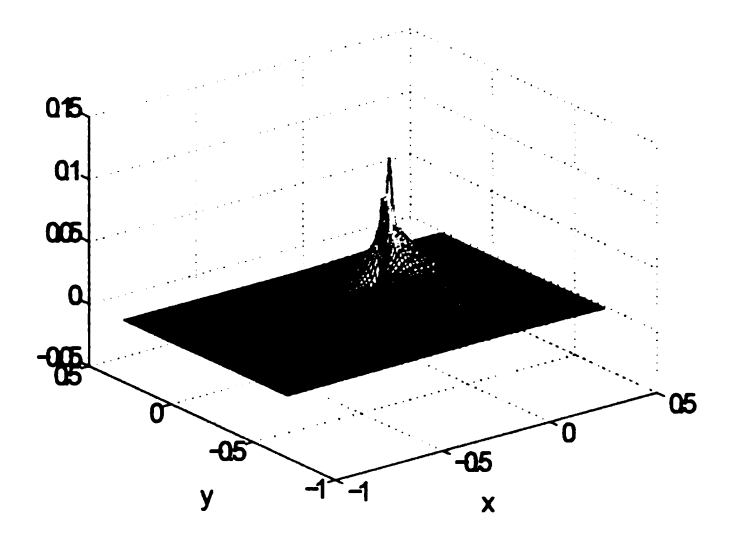


Figure 2.24. Error plot of FEM solver

tip of the wedge is much larger than the error at other place, at the same time, it doesn't happen in GFEM. The number of unknowns for FEM and GFEM is 1307 and 648 respectively. The angle α in both cases are $\frac{\pi}{24}$.

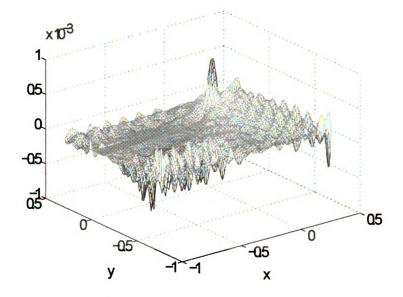


Figure 2.25. Error plot of GFEM solver

CHAPTER 3

VECTOR GENERALIZED FINITE ELEMENT METHOD

3.1 Introduction

While GFEM has been used for a range of problems [22, 44], it has not seen adaptation to address vector problem in high frequency electromagnetics. While some papers exist on application of a variation of GFEM to quasi-static problems whose governing equation is posed in terms of potentials, they do not address a fundamental difficulty: The boundary condition of the fields on the material interface require that their tangential component be continuous, their normal component be discontinuous and the normal derivatives of the tangential conditions be discontinuous as well. Achieving all of this using functions that are continuous across boundaries is almost impossible. Aside from this difficulty, it is also important for the divergence of the fields be zero (either in a strong or a weak sense). The latter was the principal motivating factor behind the development of vector basis functions [1] in classical FEM. As an aside, we note that this is not the first attempt at extending GFEM to analyze vector electromagnetics problems. That honor belongs to Tsukerman [32-37]. His treatment of the vector problem is largely inspired by that used in classical FEM. In Chapter V of [35], vector basis function is defined as $v\nabla\psi$ where ψ is barycentric coordinates, e.g. nodal basis function in FEM and shape function in GFEM, and v is polynomials. Though in FEM framework, this basis function coincide with the interpolatory high order edge element, in GFEM solver, $\nabla \psi$ equals zero in the region where there is only one patch as is this basis function. Except for this problem, he created basis functions that have zero divergence. But they cannot handle discontinuities in the constitutive parameters. Furthermore, he did not demonstrate the convergence characteristics of his scheme and only solved one eigenvalue problem by one patch where the shape of patch coincides with the shape of waveguide.

Another problem that bothers GFEM, as it also does any higher order solver is the condition number of the resulting system. Indeed, this is more of a problem here as opposed to classical FEM as the space of basis functions in GFEM is not interpolatory.

The objective of this chapter is to extend GFEM to address vector electromagnetics problems in both two and three dimensions. The principal contribution of this paper is three-fold:

- 1. We will develop two classes of vector basis functions for homogeneous domain and prove bounds on their convergence and the error bounds of linear operator.
- 2. We will develop basis functions that will enable the satisfaction of boundary conditions across interfaces. These conditions will be on the tangential components of the fields and their normal derivatives, and the normal component of the fields. In this chapter we restrict ourselves to planar and curved boundaries.
- 3. We will demonstrate h and p convergence of the proposed scheme for both Dirichlet and Neumann boundary conditions in two and three dimensional problems. We shall also demonstrate the accuracy of this scheme for computing eigenvalue for cavities, waveguides, and partially filled cavities.
- 4. We will demonstrate the inclusion of analytic behavior in the basis function space and the resulting improvements in convergence of fields. Our convergence studies will be restricted to near-field calculations.
- 5. We will propose a SVD-based preconditioner to reduced the condition number of the resulting system. The cost and error bound of the preconditioner will be derived. The reduced condition number and maintained accuracy will be demonstrated.

This chapter proceeds along the following lines; in the next three sections, we will introduce the construction of vector GFEM solver for homogeneous domain, piecewise homogeneous domain with planar interface and piecewise homogeneous with curved interface respectively. The accuracy and convergence of the GFEM solver will be demonstrated. In the last section, the SVD-based preconditioner will be introduced.

3.2 GFEM solver for homogeneous domain

3.2.1 Statement of the Problem

Consider a domain Ω whose boundary is denoted by $\partial\Omega := \Gamma = \bigcup_i \Gamma_i$. It is assumed that this domain is embedded in a domain Ω_e and its exterior boundary Γ_e is defined as $\Gamma_e := \Omega_e \cap \bar{\Omega}$. Interior to the domain Ω , the function $\mathbf{u}(\mathbf{r})$ satisfies

$$\left(\nabla \times \left[\frac{1}{\alpha(\mathbf{r})}\nabla \times\right] - \omega^2 \gamma(\mathbf{r})\right) \mathbf{u}(\mathbf{r}) = \mathbf{f}(\mathbf{r})$$

$$\mathcal{B}_i \left\{\mathbf{u}(\mathbf{r})\right\} = \mathbf{g}_i(\mathbf{r}) \text{ for } \mathbf{r} \in \Gamma_i$$
(3.1)

In these equation \mathbf{u} is used to denote either the electric or the magnetic field, $\alpha(\mathbf{r})$ and $\gamma(\mathbf{r})$ are position dependent constants, \mathcal{B}_i are differential operators, and $\mathbf{g}_i(\mathbf{r})$ is the function that is imposed on Γ_i . In the above equation, it is assumed that $\mathbf{r} \in \mathbb{R}^d$ where d=2,3. Solution to this problem for any imposed field $\mathbf{f}(\mathbf{r})$ can be obtained using classical vector FEM. This scheme requires tesselation of the underlying domain, and specifying an approximation space [1]. The approximation space is such that it satisfies the de-Rham map, and are based on a space of polynomials. The question that we intend posing is the development of a possible technique that permits development of scheme that does not rely on classical tesselation, permits the use of different kinds of basis functions in different regions of the domain Ω_e . As directly implementation of the scalar GFEM solver will results in the spurious problem, spurious-free vector GFEM solver need to be developed.

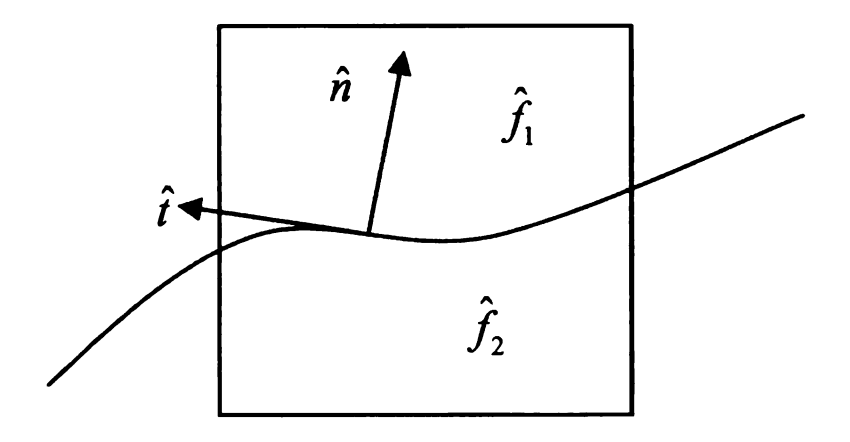


Figure 3.1. Patch cross the material interface

3.2.2 Basis functions

First, we examine the constraints that we need to impose on vector basis function. These condition emerge from Maxwell's equations and they are: (i) in a source free region, the field is divergence free, and (ii) at the interface between two media, the tangential component of the field is continuous and the normal component is discontinuous, and (iii) the normal derivatives of the tangential components are discontinuous as well. As we shall demonstrate in the Section 3.3.3, satisfaction of the last constraint is crucial achieving h— and p— convergence. Next, we will prove those constraints for vector function space.

Theorem 3.1 Figure 3.1 shows a patch with a material interface cross it. The constitutive parameters are ϵ_1 and ϵ_2 which are different from each other. Tangential and normal directions on the interface are defined as $\hat{\mathbf{t}}$ and $\hat{\mathbf{n}}$ respectively. $\mathbf{f_1}$ and $\mathbf{f_2}$ are vector local approximation in each region. The criteria of the local approximation

function can be described as followings:

$$\mathbf{f}_{1t} = \mathbf{f}_{2t}$$

$$f_{1n} \neq f_{2n}$$

$$\partial_n^l \mathbf{f}_{1t} \neq \partial_n^l \mathbf{f}_{2t} \quad l = 1, 2, 3...$$

$$\partial_n^l f_{1n} \neq \partial_n^l f_{2n} \quad l = 2, 3...$$

$$\nabla \cdot \mathbf{f}_1 = 0$$

$$\nabla \cdot \mathbf{f}_2 = 0$$
(3.2)

$$\nabla \cdot \mathbf{E}_1 = 0$$

$$\nabla \cdot \mathbf{E}_2 = 0$$

$$\mathbf{E}_{1t} = \mathbf{E}_{2t}$$
(3.3)

The above properties of the field require the following properties of the vector local approximation

$$\mathbf{f}_{1t} = \mathbf{f}_{2t}$$

$$\nabla \cdot \mathbf{f}_1 = 0$$

$$\nabla \cdot \mathbf{f}_2 = 0$$
(3.4)

From the condition

$$\epsilon_1 E_{1n} = \epsilon_2 E_{2n}$$

$$\epsilon_1 \neq \epsilon_2$$
(3.5)

It's easy to derive the criteria

$$f_{1n} \neq f_{2n} \tag{3.6}$$

We also can obtain the criteria

$$\partial_n f_{1n} = \nabla \cdot \mathbf{f}_1 - \nabla_t \cdot \mathbf{f}_{1t}$$

$$= \nabla \cdot \mathbf{f}_2 - \nabla_t \cdot \mathbf{f}_{2t}$$

$$= \partial_n f_{2n}$$
(3.7)

While the above criteria is important to construct high order vector local approximation, it's not independent.

When proving the following criteria, we can provide one simple example. As the field has the following discontinuities, the local approximation should share the same properties.

$$\partial_n^l \mathbf{f}_{1t} \neq \partial_n^l \mathbf{f}_{2t} \quad l = 1, 2, 3...$$

$$\partial_n^l f_{1n} \neq \partial_n^l f_{2n} \quad l = 2, 3...$$
(3.8)

In what follows, we start with defining basis functions in homogeneous domains and then proceed to extend this for domains that contain inhomogeneities. We shall also derive error bounds when using this span of functions. It is well known that a vector function can be expressed using a set of three wave functions that are typically denoted using $\mathbf{L}(\mathbf{r})$, $\mathbf{M}(\mathbf{r})$ and $\mathbf{N}(\mathbf{r})$ [57, 62]. These function are expressed using $\mathbf{L}(\mathbf{r}) = \nabla [\phi_l(\mathbf{r})]$, $\mathbf{M}(\mathbf{r}) = \nabla \times [\hat{c}\phi_m(\mathbf{r})]$, and $\mathbf{N}(\mathbf{r}) = 1/\kappa\nabla \times \nabla \times [\hat{c}\phi_n(\mathbf{r})]$, where $\phi_q(\mathbf{r})$ for q = l, m, n satisfy the Helmholz equation with wave number κ , and \hat{c} is a pilot vector. In a source free region, functions $\mathbf{M}(\mathbf{r})$ and $\mathbf{N}(\mathbf{r})$ are sufficient to represent the fields everywhere in the region. These fact sets the stage for the development of vector basis function for GFEM.

Assume that in any volumina $\phi_q(\mathbf{r}) \approx \phi_{ap}(\mathbf{r}) = span\{V_{i,q}\}$ for i=1,n where the subscript ap denotes an approximation to the continuous function and

 $V_i = \psi(\mathbf{r})v_i(\mathbf{r})$. It follows that one can envision, two different basis function: $\mathbf{u}_{ap}^1 \in \mathbf{V}^1 = span\left\{\psi(\mathbf{r})\nabla \times \left[\hat{c}v_{i,m}^{h,p}\right], \psi(\mathbf{r})\nabla \times \nabla \times \left[\hat{c}v_{i,n}^{h,p}\right]\right\}$, and $\mathbf{u}_{ap}^2 \in \mathbf{V}^2 = span\left\{\nabla \times \left[\hat{c}\psi(\mathbf{r})v_{i,m}^{h,p}\right], \nabla \times \nabla \times \left[\hat{c}\psi(\mathbf{r})v_{i,n}^{h,p}\right]\right\}$. From the definition of these approximations, it follows that for the approximation to be of order p, the highest order of the function $v_{i,m}^{h,p}$ should be of order p+1 whereas $v_{i,n}^{h,p}$ should be of order p+2. In this paper, these functions are chosen depending on the problem being analyzed. The definition of these basis functions also dictates that \mathbf{u}_{ap}^2 has zero divergence where as \mathbf{u}_{ap}^1 does not. To visualize these functions better, we plot two dimensional local approximation function $\nabla \times \left[\hat{c}v_{i,m}^{h,p}\right]$ with \hat{c} along the \hat{c} direction (or along the direction of invariance). These plots are displayed in the Figure 3.2, and as is evident from these figures, different modes approximate curls to different degrees.

When evaluating the terms $\nabla \times \mathbf{u}$ and $\nabla \cdot \mathbf{u}$ for the first basis function, the following formula is implemented.

$$\nabla \times \mathbf{u}_{i}^{n} = \nabla \times \left(\frac{\mathcal{W}_{i}}{\sum_{\Omega_{k} \in C_{i}} \mathcal{W}_{k}} \mathbf{v}_{i}^{n}\right)$$

$$= \nabla \left(\frac{\mathcal{W}_{i}}{\sum_{\Omega_{k} \in C_{i}} \mathcal{W}_{k}}\right) \times \mathbf{v}_{i}^{n} + \frac{\mathcal{W}_{i}}{\sum_{\Omega_{k} \in C_{i}} \mathcal{W}_{k}} \nabla \times \mathbf{v}_{i}^{n}$$

$$= \frac{\nabla \mathcal{W}_{i} \sum_{\Omega_{k} \in C_{i}} \mathcal{W}_{k} - \mathcal{W}_{i} \sum_{\Omega_{k} \in C_{i}} \nabla \mathcal{W}_{k}}{\left(\sum_{\Omega_{k} \in C_{i}} \mathcal{W}_{k}\right)^{2}} \times \mathbf{v}_{i}^{n}$$

$$+ \frac{\mathcal{W}_{i}}{\sum_{\Omega_{k} \in C_{i}} \mathcal{W}_{k}} \nabla \times \mathbf{v}_{i}^{n}$$

$$(3.9)$$

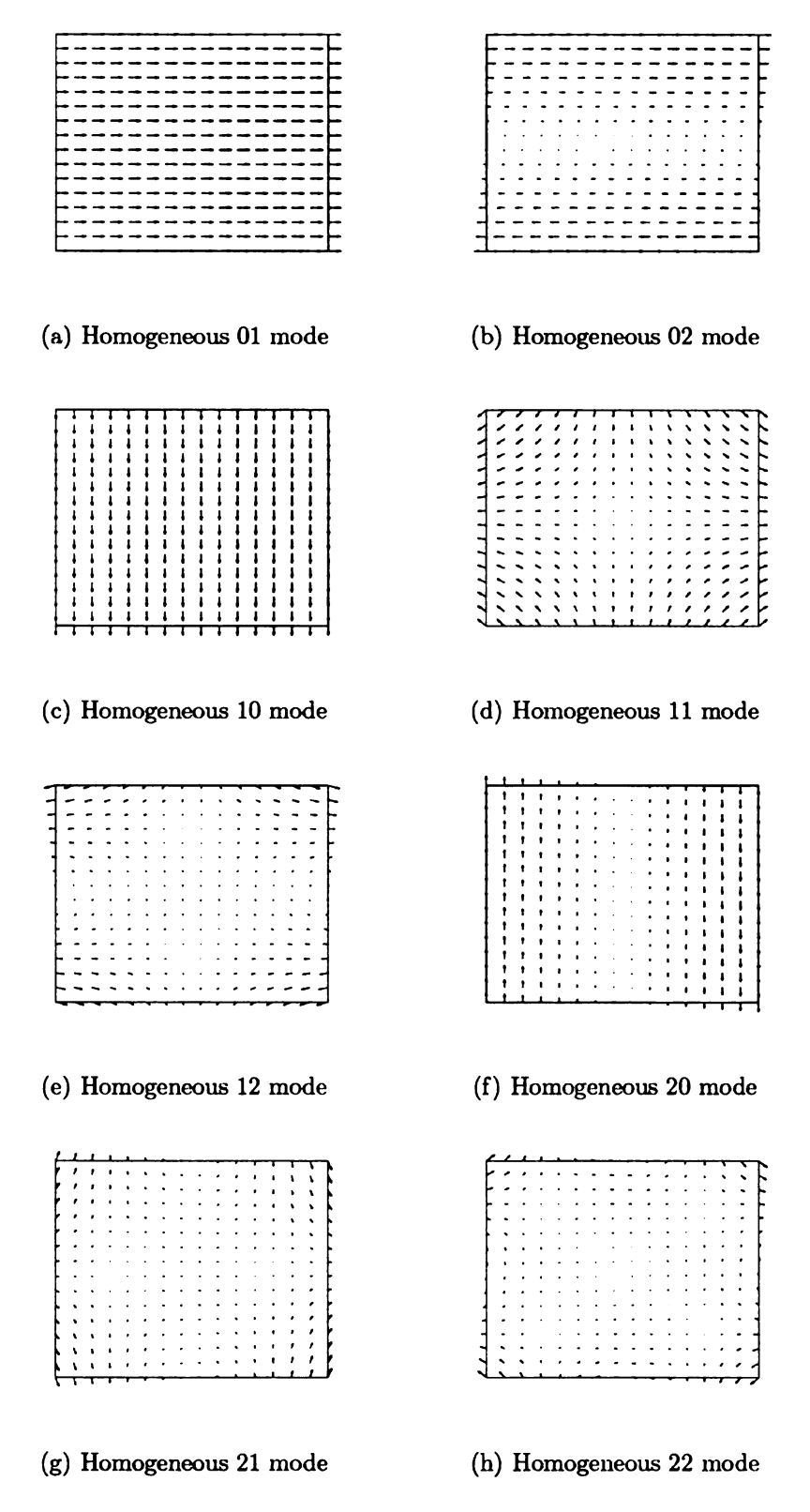


Figure 3.2. Vector plots of homogeneous local approximation function \mathbf{v}_i

$$\nabla \cdot \mathbf{u}_{i}^{n} = \nabla \cdot \left(\frac{\mathcal{W}_{i}}{\sum_{\Omega_{k} \in C_{i}} \mathcal{W}_{k}} \mathbf{v}_{i}^{n}\right)$$

$$= \frac{\mathcal{W}_{i}}{\sum_{\Omega_{k} \in C_{i}} \mathcal{W}_{k}} \nabla \cdot \mathbf{v}_{i}^{n} + \nabla \left(\frac{\mathcal{W}_{i}}{\sum_{\Omega_{k} \in C_{i}} \mathcal{W}_{k}}\right) \cdot \mathbf{v}_{i}^{n}$$

$$= \frac{\nabla \mathcal{W}_{i} \sum_{\Omega_{k} \in C_{i}} \mathcal{W}_{k} - \mathcal{W}_{i} \sum_{\Omega_{k} \in C_{i}} \nabla \mathcal{W}_{k}}{\left(\sum_{\Omega_{k} \in C_{i}} \mathcal{W}_{k}\right)^{2}} \cdot \mathbf{v}_{i}^{n}$$

$$(3.10)$$

In the above formula, \mathbf{v}_i^n denotes vector local approximation from the first kind of basis function \mathbf{u}_{ap}^1 and belong to the function space $span\left\{\nabla\times\left[\hat{c}v_{i,m}^{h,p}\right],\nabla\times\nabla\times\left[\hat{c}v_{i,n}^{h,p}\right]\right\}$. The above formula indicates that only \mathbf{v}_i^n and $\nabla\times\mathbf{v}_i^n$ are necessary to implement the bilinear form of the equation. Next, we derive error bounds for each of these approximating span of functions as applied to vector electromagnetic problems.

3.2.3 Error bound

3.2.3.0.1 Error bounds of basis functions: The global accuracy of the finite element method depends on the local accuracy of the approximation to the solution. Thus, predicting the local error bound yields the global error bound of the solver. In what follows, we derive error bounds for both types of approximations presented earlier: \mathbf{u}_{ap}^1 and \mathbf{u}_{ap}^2

Theorem 3.2 If

$$\begin{aligned} & \left\| \psi_{i}^{h} \right\|_{L^{\infty}} \leq C_{\infty(\Omega)} \\ & \left\| \nabla \psi_{i}^{h} \right\|_{L^{\infty}(\Omega)} \leq \frac{C_{\nabla}}{diam(\Omega_{i}^{h})} \\ & \left\| \nabla \times \left[\left(\phi_{m} - v_{i,m}^{h,p} \right) \hat{c} \right] \right\|_{L^{2}(\Omega \cap \Omega_{i})} \leq \epsilon_{1}(i,h,p) \\ & \left\| \nabla \times \nabla \times \left[\left(\phi_{n} - v_{i,n}^{h,p} \right) \hat{c} \right] \right\|_{L^{2}(\Omega \cap \Omega_{i})} \leq \epsilon_{2}(i,h,p) \\ & \exists M \in N \ \forall \mathbf{r} \in \Omega \ card\{i \mid \mathbf{r} \in \Omega_{i}\} \leq M \end{aligned}$$

$$(3.11)$$

Then the error is bounded by

$$\left\|\mathbf{u} - \mathbf{u}_{ap}^{1}\right\|_{L^{2}} \leq \sqrt{2M} C_{\infty} \left[\sum_{i} \epsilon_{1}^{2}(i, h, p) + \sum_{i} \epsilon_{2}^{2}(i, h, p)\right]^{1/2}$$
(3.12)

where C_{∞} and C_{∇} are constant. ϵ_1 and ϵ_2 are bounds of error of local approximating function in each patch.

Proof:

$$\begin{aligned} & \left\| \mathbf{u} - \mathbf{u}_{ap}^{1} \right\|_{L^{2}(\Omega)}^{2} \\ &= \left\| \left[\nabla \times (\phi_{m}\hat{c}) + \nabla \times \nabla \times (\phi_{n}\hat{c}) \right] - \sum_{i} \psi_{i} \left[\nabla \times \left(v_{i,m}^{h,p} \hat{c} \right) + \nabla \times \nabla \times \left(v_{i,n}^{h,p} \hat{c} \right) \right] \right\| \\ &= \left\| \sum_{i} \psi_{i} \left[\nabla \times \left(\left\{ \phi_{m} - v_{i,m}^{h,p} \hat{c} \right\} \right) \right] + \sum_{i} \psi_{i} \left[\nabla \times \nabla \times \left(\left\{ \phi_{n} - v_{i,n}^{h,p} \hat{c} \right\} \right) \right] \right\|_{L^{2}(\Omega)}^{2} \\ &\leq 2 \left\| \sum_{i} \psi_{i} \left[\nabla \times \left(\left\{ \phi_{m} - v_{i,m}^{h,p} \right\} \hat{c} \right) \right] \right\|_{L^{2}(\Omega)}^{2} \\ &+ 2 \left\| \sum_{i} \psi_{i} \left[\nabla \times \nabla \times \left(\left\{ \phi_{n} - v_{i,m}^{h,p} \right\} \hat{c} \right) \right] \right\|_{L^{2}(\Omega)}^{2} \\ &\leq 2M \sum_{i} \left\| \psi_{i} \left[\nabla \times \left(\left\{ \phi_{m} - v_{i,m}^{h,p} \right\} \hat{c} \right) \right] \right\|_{L^{2}(\Omega \cap \Omega_{i})}^{2} \\ &+ 2M \sum_{i} \left\| \psi_{i} \left[\nabla \times \nabla \times \left(\left\{ \phi_{n} - v_{i,m}^{h,p} \right\} \hat{c} \right) \right] \right\|_{L^{2}(\Omega \cap \Omega_{i})}^{2} \\ &\leq 2M C_{\infty}^{2} \sum_{i} \left[\epsilon_{1}^{2}(i,h,p) + \epsilon_{2}^{2}(i,h,p) \right] \end{aligned} \tag{3.13}$$

Theorem 3.3 If

$$\begin{aligned} & \left\| \psi_{i}^{h} \right\|_{L^{\infty}} \leq C_{\infty(\Omega)} \\ & \left\| \nabla \psi_{i}^{h} \right\|_{L^{\infty}(\Omega)} \leq \frac{C_{\nabla}}{diam(\Omega_{i}^{h})} \\ & \left\| \phi_{m} - v_{i,m}^{h,p} \right\|_{L^{2}(\Omega \cap \Omega_{i})} \leq \epsilon_{1}(i,h,p) \\ & \left\| \nabla \times \left[\left(\phi_{m} - v_{i,m}^{h,p} \right) \hat{c} \right] \right\|_{L^{2}(\Omega \cap \Omega_{i})} \leq \epsilon_{2}(i,h,p) \end{aligned}$$

$$\exists M \in N \ \forall \mathbf{r} \in \Omega \ card\{i \mid \mathbf{r} \in \Omega_{i}\} \leq M$$
 (3.14)

then the error is bounded by

$$\left\| \mathbf{u} - \mathbf{u}_{ap}^{2} \right\|_{L^{2}} \leq \sqrt{2M} \left[\sum_{i} C_{\infty}^{2} \epsilon_{2}^{2}(i, h, p) + \sum_{i} \frac{C_{\nabla}^{2}}{(diag\Omega_{i}^{h})^{2}} \epsilon_{1}^{2}(i, h, p) \right]^{1/2}$$
(3.15)

where C_{∞} and C_{∇} are constant, and ϵ_1 and ϵ_2 are error of local approximating functions .

Proof:

$$\begin{aligned} & \left\| \mathbf{u} - \mathbf{u}_{ap}^{2} \right\|_{L^{2}(\Omega)}^{2} \\ &= \left\| \nabla \times \left[\sum_{i} \psi_{i} \left(\left\{ \phi_{m} - v_{i,m}^{h,p} \right\} \hat{c} \right) \right] \right\|_{L^{2}(\Omega)}^{2} \\ &= \left\| \sum_{i} \left[\psi_{i} \nabla \times \left(\left\{ \phi_{m} - v_{i,m}^{h,p} \right\} \hat{c} \right) - \left(\left\{ \phi_{m} - v_{i,m}^{h,p} \right\} \hat{c} \right) \times \nabla \psi_{i} \right] \right\|_{L^{2}(\Omega)}^{2} \\ &\leq 2M \sum_{i} \left\| \psi_{i} \nabla \times \left(\left\{ \phi_{m} - v_{i,m}^{h,p} \right\} \hat{c} \right) \right\|_{L^{2}(\Omega \cap \Omega_{i})}^{2} \\ &+ 2M \sum_{i} \left\| \left(\left\{ \phi_{m} - v_{i,m}^{h,p} \right\} \hat{c} \right) \times \nabla \psi_{i} \right\|_{L^{2}(\Omega \cap \Omega_{i})}^{2} \\ &\leq 2M \left[C_{\infty}^{2} \sum_{i} \epsilon_{2}^{2}(i,h,p) + \frac{C_{\nabla}^{2}}{diam(\Omega_{i}^{h})^{2}} \sum_{i} \epsilon_{1}^{2}(i,h,p) \right] \end{aligned}$$

From the above equations, it appears that the space \mathbf{u}_{ap}^2 does not converge with decreasing h. However, it should be noted that ϵ_1 scales proportional to h. This implies that the rate convergence of this approximation w.r.t. both h and p is similar to that of \mathbf{u}_{ap}^1 . Note, using the above proof it can be shown that the basis functions proposed by Tsukerman will exhibit convergence characteristics similar to \mathbf{u}_{ap}^2 . The principal deficiency of \mathbf{u}_{ap}^2 is the fact that it cannot be easily extended to satisfy boundary conditions of fields across material interfaces whereas \mathbf{u}_{ap}^1 can be readily modified.

3.2.3.0.2 Error bound of bilinear operator: Next, we will show the error bound of the bilinear operator. As preliminary, we will assume the error bound of the following terms. If

$$\begin{aligned} & \left\| \psi_{i}^{h} \right\|_{L^{\infty}} \leq C_{\infty(\Omega)} \\ & \left\| \nabla \psi_{i}^{h} \right\|_{L^{\infty}(\Omega)} \leq \frac{C_{\nabla}}{\operatorname{diam}(\Omega_{i}^{h})} \\ & \left\| \nabla \times \left[\left(\phi_{m} - v_{i,m}^{h,p} \right) \hat{c} \right] \right\|_{L^{2}(\Omega \cap \Omega_{i})} \leq \epsilon_{1}(i,h,p) \\ & \left\| \nabla \times \nabla \times \left[\left(\phi_{n} - v_{i,n}^{h,p} \right) \hat{c} \right] \right\|_{L^{2}(\Omega \cap \Omega_{i})} \leq \epsilon_{2}(i,h,p) \\ & \left\| \nabla \times \nabla \times \left[\left(\phi_{m} - v_{i,m}^{h,p} \right) \hat{c} \right] \right\|_{L^{2}(\Omega \cap \Omega_{i})} \leq \epsilon_{3}(i,h,p) \\ & \left\| \nabla \times \nabla \times \nabla \times \left[\left(\phi_{n} - v_{i,m}^{h,p} \right) \hat{c} \right] \right\|_{L^{2}(\Omega \cap \Omega_{i})} \leq \epsilon_{4}(i,h,p) \\ & \left\| \nabla \times \nabla \times \nabla \times \left[\left(\phi_{n} - v_{i,n}^{h,p} \right) \hat{c} \right] \right\|_{L^{2}(\Omega \cap \Omega_{i})} \leq \epsilon_{4}(i,h,p) \\ & \exists M \in \mathbb{N} \ \, \forall \mathbf{r} \in \Omega \ \, \operatorname{card}\{i \mid \mathbf{r} \in \Omega_{i}\} \leq M \end{aligned}$$

Then the error of $\nabla \times \mathbf{u}_{ap}^1$ is bounded by

$$\left\| \nabla \times \mathbf{u} - \nabla \times \mathbf{u}_{ap}^{1} \right\|_{L^{2}}$$

$$\leq \sqrt{4M} \left[\sum_{i} \left\{ \epsilon_{1}^{2}(i, h, p) + \epsilon_{2}^{2}(i, h, p) \right\} C_{\infty}^{2} \right]$$

$$+ \sum_{i} \left\{ \epsilon_{3}^{2}(i, h, p) + \epsilon_{4}^{2}(i, h, p) \right\} \frac{C_{\nabla}^{2}}{diam(\Omega_{i}^{h})^{2}} \right]^{\frac{1}{2}}$$

$$(3.18)$$

where C_{∞} and C_{∇} are constant. ϵ_1 , and ϵ_2 are bounds of error of local approximation function in each patch. ϵ_3 , and ϵ_4 are error bounds of curl of local approximation function in each patch. If the order of scalar function ϕ_m and ϕ_n are p+1 and p+2, then we can approximate the function ϵ_1 , ϵ_2 , ϵ_3 and ϵ_4 as

$$\epsilon_{1}(i, h, p) \sim \mathcal{O}(h^{p})$$

$$\epsilon_{2}(i, h, p) \sim \mathcal{O}(h^{p})$$

$$\epsilon_{3}(i, h, p) \sim \mathcal{O}(h^{p-1})$$

$$\epsilon_{4}(i, h, p) \sim \mathcal{O}(h^{p-1})$$

$$diam(\Omega_{i}^{h}) \sim \mathcal{O}(h)$$
(3.19)

then

$$\left\| \nabla \times \mathbf{u} - \nabla \times \mathbf{u}_{ap}^{1} \right\|_{L^{2}} \sim \mathcal{O}(h^{p-1})$$
 (3.20)

Proof:

$$\begin{split} & \left\| \nabla \times \mathbf{u} - \nabla \times \mathbf{u}_{ap}^{1} \right\|_{L^{2}(\Omega)}^{2} \\ = & \left\| \nabla \times \left[\sum_{i} \psi_{i} \left(\nabla \times \left(\left\{ \phi_{m} - v_{i,m}^{h,p} \hat{c} \right\} \right) \right) \right] \right. \\ & + \left. \nabla \times \left[\sum_{i} \psi_{i} \left(\nabla \times \nabla \times \left(\left\{ \phi_{n} - v_{i,n}^{h,p} \hat{c} \right\} \right) \right) \right] \right\|_{L^{2}(\Omega)}^{2} \\ \leq & \left\| \nabla \times \left[\sum_{i} \psi_{i} \left(\nabla \times \left(\left\{ \phi_{m} - v_{i,m}^{h,p} \hat{c} \right\} \right) \right) \right] \right\|_{L^{2}(\Omega)}^{2} \\ & + 2 \left\| \nabla \times \left[\sum_{i} \psi_{i} \left(\nabla \times \nabla \times \left(\left\{ \phi_{n} - v_{i,n}^{h,p} \hat{c} \right\} \right) \right) \right] \right\|_{L^{2}(\Omega)}^{2} \\ \leq & 4 \left\| \sum_{i} \psi_{i} \left(\nabla \times \nabla \times \left(\left\{ \phi_{m} - v_{i,m}^{h,p} \hat{c} \right\} \right) \right) \right\|_{L^{2}(\Omega)}^{2} \\ & + 4 \left\| \sum_{i} \nabla \times \left(\left\{ \phi_{m} - v_{i,m}^{h,p} \hat{c} \right\} \times \nabla \psi_{i} \right\|_{L^{2}(\Omega)}^{2} \\ & + 4 \left\| \sum_{i} \psi_{i} \left(\nabla \times \nabla \times \nabla \times \left(\left\{ \phi_{n} - v_{i,n}^{h,p} \hat{c} \right\} \right) \right) \right\|_{L^{2}(\Omega)}^{2} \\ & + 4 \left\| \sum_{i} \nabla \times \nabla \times \left(\left\{ \phi_{n} - v_{i,m}^{h,p} \hat{c} \right\} \times \nabla \psi_{i} \right\|_{L^{2}(\Omega)}^{2} \\ & \leq & 4M \sum_{i} \left\| \psi_{i} \left(\nabla \times \nabla \times \left(\left\{ \phi_{m} - v_{i,m}^{h,p} \hat{c} \right\} \right) \right) \right\|_{L^{2}(\Omega \cap \Omega_{i})}^{2} \\ & + & 4M \sum_{i} \left\| \nabla \times \left(\left\{ \phi_{m} - v_{i,m}^{h,p} \hat{c} \right\} \times \nabla \psi_{i} \right\|_{L^{2}(\Omega \cap \Omega_{i})}^{2} \\ & + & 4M \sum_{i} \left\| \nabla \times \nabla \times \left(\left\{ \phi_{n} - v_{i,n}^{h,p} \hat{c} \right\} \times \nabla \psi_{i} \right\|_{L^{2}(\Omega \cap \Omega_{i})}^{2} \right. \\ & + & 4M \sum_{i} \left\| \nabla \times \nabla \times \left(\left\{ \phi_{n} - v_{i,n}^{h,p} \hat{c} \right\} \times \nabla \psi_{i} \right\|_{L^{2}(\Omega \cap \Omega_{i})}^{2} \right. \\ & \leq & 4M \left[\sum_{i} \left\{ \epsilon_{3}^{2}(i,h,p) + \epsilon_{4}^{2}(i,h,p) \right\} C_{\infty}^{2} + \sum_{i} \left\{ \epsilon_{1}^{2}(i,h,p) + \epsilon_{2}^{2}(i,h,p) \right\} \frac{C_{\nabla}^{2}}{diam(\Omega_{i}^{h})^{2}} \right] \right. \end{aligned}$$

If we also have

$$\|\nabla \times \mathbf{v}_{i}\|_{L^{2}(\Omega \cap \Omega_{i})} \leq \epsilon_{5}(i, h, p)$$

$$\|\mathbf{v}_{i}\|_{L^{2}(\Omega \cap \Omega_{i})} \leq \epsilon_{6}(i, h, p)$$
(3.22)

Then the error of the linear operator is bounded by

$$\| (\nabla \times \mathbf{u}_{ap}^{1}) \cdot (\nabla \times \mathbf{v}) + \mathbf{u}_{ap}^{1} \cdot \mathbf{v} - (\nabla \times \mathbf{u}) \cdot (\nabla \times \mathbf{v}) - \mathbf{u} \cdot \mathbf{v} \|_{L^{2}(\Omega)}^{2}$$

$$\leq \left\{ 8M \sum_{i} f_{1}(i, h, p) \epsilon_{5}(i, h, p) + 4M C_{\infty}^{2} \sum_{i} f_{2}(i, h, p) \epsilon_{6}(i, h, p) \right\}^{1/2}$$

$$(3.23)$$

where

$$f_{1}(i,h,p) = \left\{ \epsilon_{3}^{2}(i,h,p) + \epsilon_{4}^{2}(i,h,p) \right\} C_{\infty}^{2} + \left\{ \epsilon_{1}^{2}(i,h,p) + \epsilon_{2}^{2}(i,h,p) \right\} \frac{C_{\nabla}^{2}}{diam(\Omega_{i}^{h})^{2}}$$

$$f_{2}(i,h,p) = \epsilon_{1}^{2}(i,h,p) + \epsilon_{2}^{2}(i,h,p)$$
(3.24)

If we assume that

$$\epsilon_5(i, h, p) \sim \mathcal{O}(1/h)$$

$$\epsilon_6(i, h, p) \sim \mathcal{O}(1)$$
(3.25)

Then

$$\left\| (\nabla \times \mathbf{u}_{ap}^{1}) \cdot (\nabla \times \mathbf{v}) + \mathbf{u}_{ap}^{1} \cdot \mathbf{v} - (\nabla \times \mathbf{u}) \cdot (\nabla \times \mathbf{v}) - \mathbf{u} \cdot \mathbf{v} \right\|_{L^{2}(\Omega)}$$

$$\leq \left\{ 8M \sum_{i} f_{1}(i, h, p) \epsilon_{5}(i, h, p) + 4M C_{\infty}^{2} \sum_{i} f_{2}(i, h, p) \epsilon_{6}(i, h, p) \right\}^{1/2}$$

$$\sim \mathcal{O}(h^{(p-1)})$$
(3.26)

63

Proof:

$$\begin{split} & \left\| (\nabla \times \mathbf{u}_{ap}^{1}) \cdot (\nabla \times \mathbf{v}_{i}) + \mathbf{u}_{ap}^{1} \cdot \mathbf{v}_{i} - (\nabla \times \mathbf{u}) \cdot (\nabla \times \mathbf{v}_{i}) - \mathbf{u} \cdot \mathbf{v}_{i} \right\|_{L^{2}(\Omega)}^{2} \\ & \leq \left\| \left(\nabla \times \left\{ \mathbf{u}_{ap}^{1} - \mathbf{u} \right\} \right) \cdot (\nabla \times \mathbf{v}_{i}) - \left(\mathbf{u}_{ap}^{1} - \mathbf{u} \right) \cdot \mathbf{v}_{i} \right\|_{L^{2}(\Omega)}^{2} \\ & \leq 2 \left\| \left(\mathbf{u}_{ap}^{1} - \mathbf{u} \right) \cdot (\nabla \times \mathbf{v}_{i}) \right\|_{L^{2}(\Omega)}^{2} \\ & + 2 \left\| \left(\mathbf{u}_{ap}^{1} - \mathbf{u} \right) \cdot \mathbf{v}_{i} \right\|_{L^{2}(\Omega)}^{2} \\ & \leq 2 \left\| \nabla \times \left\{ \mathbf{u}_{ap}^{1} - \mathbf{u} \right\} \right\|_{L^{2}(\Omega)}^{2} \left\| \nabla \times \mathbf{v}_{i} \right\|_{L^{2}(\Omega)}^{2} \\ & \leq 2 \left\| \nabla \times \left\{ \mathbf{u}_{ap}^{1} - \mathbf{u} \right\} \right\|_{L^{2}(\Omega)}^{2} \left\| \nabla \times \mathbf{v}_{i} \right\|_{L^{2}(\Omega)}^{2} \\ & \leq 8M \left[\sum_{i} \left\{ \epsilon_{3}^{2}(i, h, p) + \epsilon_{4}^{2}(i, h, p) \right\} C_{\infty}^{2} \\ & + \sum_{i} \left\{ \epsilon_{1}^{2}(i, h, p) + \epsilon_{2}^{2}(i, h, p) \right\} \frac{C_{\nabla}^{2}}{diam(\Omega_{i}^{h})^{2}} \right] \epsilon_{5}(i, h, p) \\ & + 4MC_{\infty}^{2} \sum_{i} \left[\epsilon_{1}^{2}(i, h, p) + \epsilon_{2}^{2}(i, h, p) \right] \epsilon_{6}(i, h, p) \end{split}$$

3.2.4 Imposition of boundary conditions and the resulting bilinear form

As is evident from the preceding discussion, the basis functions are not interpolatory, nor do the domains conform to the boundary. While this fact does not affect the imposition of the Neumann boundary condition, imposition of the Dirichlet boundary conditions are not as simple as those for classical FEM. Methods that have been used to impose this condition included augmenting GFEM with classical methods at the boundary or using a Lagrange multiplier. Both these method are not stable as they do not satisfy the Babuska-Brezzi condition [52–54]. It can be shown that stable results may be obtained using either stabilized Lagrange multiplier technique or the Nitsche's method. We have used the latter with success for solving the scalar

Helmholtz equation as have others [55, 63]. In this paper, this technique is extended to vector electromagnetic fields. Thus, given (3.1) with

$$\mathbf{u}(\mathbf{r}) \times \hat{n} = \mathbf{g}_{d}(\mathbf{r}) \text{ for } \mathbf{r} \in \Gamma_{d}$$

$$\hat{n} \times (\nabla \times \mathbf{u}(\mathbf{r})) = \mathbf{g}_{n1}(\mathbf{r}) \text{ for } \mathbf{r} \in \Gamma_{n}$$

$$\mathbf{u}(\mathbf{r}) \cdot \hat{n} = q_{n2}(\mathbf{r}) \text{ for } \mathbf{r} \in \Gamma_{n}$$
(3.28)

where $\Gamma = \Gamma_d \cup \Gamma_n$ we need to find an approximation $\mathbf{u}_{ap}(\mathbf{r}) \in \mathbf{V}_n \subset H(\nabla \times, \Omega)$. It can be shown that the bilinear form for solving this problem may be written as

$$\mathcal{A}_{h}(\mathbf{u}, \mathbf{w}) = \mathcal{F}_{h}(\mathbf{w}) \ \forall \mathbf{w} \in \mathbf{V}_{n}$$

$$\mathcal{A}_{h}(\mathbf{u}, \mathbf{w}) = \int_{\Omega} d\Omega \ \frac{1}{\alpha(\mathbf{r})} \nabla \times \mathbf{u} \cdot \nabla \times \mathbf{w} - \omega^{2} \int_{\Omega} d\Omega \ \gamma(\mathbf{r}) \mathbf{u} \cdot \mathbf{w}$$

$$+ \beta_{1} \int_{\Gamma_{d}} d\Gamma \ (\mathbf{u} \times \hat{n}) \cdot (\mathbf{w} \times \hat{n}) + \alpha \int_{\Gamma_{d}} d\Gamma \ (\nabla \cdot \mathbf{u}) (\nabla \cdot \mathbf{w})$$

$$+ \int_{\Gamma_{d}} d\Gamma \ \frac{1}{\alpha(\mathbf{r})} (\mathbf{u} \times \hat{n}) \cdot (\nabla \times \mathbf{w}) + \int_{\Gamma_{d}} d\Gamma \ \frac{1}{\alpha(\mathbf{r})} (\mathbf{w} \times \hat{n}) \cdot (\nabla \times \mathbf{u})$$

$$+ \beta_{2} \int_{\Gamma_{n}} d\Gamma (\mathbf{u} \cdot \hat{n}) (\mathbf{w} \cdot \hat{n})$$

$$\mathcal{F}_{h}(\mathbf{w}) = \int_{\Omega} d\Omega \ \mathbf{f} \cdot \mathbf{w} + \int_{\Gamma_{d}} d\Gamma \ \frac{1}{\alpha(\mathbf{r})} \mathbf{g}_{d} \cdot (\nabla \times \mathbf{w}) + \beta_{1} \int_{\Gamma_{d}} d\Gamma \mathbf{g}_{d} \cdot (\mathbf{w} \times \hat{n})$$

$$+ \int_{\Gamma_{n}} d\Gamma \frac{1}{\alpha(\mathbf{r})} \mathbf{g}_{n1} \cdot \mathbf{w} + \beta_{2} \int_{\Gamma_{n}} d\Gamma g_{n2} (\mathbf{w} \cdot \hat{n})$$

$$(3.29)$$

In the above equation, β_1 is a constant that imposes the Dirichlet boundary condition using the Nitsche's method and makes the overall system coercive. The means estimate the value of β_1 follows those derived by [50]. The quantities associated with α and β_2 are regularization terms. We have found that these are not necessary when using approximation functions of the type \mathbf{u}_{ap}^2 but make the convergence curves smoother when used with approximation functions of the type \mathbf{u}_{ap}^1 .

3.2.5 Numerical experiments

In what follows, we shall present a series of numerical experiments that will serve to demonstrate the accuracy and convergence of the vector GFEM presented in this chapter. At first will focus on convergence issues related to problems in homogeneous domains. Then we shall demonstrate the versatility and convergence properties of this technique by studying scattering from a wedge using non-polynomial basis functions. In some of these numerical experiments we will demonstrate the relative convergence of both \mathbf{u}_{ap}^1 and \mathbf{u}_{ap}^2 .

First, consider a homogeneous rectangular computation domain, where the solution to the vector wave equation is assumed to be

$$\mathbf{u}(x,y) = 1.32\cos(1.76x)\cos(1.32y)\hat{x} + 1.76\sin(1.76x)\sin(1.32y)\hat{y}$$
(3.30)

in the domain $\Omega = (0,1)^2$ with boundary $\Gamma \bigcup_i^4 \Gamma_i$ where $\{\Gamma_1 : \mathbf{r} \in 0 \times (0,1)\}, \{\Gamma_2 : \mathbf{r} \in (0,1) \times 1\}, \{\Gamma_3 : \mathbf{r} \in 1 \times (0,1)\}, \{\Gamma_4 : \mathbf{r} \in (0,1) \times 0\}.$

This field is imposed on Γ as either a Neumann or Dirichlet boundary condition. The problem is then posed as (3.1). Given the geometry of the problem and the nature of solution, the approximation to the field in Ω can be written as $\mathbf{u}_{ap}^1 = span\left\{\psi_i(\mathbf{r})\nabla\times\left[\hat{c}v_{i,m}^{h,p}\right]\right\}$. In this experiment, all nodes are distributed uniformly, and rectangular patches are used. The size of each patch is chosen to be 1.5 times the distance between the nodes. Unless otherwise mentioned, all examples in this chapter are built in a similar manner. The weight functions $\mathcal{W}_i(\mathbf{r})$ is a tensor product rooftops, and the local approximation function $v_{i,m}(\mathbf{r})$ and $v_{i,n}(\mathbf{r})$ are tensor product of Legendre polynomials. Figure 3.3(a) shows the h, p convergence of GFEM when the Neumann boundary value problem is solved. Figure 3.3(b) shows h, p convergence for the Dirichlet boundary value problem. In the figures, the L^2 norm of relative error is evaluated at uniformly distributed 100×100 sample points. As is apparent, the technique shows excellent convergence.

Next, we solve the same problem for both boundary conditions. However, the approximation space will be $\mathbf{u}_{ap}^2 = span\left\{\nabla \times \left[\hat{c}\psi_i(\mathbf{r})v_{i,m}^{h,p}\right]\right\}$. All other parameters (size of the meshes, distribution of the nodes) are identical to those used earlier. As is evident from Figure 3.4, the error decrease with decrease in h and increase in p.

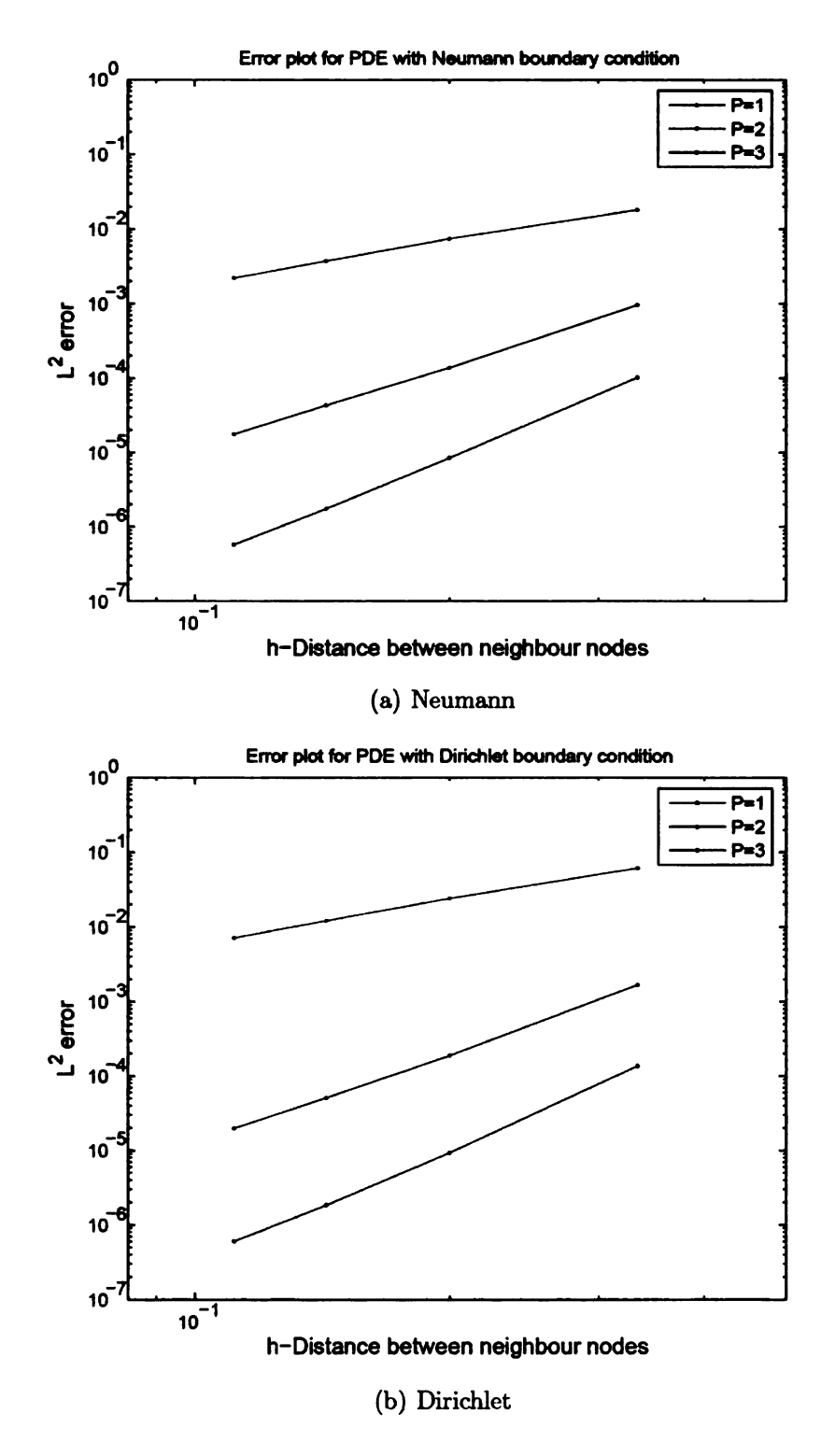


Figure 3.3. Convergence graphs for vector Neumann and Dirichlet BVPs by \mathbf{u}_{ap}^1

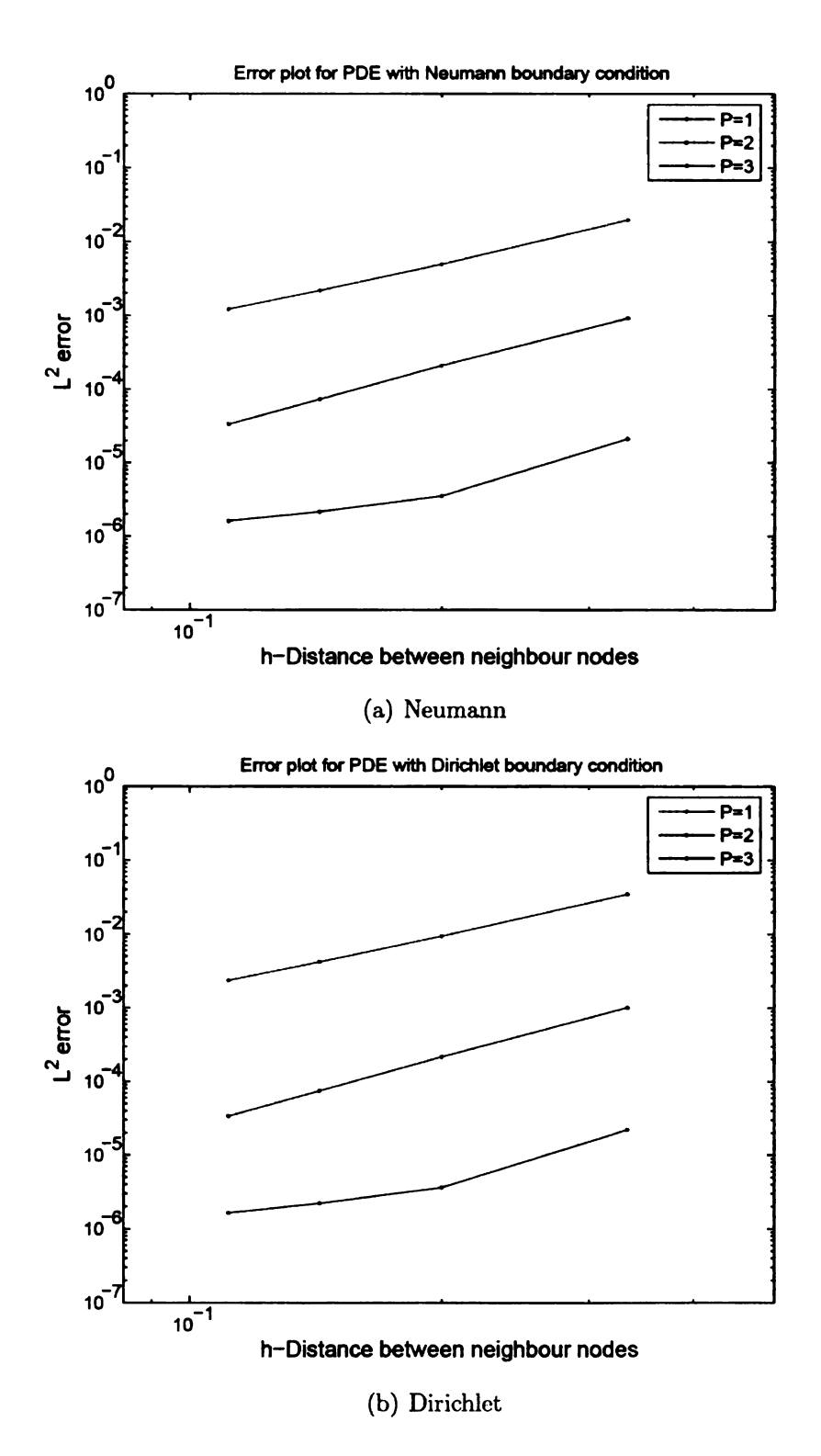


Figure 3.4. Convergence graphs for vector Neumann and Dirichlet BVPs by \mathbf{u}_{ap}^2

Next, we examine the accuracy of three dimensional vector basis function in homogeneous computation domain. The computational domain is $\Omega = (0,1)^3$ and it is also assumed that the field behavior in the domain is governed by

$$\mathbf{u}(x,y) = -19 * \cos(0.94x) \sin(1.26y) \sin(1.57z)\hat{x}$$

$$-17 * \sin(0.94x) \cos(1.26y) \sin(1.57z)\hat{y}$$

$$+25 * \sin(0.94x) \sin(1.26y) \cos(1.57z)\hat{z}$$
(3.31)

It is apparent from the above equations that both functions $\mathbf{M}(\mathbf{r})$ and $\mathbf{N}(\mathbf{r})$ are necessary to represent the field. Consequently, the function space chosen is $\mathbf{u}_{ap}^1 = span\left\{\psi_i(\mathbf{r})\nabla\times\left[\hat{c}v_{i,m}\right],\psi_i(\mathbf{r})\nabla\times\nabla\times\left[\hat{c}v_{i,n}\right]\right\}$. Again, all the parameters used in the computation are the same as those in 2D problems and are only extended to 3D. The L^2 norm of relative error is evaluated at $5\times5\times5$ uniformly distributed sample points. Figure 3.5 shows the h and p convergence of those vector basis.

The above results demonstrate h and p convergence, but the anticipated rate of convergence h^{2p} is not achieved. This said, it is worthwhile to note that the theoretical convergence rate is obtained from dispersion analysis and is appropriate for analyzing convergence of far fields as in RCS. But, the examples shown involve near field quantities. To illustrate convergence, we again consider a homogeneous domain $\Omega = (0,1)^3$. It is assumed that the field behavior in the domain is given by $\mathbf{u}(x,y) = \exp\{-j0.9425z\}\hat{y}$. All other parameters, viz., distribution of nodes, overlap, etc, are identical to those used earlier and as before the L^2 error norm is evaluated at $5 \times 5 \times 5$ uniformly distributed sample points. The convergence data is shown in Figure 3.6, and as is evident from this figure, the convergence for p=2 follows the predicted behavior. However, the curves for p=1 are a shade worse.

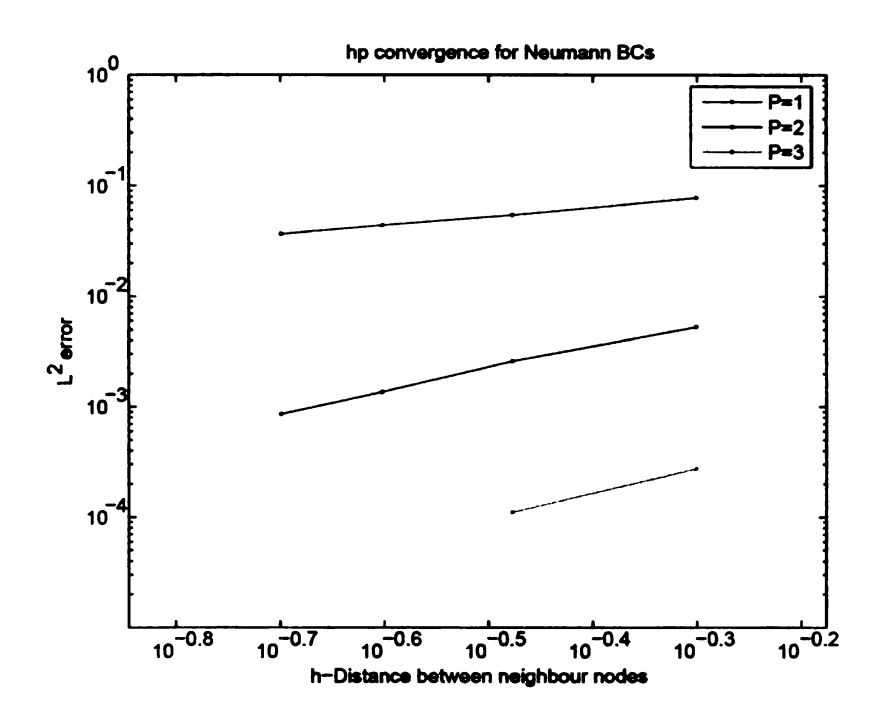


Figure 3.5. Convergence graphs for 3D homogeneous vector Neumann BVPs

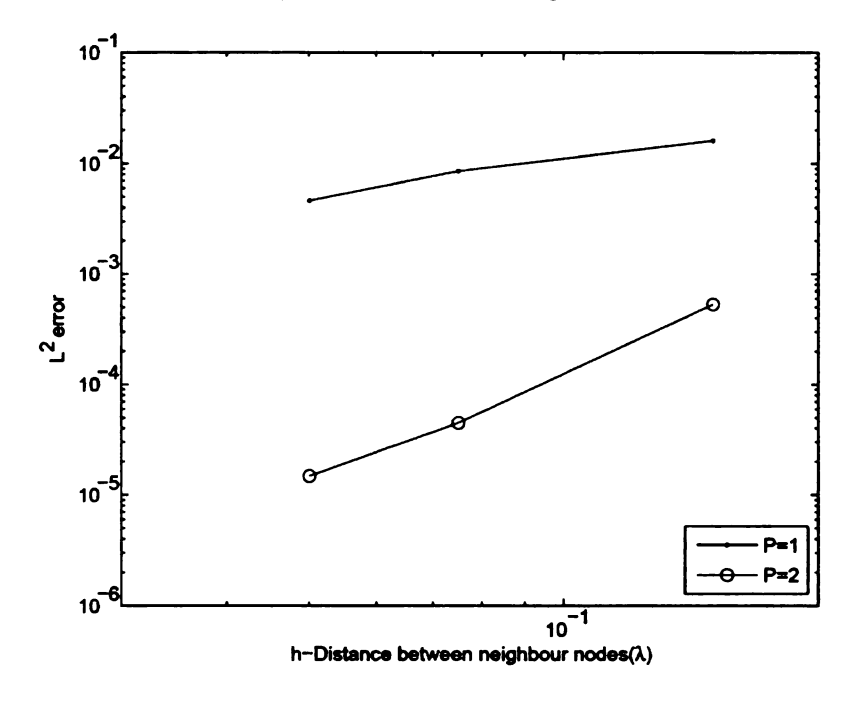


Figure 3.6. Convergence graphs for 3D homogeneous vector Neumann BVPs (Plane Wave)

TE	Principal Mode		p = 1	p = 2	p=3
		h = 1/4	0.0616	2.88e-4	2.82e-6
		h = 1/6	0.0297	6.17e-5	2.42e-7
	First 8	h = 1/4	0.1629	3.99e-3	1.65e-4
	modes	h = 1/6	0.0743	8.74e-4	1.21e-5
TM	Principal	h = 1/4	0.0182	2.75e-4	1.14e-6
	Mode	h = 1/6	9.93e-3	4.50e-5	1.08e-7
	First 8	h = 1/4	0.1674	0.0349	5.83e-4
	Modes	h = 1/6	0.0992	5.27e-3	1.12e-4

Table 3.1. Error in eigenvalues computed using \mathbf{u}_{ap}^{1}

TE	Principal Mode		p = 1	p=2	p=3
		h = 1/4	0.0206	1.17e-4	1.32e-7
		h = 1/6	8.88e-3	3.76e-5	4.52e-9
	First 8	h = 1/4	0.0697	1.31e-3	1.07e-5
	modes	h = 1/6	0.0263	3.81e-4	7.06e-7
ТМ	Principal	h = 1/4	7.13e-3	1.62e-4	6.82e-8
	Mode	h = 1/6	3.76e-3	3.66e-5	7.04e-9
	First 8	h = 1/4	0.1878	5.82e-3	3.97e-5
	Modes	h = 1/6	0.0420	1.89e-3	1.14e-5

Table 3.2. Error in eigenvalues computed using \mathbf{u}_{ap}^2

Next, we compute the eigenmodes in a rectangular waveguide. The dimensions of the waveguide are chosen to be $1m \times 1m$. The convergence data (error in L^2 norm) for both TE^z and TM^z modes are presented in the Table 3.1 and Table 3.2. The basis functions used in these experiments are for both \mathbf{u}_{ap}^1 and \mathbf{u}_{ap}^2 . As is evident from this data, the results obtained converge rapidly with increasing order and refinement. Furthermore, results obtained using basis functions of type \mathbf{u}_{ap}^2 converge faster than those obtained using \mathbf{u}_{ap}^1 .

Until now, the basis functions used in all the examples have been based on tensor products of polynomials. Here, we recomputer the scattering from a wedge

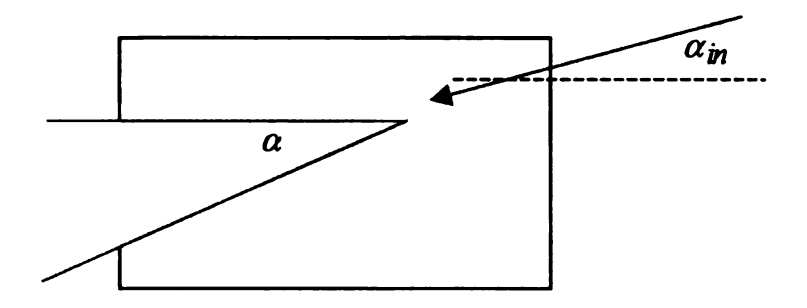


Figure 3.7. Geometric description of the wedge

in the last chapter. The problem can be solved as vector problem when magnetic field $\mathbf{H}(\mathbf{r})$ is computed. In what follows, we will explicitly incorporate the known functional behavior. Consider a two dimensional wedge with angle $\frac{\pi}{6}$ that is located in a rectangular computational domain $\Omega = (-1.0, 0.5) \times (-0.7, 0.3)$. The tip of the wedge coincides with the origin of the computational domain and one side lies in the y = 0 plane. A field that is polarized along the \hat{z} and propagating along $\hat{k} = -0.9659\hat{x} - 0.2588\hat{y}$ is incident upon the wedge, and the wavenumber $k_0 = 3$; this geometric configuration is shown in Figure 3.7. It can be easily shown that the fields are given by

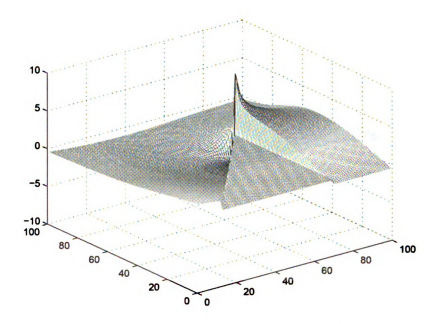
$$\mathbf{H(r)} = \nabla \times \mathbf{E(r)}$$

$$E_z = \frac{4\pi E_0}{2\pi - \alpha} \sum_{v} j^v J_v(k\rho) sin[v(\alpha_{in} + \pi - \alpha)] sin[v(\phi + \pi - \alpha)]$$

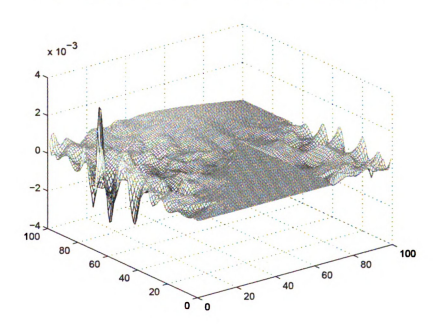
$$v = \frac{m\pi}{2\pi - \alpha} \qquad m = 1, 2, \cdots$$
(3.32)

To solve this problem using GFEM, we use $J_v(k\rho)sin[v(\phi + \pi - \alpha)]$ to create the function space $v_{i,m}$. The infinite extent of the wedge is simulated by imposing analytical solutions for the infinite wedge as Dirichlet boundary conditions. The

relative error is computed using L^2 norm of error in the electric field at 100×100 sample points that are uniformly distributed along \hat{x} and \hat{y} direction. Figure 3.8, Figure 3.9 shows the analytical solution and the graph of error when the number of patches is 12×9 and the number of modes in one patch is 7. From this figure, it is apparent that this scheme captures the field behavior extremely well at all points in the computational domain, and as is to be expected, the results are excellent at the tip. Graph of error shows that the overall error in the domain is dominated by that on the boundary. Finally, Figure 3.10 shows the relative error with respect to the number of unknowns, where m is the number of modes used for the local approximation in one patch.

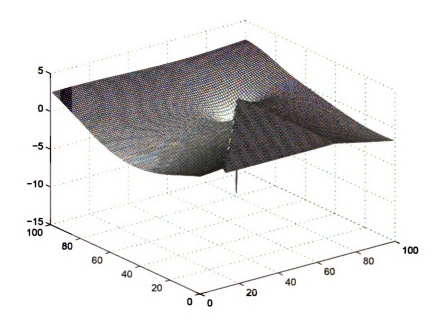


(a) \hat{x} component of the magnetic field (obtained analytically)

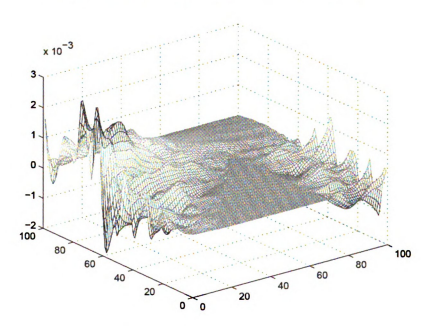


(b) Error in the \hat{x} component

Figure 3.8. Analytical result for scattering from a wedge and error plot for y componnet



(a) \hat{y} component of the magnetic field (obtained analytically)



(b) Error in the \hat{y} component

Figure 3.9. Analytical result for scattering from a wedge and error plot for y component

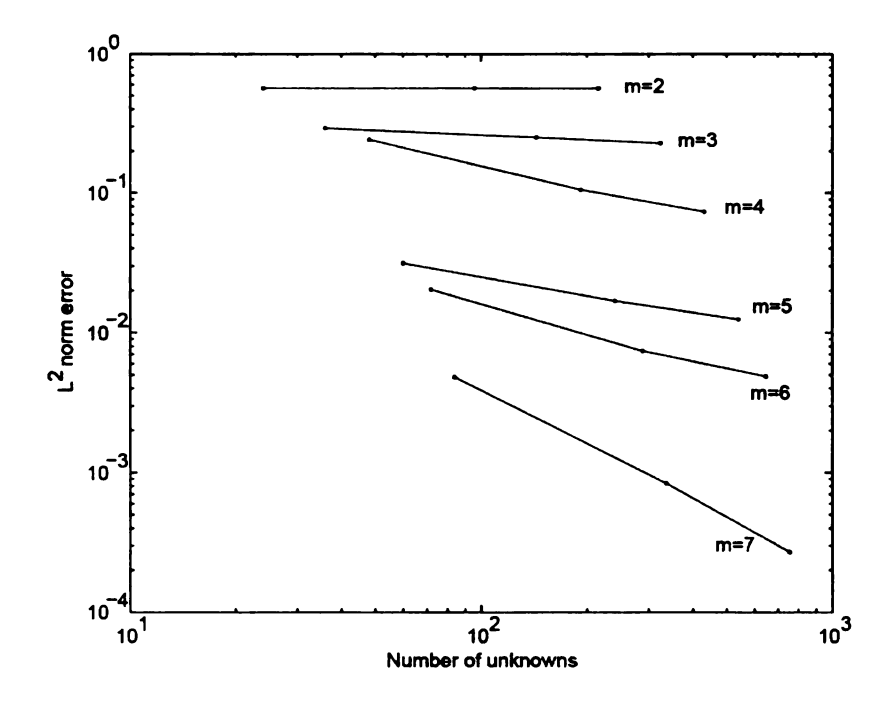


Figure 3.10. $h,\,p$ convergence for wedge problem

3.3 GFEM solver for piecewise homogeneous domain with flat interface

3.3.1 Basis function

The basis functions defined earlier are continuous as are its derivatives. While these basis functions are ideal for modeling fields in a homogeneous domains, it is apparent that these are far from satisfactory when the domain comprises of a material discontinuity. Ideally, the approximation space should consist of functions whose normal components are discontinuous and whose normal derivatives of the tangential components are discontinuous as well. To address this problem, consider a domain $\Omega_i = \Omega_i^+ \cup \Omega_i^-$ and $\Gamma_i^\pm = \partial \Omega_i^+ \cap \partial \Omega_i^-$. The dielectric properties in Ω_i^\pm are assumed to be different as shown in Figure 3.11. In what follows, Γ is assumed to be planar, the unit normal vector to this boundary is denoted by $\hat{\zeta}$, and the boundary is defined by the plane $\Gamma = \zeta_0 \hat{\zeta}$. Assume that the local approximation functions, $\left\{ \nabla \times \left(\hat{\zeta} v_{i,m}^{h,p} \right), \nabla \times \nabla \times \left(\hat{\zeta} v_{i,n}^{h,p} \right) \right\}$, are augmented by two functions $\mathbf{f}_i^+(\mathbf{r})$ and $\mathbf{f}_i^-(\mathbf{r})$ with $supp\left\{ \mathbf{f}_i^+(\mathbf{r}) \right\} = \Omega_i^+$ and $supp\left\{ \mathbf{f}_i^-(\mathbf{r}) \right\} = \Omega_i^-$. Next, we derive the characteristics of these functions $\forall \mathbf{r} \in \Gamma_i^\pm$.

Prior to doing so, we define the following: $\mathbf{r} = \boldsymbol{\rho} + \zeta \hat{\zeta}$, $\nabla = \nabla_{\rho} + \partial_{\zeta} \hat{\zeta}$ and $\mathbf{f}_{i}^{\alpha}(\mathbf{r}) = \mathbf{f}_{i\rho}^{\alpha} + \hat{\zeta} f_{i\zeta}^{\alpha}$ for $\alpha = \pm$. Operations on these functions are defined as:

$$\mathbf{T}_{k}(\mathbf{r}) = \partial_{\zeta}^{k} \left(\mathbf{f}_{i\rho}^{+}(\mathbf{r}) - \mathbf{f}_{i\rho}^{-}(\mathbf{r}) \right) \quad \forall k = 1, 2, \cdots$$

$$N_{0}(\mathbf{r}) = f_{i\zeta}^{+}(\mathbf{r}) - f_{i\zeta}^{-}(\mathbf{r}) \qquad (3.33)$$

$$N_{k}(\mathbf{r}) = \partial_{\zeta}^{k} \left(f_{i\zeta}^{+}(\mathbf{r}) - f_{i\zeta}^{-}(\mathbf{r}) \right) \quad \forall k = 2, 3, \cdots$$

Using these definitions, the conditions that the local approximation functions f^{\pm}

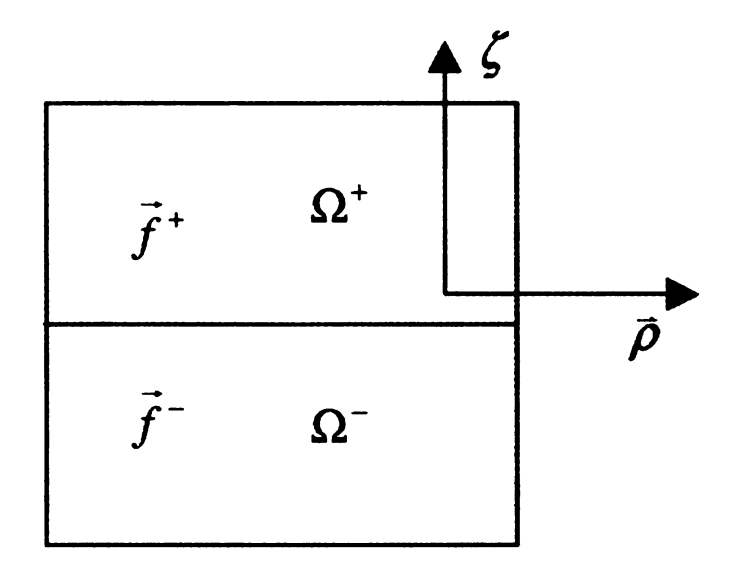


Figure 3.11. Interface of two media

(and the fields) must satisfy are

$$\mathbf{T}_0(\mathbf{r})|_{\forall \mathbf{r} \in \Gamma_i^{\pm}} = 0 \tag{3.34a}$$

$$\mathbf{T}_{k}(\mathbf{r})|_{\forall \mathbf{r} \in \Gamma_{i}^{\pm}} \neq 0 \quad k = 1, 2, \cdots, p-1$$
 (3.34b)

$$N_0(\mathbf{r})|_{\forall \mathbf{r} \in \Gamma_i^{\pm}} \neq 0$$
 (3.34c)

$$N_k(\mathbf{r})|_{\forall \mathbf{r} \in \Gamma_i^{\pm}} \neq 0 \quad k = 2, 3, \dots, p-1$$
 (3.34d)

$$\nabla \cdot \mathbf{f}_i^{\pm}(\mathbf{r}) = 0 \tag{3.34e}$$

Note, the partition of unity ψ_i is continuous across the interface of two media. Therefore if the local approximation functions satisfy the boundary requirements exactly, then the basis functions will also satisfy those requirements exactly.

Next, the additional local approximation function may now be defined in a man-

ner similar to that used earlier.

$$\mathbf{f}_{i}^{+}(\mathbf{r}) = \nabla \times (v_{i,m}^{h,p}(\boldsymbol{\rho},\zeta)\hat{\zeta}) + \nabla \times \nabla \times (v_{i,n}^{h,p}(\boldsymbol{\rho},\zeta)\hat{\zeta})$$

$$= \nabla_{\boldsymbol{\rho}} \times (v_{i,m}^{h,p}(\boldsymbol{\rho},\zeta)\hat{\zeta}) + \nabla_{\boldsymbol{\rho}} \times \nabla_{\boldsymbol{\rho}} \times (v_{i,n}^{h,p}(\boldsymbol{\rho},\zeta)\hat{\zeta}) \qquad \mathbf{r} \in \Omega_{i}^{+}$$

$$+ \hat{\zeta} \times \nabla_{\boldsymbol{\rho}} \times (\hat{\zeta}\partial_{\zeta}v_{i,n}^{h,p}(\boldsymbol{\rho},\zeta))$$

$$\mathbf{f}_{i}^{-}(\mathbf{r}) = \nabla_{\boldsymbol{\rho}} \times (v_{i,m}^{h,p}(\boldsymbol{\rho},\zeta_{0})\hat{\zeta}) + \nabla_{\boldsymbol{\rho}} \times \nabla_{\boldsymbol{\rho}} \times [\hat{\zeta}(\zeta-\zeta_{0})\partial_{\zeta}v_{i,n}^{h,p}(\boldsymbol{\rho},\zeta_{0})]$$

$$+ \hat{\zeta} \times \nabla_{\boldsymbol{\rho}} \times (\hat{\zeta}\partial_{\zeta}v_{i,n}^{h,p}(\boldsymbol{\rho},\zeta_{0})) \qquad \mathbf{r} \in \Omega_{i}^{-}$$

$$(3.35)$$

It can be verified from the above definition of local approximation functions that the functions $\nabla_{\rho} \times \nabla_{\rho} \times (v_{i,n}^{h,p}(\rho,\zeta)\hat{\zeta})$ and $\nabla_{\rho} \times \nabla_{\rho} \times \left[\hat{\zeta}(\zeta-\zeta_{0})\partial_{\zeta}v_{i,n}^{h,p}(\rho,\zeta_{0})\right]$ are normal to the interface, and functions $\nabla_{\rho} \times \left(v_{i,m}^{h,p}(\rho,\zeta)\hat{\zeta}\right)$, $\nabla_{\rho} \times \left(v_{i,m}^{h,p}(\rho,\zeta_{0})\hat{\zeta}\right)$, $\hat{\zeta} \times \nabla_{\rho} \times \left(\hat{\zeta}\partial_{\zeta}v_{i,n}^{h,p}(\rho,\zeta)\right)$ and $\hat{\zeta} \times \nabla_{\rho} \times \left(\hat{\zeta}\partial_{\zeta}v_{i,n}^{h,p}(\rho,\zeta_{0})\right)$ are tangential to the interface. It also follows that to obtain a p^{th} order approximation, the functions $v_{i,m}^{h,p}$ and $v_{i,n}^{h,p}$ should be of order p+1 and p+2, respectively. Next, we use these definitions of $\mathbf{f}_{i}^{\pm}(\mathbf{r})$ to verify that they satisfy the conditions (3.34). Substituting these functions into (3.33) and evaluating these $\forall \mathbf{r} \in \Gamma_{i}^{\pm}$, one obtains

$$\mathbf{T}_{k}(\boldsymbol{\rho},\zeta_{0}) = \left[\partial_{\zeta}^{k} \mathbf{f}_{i\rho}^{+}(\mathbf{r}) - \partial_{\zeta}^{k} \mathbf{f}_{i\rho}^{-}(\mathbf{r}) \right] \Big|_{\zeta=\zeta_{0}} \\
= \nabla_{\rho} \times \left(\hat{\zeta} \partial_{\zeta}^{k} v_{i,m}^{h,p}(\boldsymbol{\rho},\zeta_{0}) \right) + \hat{\zeta} \times \nabla_{\rho} \times \left(\hat{\zeta} \partial_{\zeta}^{k+1} v_{i,n}^{h,p}(\boldsymbol{\rho},\zeta_{0}) \right) \\
N_{0}(\boldsymbol{\rho},\zeta_{0}) = \left[f_{i\zeta}^{+}(\mathbf{r}) - f_{i\zeta}^{-}(\mathbf{r}) \right] \Big|_{\zeta=\zeta_{0}} \\
= \nabla_{\rho} \times \nabla_{\rho} \times \left(v_{i,n}^{h,p}(\boldsymbol{\rho},\zeta_{0}) \hat{\zeta} \right) \cdot \hat{\zeta} \\
N_{k}(\boldsymbol{\rho},\zeta_{0}) = \left[\partial_{\zeta}^{k} f_{i\zeta}^{+} - \partial_{\zeta}^{k} f_{i\zeta}^{-} \right] \Big|_{\zeta=\zeta_{0}} \\
= \begin{cases}
\nabla_{\rho} \times \nabla_{\rho} \times \left(\hat{\zeta} \partial_{\zeta}^{k} v_{i,n}^{h,p}(\boldsymbol{\rho},\zeta_{0}) \right) & k > 1 \\
0 & k = 1
\end{cases} \tag{3.36}$$

It is apparent from the above equation that the functions $\mathbf{T}_k(\mathbf{r})$, $N_0(\mathbf{r})$ and $N_k(\mathbf{r})$ are all not equal to zero. Thus, the additional local approximation functions defined

in (3.35) has discontinuities in (i) its normal component and (ii) normal derivatives of its normal and tangential components. Also,

$$\nabla \cdot \mathbf{f}_{i}^{+} = \nabla \cdot \nabla \times \left(v_{i,m}^{h,p}(\boldsymbol{\rho}, \zeta) \hat{\zeta} \right) + \nabla \cdot \nabla \times \nabla \times \left(v_{i,n}^{h,p}(\boldsymbol{\rho}, \zeta) \hat{\zeta} \right)$$

$$= 0 \tag{3.37a}$$

and

$$\nabla \cdot \mathbf{f}_{i}^{-} = \nabla \cdot \nabla_{\rho} \times \left(v_{i,m}^{h,p}(\boldsymbol{\rho}, \zeta_{0}) \hat{\zeta} \right) + \nabla \cdot \nabla_{\rho} \times \nabla_{\rho} \times \left[\hat{\zeta}(\zeta - \zeta_{0}) \partial_{\zeta} v_{i,n}^{h,p}(\boldsymbol{\rho}, \zeta_{0}) \right]$$

$$+ \nabla \cdot \left\{ \hat{\zeta} \times \nabla_{\rho} \times \left(\hat{\zeta} \partial_{\zeta} v_{i,n}^{h,p}(\boldsymbol{\rho}, \zeta_{0}) \right) \right\}$$

$$= 0 + \nabla_{\rho} \times \nabla_{\rho} \times \left(\hat{\zeta} \partial_{\zeta} v_{i,n}^{h,p}(\boldsymbol{\rho}, \zeta_{0}) \right) - \hat{\zeta} \cdot \left(\nabla_{\rho} \times \nabla_{\rho} \times \left(\hat{\zeta} \partial_{\zeta} v_{i,n}^{h,p}(\boldsymbol{\rho}, \zeta_{0}) \right) \right]$$

$$= 0$$

$$(3.37b)$$

Thus, these basis functions, together with the basis functions \mathbf{u}_{ap}^1 presented in Subsection 3.2.2, satisfy all the criteria laid out in (3.34). This is pictorially depicted in Figure 3.12. Here vector plots of \mathbf{f}^{\pm} are displayed for a patch that straddles the material interface for different orders. From these figures, it is apparent that the tangential components of the span of approximation functions are continuous across the interface whereas the normal components of the span of approximation functions are discontinuous. In some figures, the approximation function in Ω^- is zero, but that does not effect the discontinuity created at the interface. Consequently, the basis function space $\mathbf{V}^1(\Omega)$ is augmented by the functions $\psi_i(\mathbf{r})\mathbf{f}_i^{\pm}$ and denoted by $\widetilde{\mathbf{V}}^1(\Omega)$. It can be easily verified that the function space $\widetilde{\mathbf{V}}^1(\Omega) \subset H(\nabla \times, \Omega)$. The method presented here, defining additional functions, is one way that can be used to impose appropriate conditions on the fields. It is also conceivable to define these jumps via other means. For instance, representing discontinuities using surface integrals along the boundary or appropriately defining the vector potential \mathbf{L} .

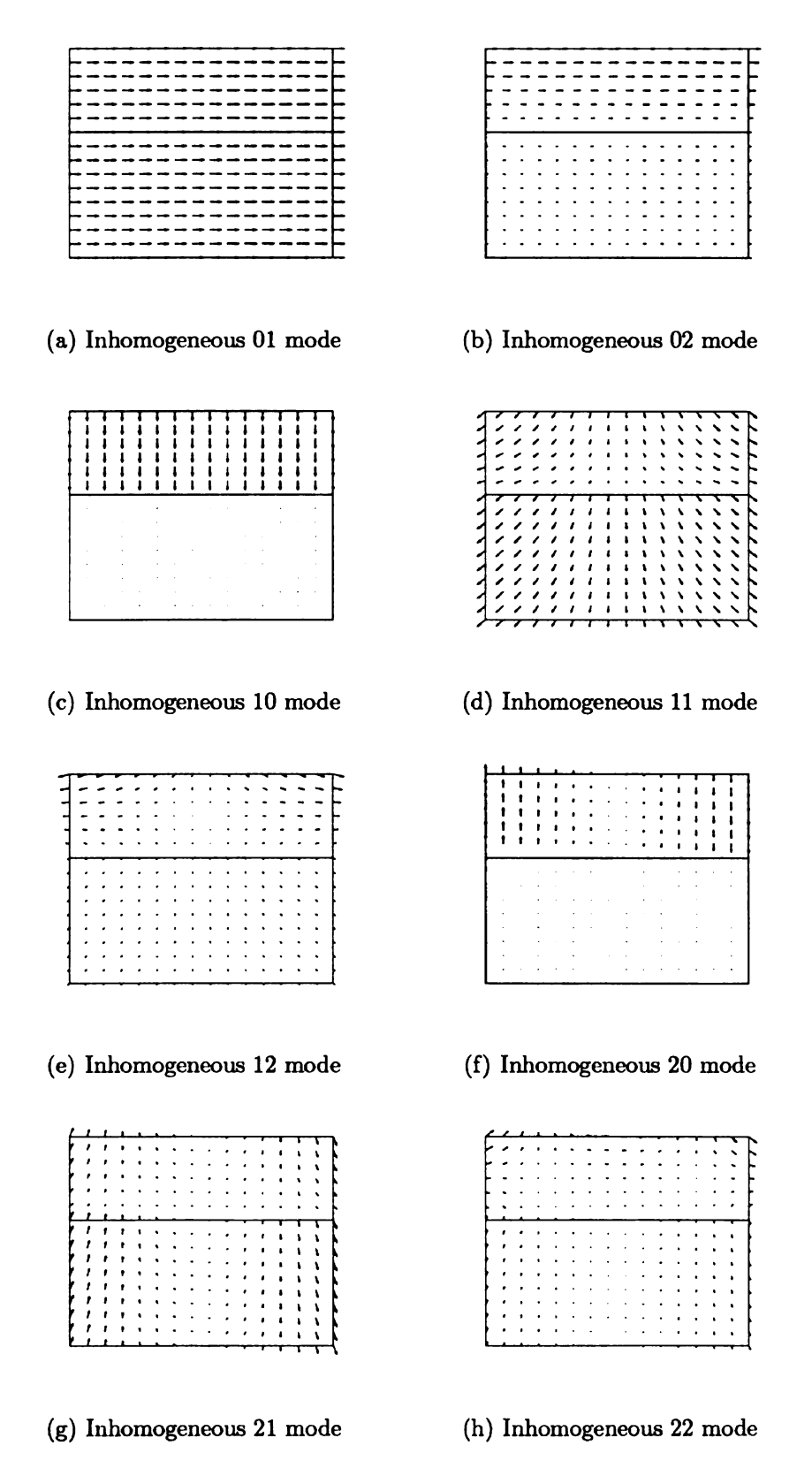


Figure 3.12. Vector plots of inhomogeneous local approximation function \mathbf{v}_i

3.3.2 Proof of the completeness of the vector basis function

In what follows, we present an alternative proof that the proposed basis functions are complete. Assume that the field in domain Ω^+ and domain Ω^- , shown in Figure 3.11, are $\mathbf{u}^+(\mathbf{r})$ and $\mathbf{u}^-(\mathbf{r})$, respectively. Two fields are independent of each other except for the continuity of the tangential components of $\mathbf{u}(\mathbf{r})$ and $\nabla \times \mathbf{u}(\mathbf{r})$ at the interface. To prove completeness, we redefine the fields in the domain $\Omega = \Omega^+ \cup \Omega^-$. To this end, let $\mathbf{u}_t(\mathbf{r})$ denote the field for $\mathbf{r} \in \Omega$, and $\mathbf{u}_r(\mathbf{r}) = \mathbf{u}^+(\mathbf{r}) - \mathbf{u}_t(\mathbf{r})$ for $\mathbf{r} \in \Omega^+$. The fields in Ω^+ and Ω^- can be rewritten as

$$\mathbf{u}(\mathbf{r}) = \begin{cases} \mathbf{u}^{+}(\mathbf{r}) = \mathbf{u}_{t}(\mathbf{r}) + \mathbf{u}_{r}(\mathbf{r}) & \mathbf{r} \in \Omega^{+} \\ \mathbf{u}^{-}(\mathbf{r}) = \mathbf{u}_{t}(\mathbf{r}) & \mathbf{r} \in \Omega^{-} \end{cases}$$
(3.38)

where fields $\mathbf{u}_t(\mathbf{r})$ and $\mathbf{u}_r(\mathbf{r})$ are assumed to be smooth as are their derivatives. They are independent of each other, and $\mathbf{u}_r(\mathbf{r})$ and $\nabla \times \mathbf{u}_r(\mathbf{r})$ have zero tangential components at the interface. Because $\mathbf{u}(\mathbf{r})$ is divergence free, we can express it as:

$$\mathbf{u}_{t}(\mathbf{r}) = \nabla \times (F_{t}\hat{\zeta}) + \nabla \times \nabla \times (A_{t}\hat{\zeta})$$

$$\mathbf{u}_{r}(\mathbf{r}) = \nabla \times (F_{r}\hat{\zeta}) + \nabla \times \nabla \times (A_{r}\hat{\zeta})$$
(3.39)

where F_t , F_r , A_t and A_r are independent quantities with constraints $F_r(\zeta_0) = 0$ and $\partial_{\zeta} A_r(\zeta_0) = 0$. The constraints are from the fact that the tangential components of $\mathbf{u}_r(\mathbf{r})$ and $\nabla \times \mathbf{u}_r(\mathbf{r})$ are zero at the interface. Imposing a requirements, that any approximation to this function be p^{th} order, the basis functions (or local approximation functions) should be able to approximate F_t and F_r to p+1 order and approximate A_t and A_r to p+2 order.

Next, we will demonstrate that this requirement can be satisfied by the basis functions defined in this paper. Let $\mathbf{f}_0(\mathbf{r})$, $\mathbf{f}^{\pm}(\mathbf{r})$ be the local approximation functions that represent the field locally. In the patch across the interface, we approximate the fields by approximation function in homogeneous domain and additional

approximation function that creates the discontinuity satisfying constraints at the interface. Then, the functions for homogeneous domain and inhomogeneous domain is denoted by \mathbf{f}_0 in whole domain and \mathbf{f}^{\pm} in Ω^{\pm} , respectively. More specifically:

$$\mathbf{f}_{0}(\mathbf{r}) = \nabla \times (v_{m,0}(\mathbf{r})\hat{\zeta}) + \nabla \times \nabla \times (v_{n,0}(\mathbf{r})\hat{\zeta})$$

$$\mathbf{f}^{+}(\mathbf{r}) = \nabla \times (v_{m,a}(\mathbf{r})\hat{\zeta}) + \nabla \times \nabla \times (v_{n,a}(\mathbf{r})\hat{\zeta})$$

$$\mathbf{f}^{-}(\mathbf{r}) = \nabla_{\rho} \times (v_{m,a}(\rho,\zeta_{0})\hat{\zeta}) + \nabla_{\rho} \times \nabla_{\rho} \times \left[(\zeta - \zeta_{0})\partial_{\zeta}v_{n,a}(\rho,\zeta_{0})\hat{\zeta} \right]$$

$$+ \hat{\zeta} \times \nabla_{\rho} \times \left[\partial_{\zeta}v_{n,a}(\rho,\zeta_{0})\hat{\zeta} \right]$$

$$= \nabla \times (v_{m,a}(\rho,\zeta_{0})\hat{\zeta}) + \nabla \times \nabla \times \left[(\zeta - \zeta_{0})\partial_{\zeta}v_{n,a}(\rho,\zeta_{0})\hat{\zeta} \right]$$

$$(3.40)$$

where we omit the superscript h and p and subscript i and add subscript 0 and a for homogeneous basis and additional basis for brevity. Obviously $v_{m,0}$, $v_{m,a}$ are p+1 order and $v_{n,0}$, $v_{n,a}$ are p+2 order. Let $F_{r,app}$, $F_{t,app}$, $A_{r,app}$ and $A_{t,app}$ be local approximation to F_r , F_t , A_r and A_t . Compared with (3.38), the local approximation can be written as:

$$F_{t,app} = v_{m,0}(\mathbf{r}) + v_{m,a}(\boldsymbol{\rho}, \zeta_0)$$

$$F_{r,app} = v_{m,a}(\mathbf{r}) - v_{m,a}(\boldsymbol{\rho}, \zeta_0)$$

$$A_{t,app} = v_{n,0}(\mathbf{r}) + (\zeta - \zeta_0)\partial_{\zeta}v_{n,a}(\boldsymbol{\rho}, \zeta_0)$$

$$A_{r,app} = v_{n,a}(\mathbf{r}) - (\zeta - \zeta_0)\partial_{\zeta}v_{n,a}(\boldsymbol{\rho}, \zeta_0)$$
(3.41)

Obviously, $F_{t,app}$ and $F_{r,app}$ can approximate F_t and F_r to p+1 order, and $A_{t,app}$ and $A_{r,app}$ can approximate A_t and A_r to p+2 order. Constraints $F_r(\zeta_0) = 0$ and $\partial_{\zeta} A_r(\zeta_0) = 0$ can also be satisfied. Therefore the basis functions are complete to order p.

3.3.3 Numerical experiments

In the next series of examples, we consider problems wherein the medium is piecewise homogeneous. We will examine both boundary value and eigenvalue problems. First, consider a 2D inhomogeneous domain. The computational domain is defined by $\Omega = \Omega^+ + \Omega^-$ with $\Omega^+ = (0,1) \times (0.5,1)$ and $\Omega^- = (0,1) \times (0,0.5)$. The relative permittivity in Ω^+ and Ω^- are chosen to be $\varepsilon_r = 1, 3$, respectively. The fields are as follows: $\forall \mathbf{r} \in \Omega^+$ the electric field is $\mathbf{E} = (-\hat{x} - \sqrt{3}\hat{y})exp\{-j[\sqrt{3}x - (y - 1/2)]\}$, and $\forall \mathbf{r} \in \Omega^-$ the electric field is $\mathbf{E} = 1/\sqrt{3}(-\sqrt{3}\hat{x} - \hat{y})exp\{-j[\sqrt{3}x - 3(y - 1/2)]\}$. Using this data, we derive the appropriate Dirichlet and Neumann boundary conditions that are to be imposed.

The basis functions used belong to $\tilde{\mathbf{V}}(\Omega)$. These basis functions create a discontinuity in the normal component and the normal derivatives of the tangential component. A tensor product of Legendre polynomials is used as a generating function, the L^2 norm of relative error is evaluated at uniformly distributed 100×100 sample points. This is depicted in Figure 3.13, and as is readily apparent, the method shows h, p-convergence when either the Dirichlet or Neumann boundary condition is used.

Next, we examine the performance of these basis function when applied to a 3D problem. The computational domain is defined by $\Omega = \Omega^+ + \Omega^-$ with $\Omega^+ = (0,1) \times (0,1) \times (0.5,1)$ and $\Omega^- = (0,1) \times (0,1) \times (0,0.5)$. The relative permittivity in Ω^+ and Ω^- are chosen to be $\varepsilon_\tau = 1,3$, respectively. The fields imposed are as follows: $\forall \mathbf{r} \in \Omega^+$ the electric field is $\mathbf{E} = \hat{y}exp\{-j[\sqrt{3}x-(z-0.5)]\}-\hat{y}0.5exp\{-j[\sqrt{3}x+(z-0.5)]\}$, and $\forall \mathbf{r} \in \Omega^-$ the electric field is $\mathbf{E} = \hat{y}0.5exp\{-j\sqrt{3}[x-\sqrt{3}(z-0.5)]\}$. This data is used to impose the Dirichlet boundary conditions. Figure 3.14 demonstrates the h and p convergence. These results are obtained by sampling the fields at $5 \times 5 \times 5$ points in domain and computing the L^2 error norm. As is apparent, the results are excellent.

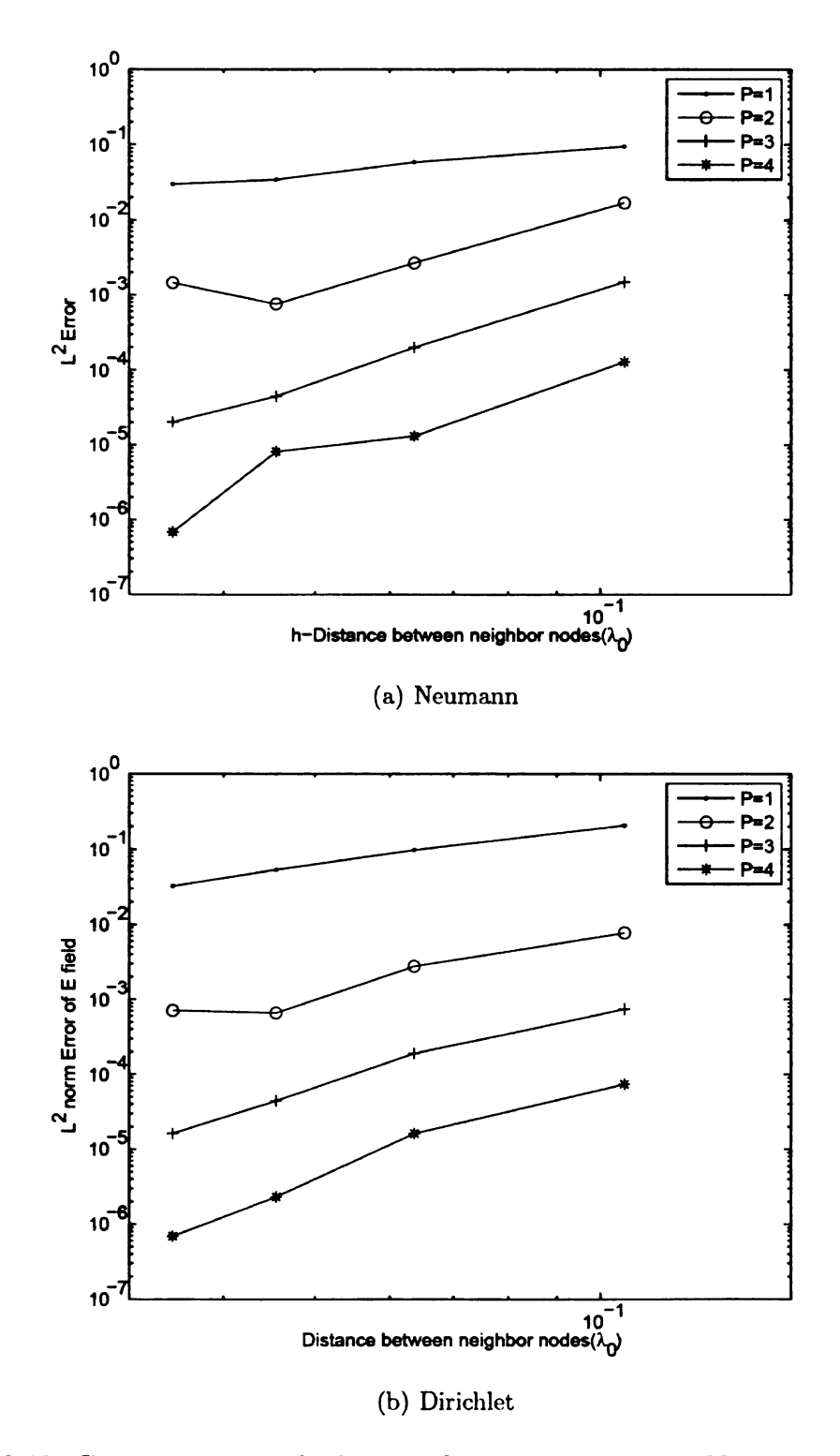


Figure 3.13. Convergence graphs for 2D inhomogeneous vector Neumann and Dirichlet $\ensuremath{\mathsf{BVPs}}$

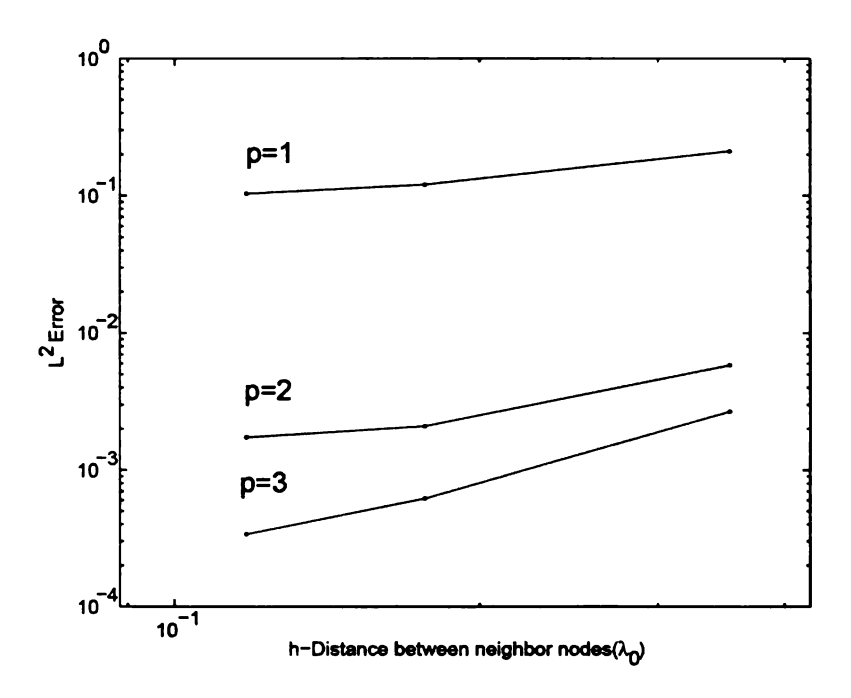


Figure 3.14. Convergence graphs for 3D inhomogeneous vector Dirichlet BVPs

Next, we compute the eigenmodes in a brick cavity. The computational domain is defined by $\Omega = \Omega^+ + \Omega^-$ with $\Omega^+(0,1) \times (0,0.1) \times (0.5,1)$ and $\Omega^- = (0,1) \times (0,0.1) \times (0,0.5)$. The relative permittivity in Ω^+ and Ω^- are chosen to be $\varepsilon_r = 1,2$. This numerical experiment is identical to the one designed in [64] to validate the classical vector FEM code. The convergence data (error in L^2 norm) for eigenmodes are presented in Table 3.3. As is evident from this data, the results obtained converge rapidly with increasing order and refinement.

3.4 GFEM solver for piecewise homogeneous domain with curved interface

3.4.1 Basis function

Until now, the vector GFEM solver has been developed for homogeneous domain and piecewise homogeneous domain with flat material interface. When solving large

		p=2	p=3
Principal	h = 1/2	6.2e-4	1.8e-5
Mode	h = 1/4 2.0e-4	9.1e-6	
Mode	h = 1/6	5.6e-5	6.1e-6
First 6	h = 1/2	0.019	1.7e-3
modes	h = 1/4	4.9e-3	7.3e-4
inodes	$h = 1/6 \mid 1.8e-3$	1.8e-3	3.7e-4

Table 3.3. Error in eigenvalues computed using \mathbf{u}_{ap}^1

problem such as antenna design, air plane design and so on, the curved material interface should be analyzed. When high order accuracy of solution is required, high order accuracy in both basis functions and geometry description are necessary. In classic FEM, there are two ways to obtain satisfactory geometry description. First, we can descritize the regular mesh fine enough to describe the geometry, but it limit the geometry description to first order accuracy. Second, we can utilize the high order mesh based on the geometry transform which realize the high order accuracy of the geometry description, but the property of vector basis function, especially the divergence free property, is spoiled. Those drawbacks come from the continuity requirments of basis function space on the edge of the mesh in classic FEM. In GFEM, as the continuity requirement of the basis function can be realized only by the partition of unity function, we have more freedom in constructing the local approximation function on the material interface. More specifically, the construction of the basis function needn't depend on the geometric transformation. This property makes it possible to obtain high order accuracy of geometry transform and divergence-free vector basis function together. In this section, we will propose a GFEM solver to deal with the curved material interface and demonstrate the convergence of those basis functions.

Figure 3.15 show a patch Ω_i on the curved interface. The constitutive parameters are different on two side. The tangential direction and normal direction to the

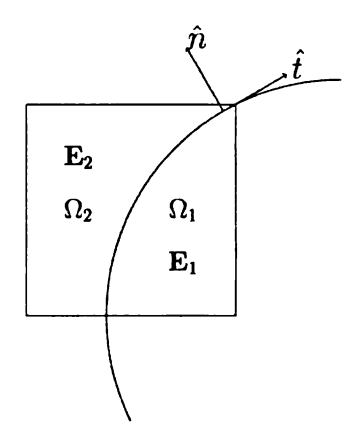


Figure 3.15. Figure of patch on the curved structure

interface are denoted by \hat{t} and \hat{n} on the interface. If the fields in both homogeneous domain is denoted by \mathbf{E}_1 and \mathbf{E}_2 , then on the interface, those fields should satisfy the following criteria:

$$\mathbf{E}_{t1} = \mathbf{E}_{t2}$$

$$E_{n1} \neq E_{n2}$$

$$\partial_n \mathbf{E}_{t1} \neq \partial_n \mathbf{E}_{t2}$$

$$\partial_n E_{n1} \neq \partial_n E_{n2}$$

$$\nabla \cdot \mathbf{E} = 0$$
(3.42)

The above criteria show that the tangential component of the field are continuous and the normal component of the field are discontinuous. The normal directives of both tangential and normal components are discontinuous as well. The fields are divergence free in both homogeneous domain. As the vector basis function for homogeneous domain is continuous everywhere, the additional vector local approximation function \mathbf{f}_{add} should be defined in the patch to create the appropriate discontinu-

ities. The additional function \mathbf{f}_{add} is not necessary to be defined on both sides of the interface, we can just define \mathbf{f}_{add} in one side such as Ω_1 in Figure 3.15. Then the criteria for the \mathbf{f}_{add} are the following:

$$\mathbf{f}_{t} = 0$$

$$f_{n} \neq 0$$

$$\partial_{n} \mathbf{f}_{t} \neq 0$$

$$\partial_{n} f_{n} \neq 0$$

$$\nabla \cdot \mathbf{f} = 0$$
(3.43)

That means, continuous component of the fields result in the zero component of \mathbf{f}_{add} on the interface, discontinuous component of the fields result in the nonzero component of \mathbf{f}_{add} . The addition function \mathbf{f}_{add} is also divergence free. The last criteria is very important to get the high order approximation of the divergence free field.

The most straightforward way is to construct the addition functions based on geometry transform. By doing so, the curvilinear structure Ω_1 is transformed to a regular structure. After defining the additional basis function in that structure. we transform it back to the original structure. Unfortunately, we found that when the additional function satisfies all the continuity requirements on the interface, it's not divergence free. In GFEM, as mentioned before, the continuity requirements of the basis function on the edge of the patch can be realized only by the partition of unity function. That means the construction of the addition function \mathbf{f}_{add} can only depend on material interface. Next, the construction of the addition function will be introduced in detail.

We defined the local transverse and longitudinal coordinate as $\hat{\rho}$ and \hat{z} , then the material interface can be defined as $z_0 = P(\rho) \quad \forall \rho \in \Gamma_{\rho}$. Γ_{ρ} denotes the projection of the interface in patch Ω_i on the ρ plane, and we can define the \mathbf{f}_{add} at any place in

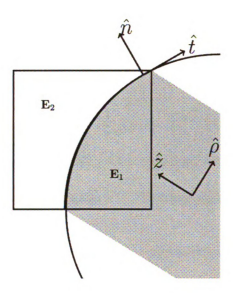


Figure 3.16. Local coordinate of patch on the curved structure

the domain $\Gamma_{\rho} \times (-\inf, P(\rho))$ as shown in Figure 3.16. The \mathbf{f}_{add} can be formulated using

$$\mathbf{v} = \nabla \times (\phi_m \hat{z}) + \nabla \times \nabla \times (\phi_n \hat{z})$$

$$\mathbf{f}(\boldsymbol{\rho}, z) = \mathbf{v}(\boldsymbol{\rho}, z) - [\mathbf{v}(\boldsymbol{\rho}, P(\boldsymbol{\rho})) - \hat{n}(\mathbf{v}(\boldsymbol{\rho}, P(\boldsymbol{\rho})) \cdot \hat{n})]$$

$$+ \hat{z} \nabla_{\boldsymbol{\rho}} \cdot [\mathbf{v}(\boldsymbol{\rho}, P(\boldsymbol{\rho})) - \hat{n}(\mathbf{v}(\boldsymbol{\rho}, P(\boldsymbol{\rho})) \cdot \hat{n})](z - P(\boldsymbol{\rho}))$$
(3.44)

where the \hat{n} represents the unit vector normal to the interface. This vector can be expressed mathematically by $\hat{n} = \hat{z} - \nabla_{\rho} P(\rho)$. Scalar function ϕ_m and ϕ_n can be any function. For p^{th} order accuracy, function ϕ_m and ϕ_n should be of order p+1 and p+2. The basis function defined above can satisfy all the criteria, including the divergence-free criteria. Figure 3.17 shows 2D examples of the addition function. In these figures, tangential component of the addition function is zero on the interface, and the normal component is nonzero.

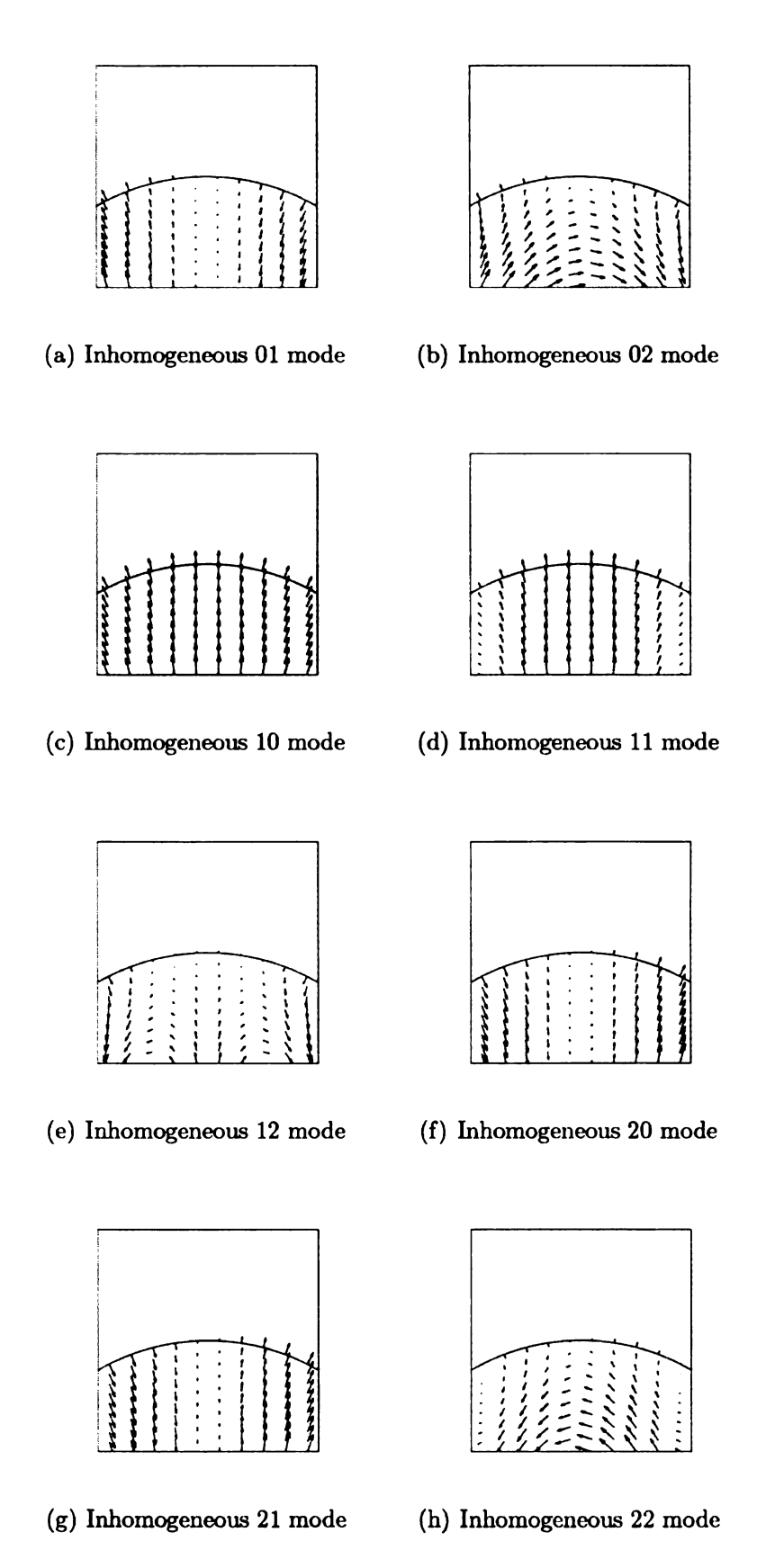


Figure 3.17. Vector plots of inhomogeneous local approximation function \mathbf{v}_i for curved interface

The zero tangential component and nonzero normal component of the \mathbf{f}_{add} is proved mathematically as follows:

$$\mathbf{f}_{t}(\boldsymbol{\rho}, P(\boldsymbol{\rho})) = \mathbf{v}_{t}(\boldsymbol{\rho}, P(\boldsymbol{\rho})) - [\mathbf{v}_{t}(\boldsymbol{\rho}, P(\boldsymbol{\rho})) - 0]$$

$$+ [\hat{z} - (\hat{z} \cdot \hat{n})\hat{n}] \nabla_{\boldsymbol{\rho}} \cdot [\mathbf{v}(\boldsymbol{\rho}, P(\boldsymbol{\rho})) - \hat{n}(\mathbf{v}(\boldsymbol{\rho}, P(\boldsymbol{\rho})) \cdot \hat{n})] (P(\boldsymbol{\rho}) - P(\boldsymbol{\rho}))$$

$$= 0$$

$$\mathbf{f}_{n}(\boldsymbol{\rho}, P(\boldsymbol{\rho})) = \mathbf{v}_{n}(\boldsymbol{\rho}, P(\boldsymbol{\rho})) - [\mathbf{v}_{n}(\boldsymbol{\rho}, P(\boldsymbol{\rho})) - \hat{n}(\mathbf{v}(\boldsymbol{\rho}, P(\boldsymbol{\rho})) \cdot \hat{n})]$$

$$+ (\hat{z} \cdot \hat{n})\hat{n} \nabla_{\boldsymbol{\rho}} \cdot [\mathbf{v}(\boldsymbol{\rho}, P(\boldsymbol{\rho})) - \hat{n}(\mathbf{v}(\boldsymbol{\rho}, P(\boldsymbol{\rho})) \cdot \hat{n})] (P(\boldsymbol{\rho}) - P(\boldsymbol{\rho}))$$

$$= \hat{n}(\mathbf{v}(\boldsymbol{\rho}, P(\boldsymbol{\rho})) \cdot \hat{n})$$

$$\neq 0$$

$$(3.45)$$

The following is the proof of divergence free property of \mathbf{f}_{add} .

$$\nabla \cdot \mathbf{f}_{n}(\boldsymbol{\rho}, P(\boldsymbol{\rho})) = \nabla \cdot \mathbf{v}(\boldsymbol{\rho}, z)$$

$$- (\mathbf{v}(\boldsymbol{\rho}, P(\boldsymbol{\rho})) \cdot \hat{n})]$$

$$+ \nabla_{\boldsymbol{\rho}} \cdot [\mathbf{v}(\boldsymbol{\rho}, P(\boldsymbol{\rho})) - \hat{n}(\mathbf{v}(\boldsymbol{\rho}, P(\boldsymbol{\rho})) \cdot \hat{n})]$$

$$= 0$$
(3.46)

The functions introduced herein demonstrate means to develop additional basis function for curved surface. For completeness, we first introduce basis function developed with geometry transformation. A curvilinear structure in xy-domain can be mapped to a regular structure in $\xi\eta$ -plane. Transform functions are

$$x = x(\xi, \eta)$$

$$y = y(\xi, \eta)$$
(3.47)

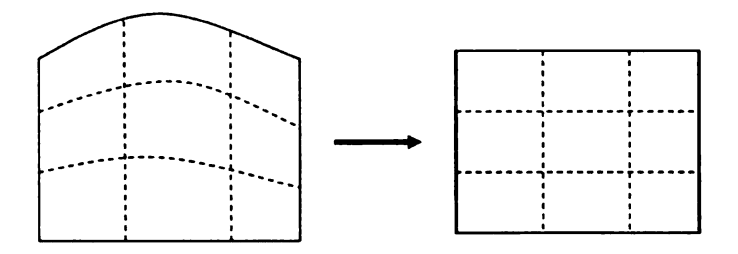


Figure 3.18. Geometric transform

Then Jacobian matrix is defined as:

$$[\mathbf{J}] = \begin{bmatrix} \frac{\partial x}{\partial \xi} & \frac{\partial y}{\partial \xi} \\ \frac{\partial x}{\partial \eta} & \frac{\partial y}{\partial \eta} \end{bmatrix}$$
(3.48)

and $|\mathbf{J}|$ is Jacobian. If we use \mathbf{u} and $\tilde{\mathbf{u}}$ to represent the vector function in curvilinear structure and regular structure, then we can construct the addition function in curvilinear structure by the following transform formula:

$$\mathbf{u} = [\mathbf{J}]^{-1}\tilde{\mathbf{u}}$$

$$\nabla \times \mathbf{u} = \frac{1}{|\mathbf{J}|} [\mathbf{J}]^T \tilde{\nabla} \times \tilde{\mathbf{u}}$$
(3.49)

This formula can be easily extended to three dimension.

In both of the above two methods, the material interface is described by some sample points on the interface. Locations of other point on the interface is computed by interpolation of those sample points with Lagrange polynomials as interpolatory functions.

3.4.2 Numerical Experiments

Next, several numerical results will be shown to demonstrate the accuracy of this vector GFEM solver. First, we shall demonstrate the convergence of the local approximation function. Next we shall demonstrate the convergence of the basis function. Finally, one large two dimension problem will be used to demonstrate the feasibility of this solver. At first, convergence of the local approximation will be demonstrated. Figure 3.19 shows one patch on the curved interface, the curved interface is a segment of the circle with radius 0.48λ and cross the center of the rectangle which can be described as $x^2 + (y+3)^2 = 3^2$ with $\vec{k} = 2\pi \hat{x}$. The rectangular computation domain is $(-0.5, 0.5) \times (-0.5, 0.5)$. The analytical results in the patch is the total fields when a TE plane wave propagating to the dielectric coated PEC cylinder with radius of the PEC 0.24λ . The patch is on the boundary of the dielectric coating with the side of the patch parallel to the line between the center of the patch and the center of the PEC. When we change the size of the patch, we keep the center of the patch on a fixed point on the boundary of dielectric coating. The relative L^2 error is computed on the 100×100 sample points uniformly distributed on the patches. The additional scalar function is chosen as tensor product of Legendre polynomials. The Figure 3.20 show the error based on both of two methods introduced above. The dashed line show the error of local function based on geometry transformation. From the figure we can find that when the order of the function is high, the accuracy of the approximation is spoiled by the geometric transform. This results shows the importance of divergence-free criteria in creating the additional function. The solid line show the additional function based on [3.44]. It shows the h- p- convergence of the additional function. The error is excellent

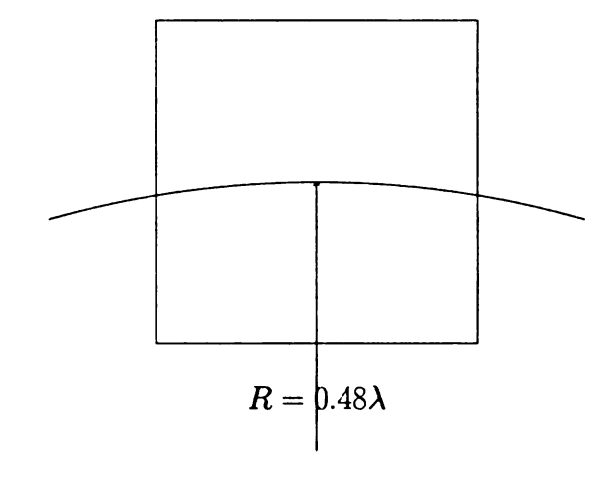


Figure 3.19. Figure of patch on the curved structure

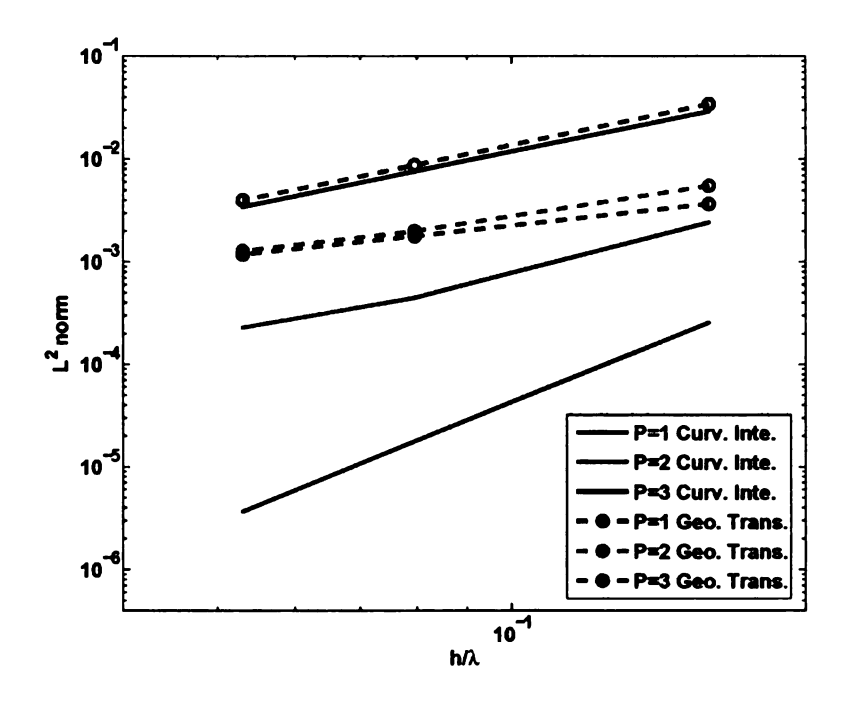


Figure 3.20. h-, p- convergence of the local approximation

Next figure shows different errors when the center of the PEC circle is moving around the patch, e.g., in Figure 3.21 the α is changing from 0 to 2π . In this case, the size of the PEC and dielectric coating are the same with before. The center of the patch is still on one point of the dielectric coating's boundary. In this experiment, the size of the patch is 0.05λ and p=3, The relative L^2 error is computed on the 100×100 sample points uniformly distributed on the patches. The Figure 3.22 show that the error is always smaller than 10^{-5} .

Next, we will demonstrate the convergence of the vector GFEM solver in a simple problem. As shown in Figure 3.23, there is a dielectric coated PEC with the radius of the PEC and dielectric as 0.06λ and 0.13λ . The computation domain is bounded by two circles with radius 0.095λ and 0.16λ . Relative permittivity of dielectric coating is 2. Dielectric boundary condition is imposed. Incident field is a TE plane wave and propagates along $-\hat{x}$ direction. The L^2 error is computed on the 100×100 sample points uniformly distributed in the domain. The Figure 3.24 shows the convergence of the basis function. The fields with $h=0.055\lambda$ and p=4 are also shown in the Figure 3.25, Figure 3.26. Figures show the analytical result and error of E_{ρ} and E_{ϕ} respectively. As the E_{ρ} is normal to the interface, it is discontinuous on the interface, when E_{ϕ} is continuous on the interface. The figure demonstrates that property and shows that the error is small and distributed uniformly throughout the computational domain and is not restricted to the surface.

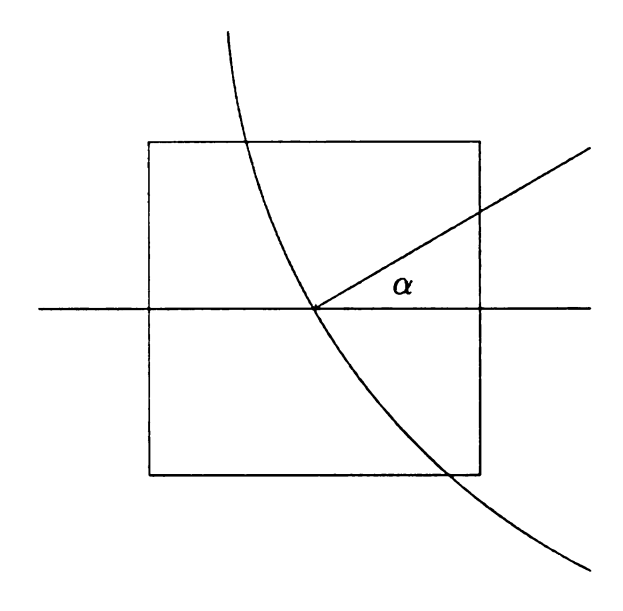


Figure 3.21. Figure of rotated curved structure

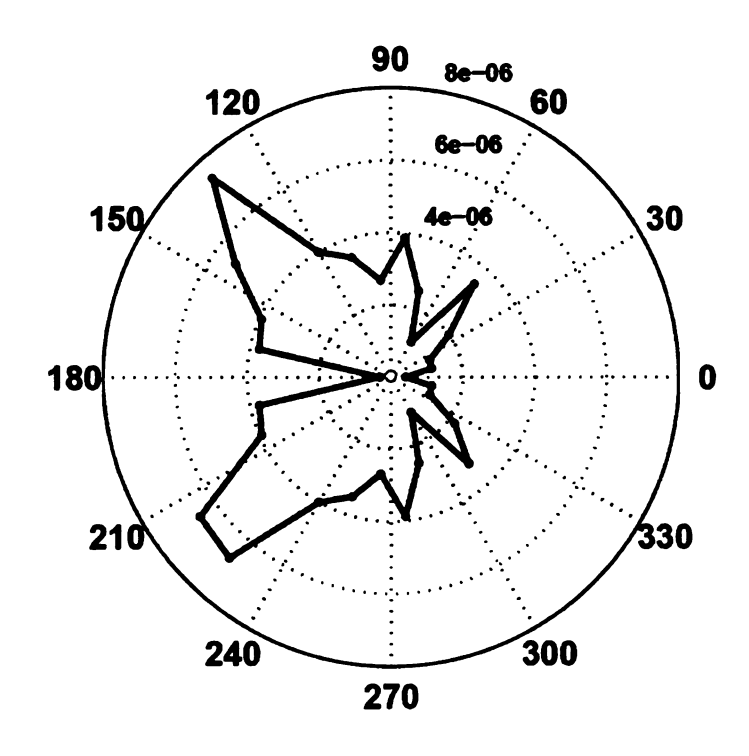


Figure 3.22. Error with different curved surface

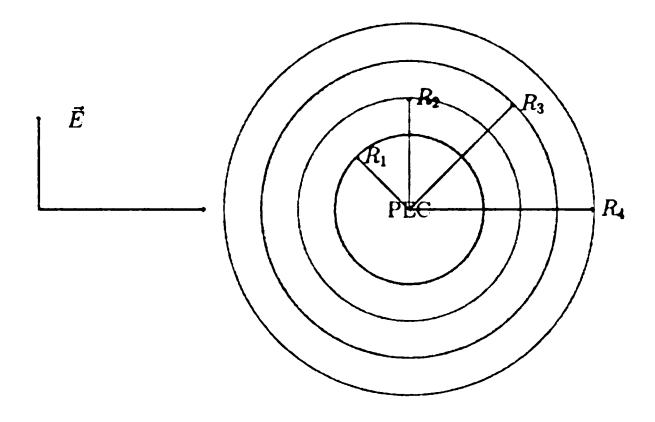


Figure 3.23. Geometric description of dielectric-coated PEC cylinder

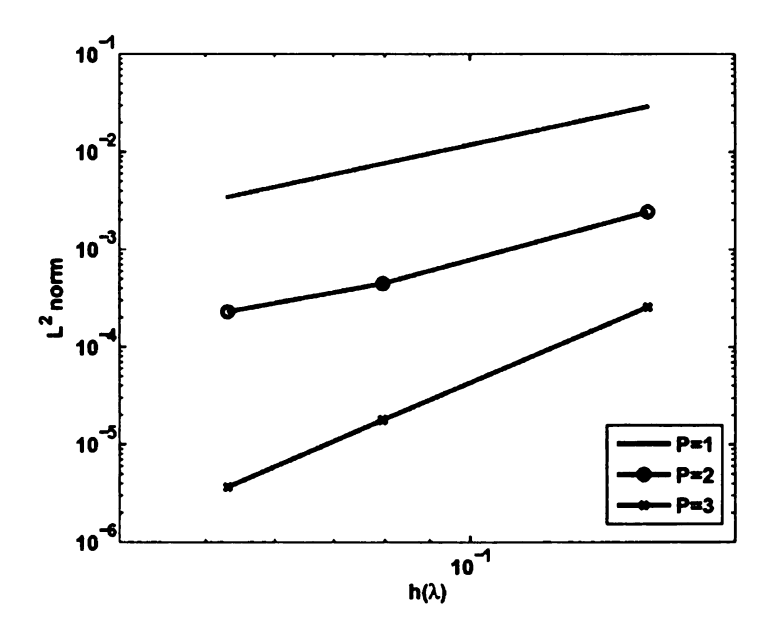
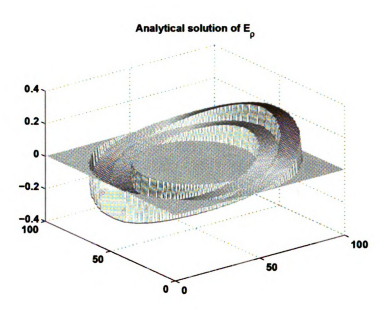


Figure 3.24. Convergence graphs of GFEM solver with Dirichlet BC $\,$



(a) Analytical result for E_{ρ}

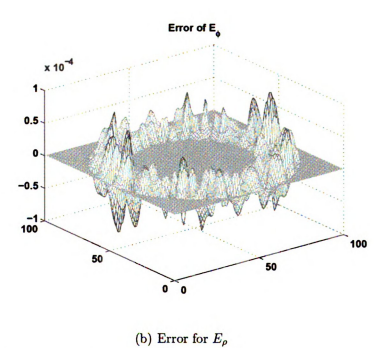
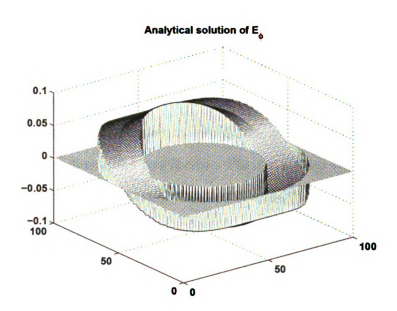
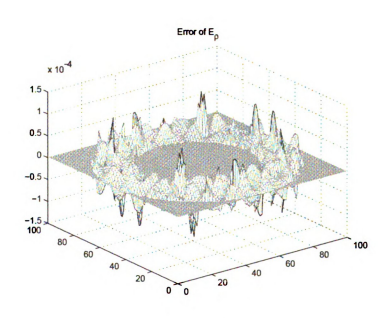


Figure 3.25. Analytical and numerical result of ρ component of the field



(a) Analytical result for E_{ϕ}



(b) Error for E_{ϕ}

Figure 3.26. Analytical and numerical result of ϕ component of the field

Last, a 2D large problem will be analyzed. As shown in Figure 3.27, there is also a dielectric coated PEC with the radius of the PEC and dielectric coating as 2.7λ and 2.85λ . The relative permittivity of dielectric coating is 2. The computation domain is truncated by a circle with radius 3.0λ . The incident field is TE plane wave propagating along $-\hat{x}$ direction. Dirichlet boundary condition is imposed on the boundary. The distance h between the neighboring nodes is 0.43λ , the order p=4, numerical results are computed on two circles inside and out of the interface and close to it with radius 2.82λ and 2.88λ . The results are shown in the Figure 3.28, Figure 3.29. Results show that the approximation is excellent and the relative error is 2×10^{-3} .

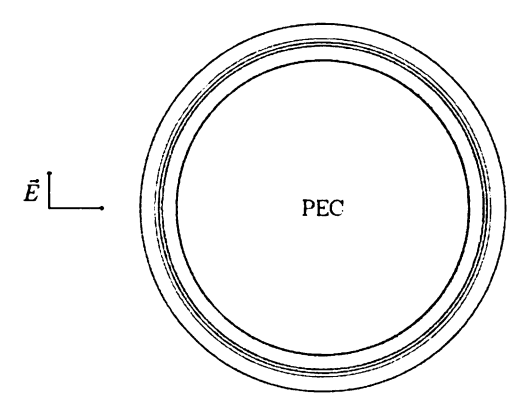
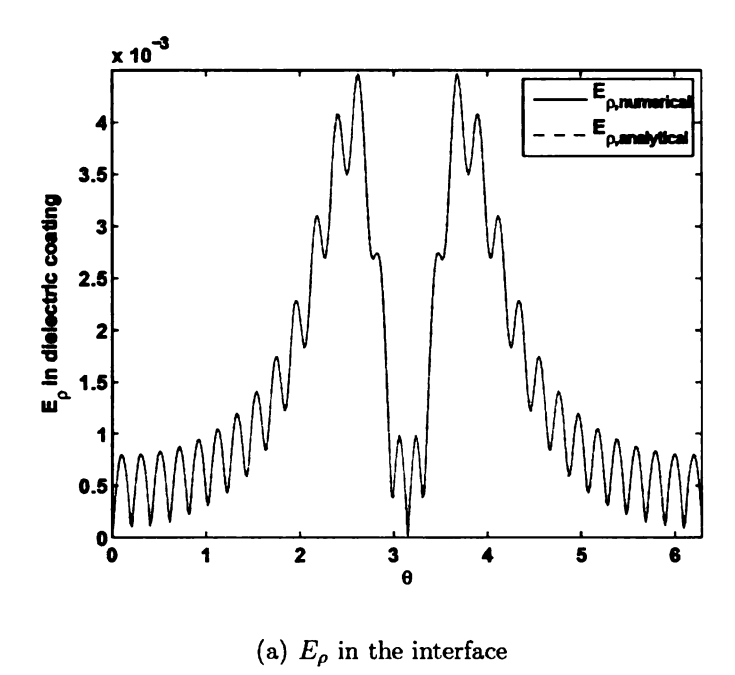


Figure 3.27. Figure of patch on the curved structure



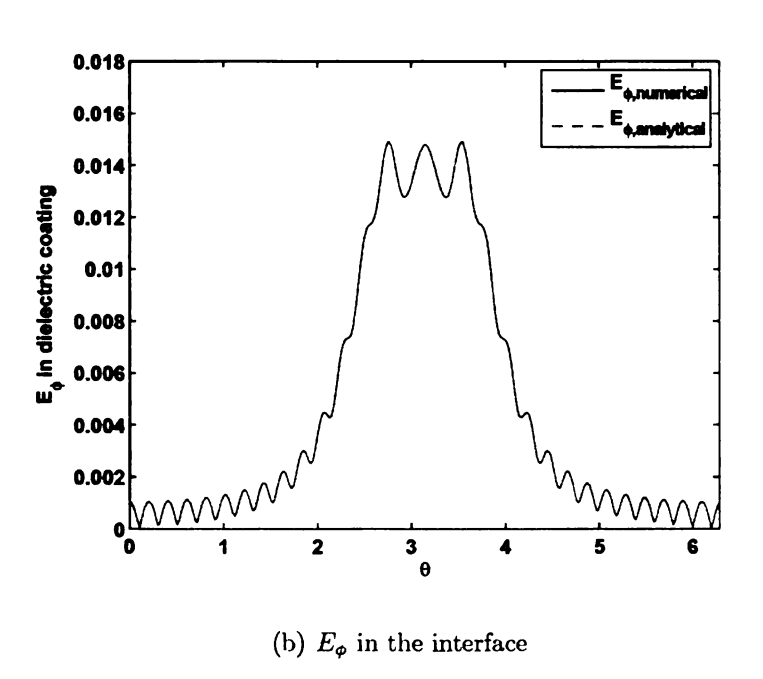
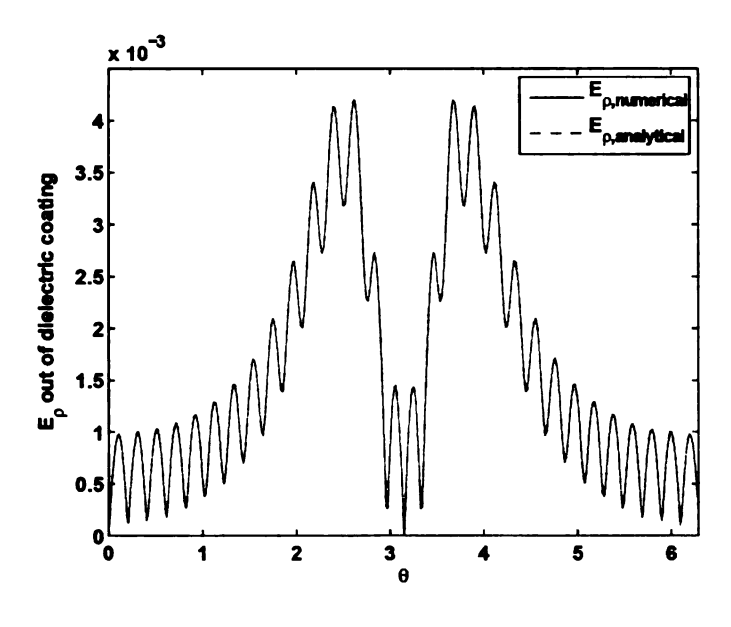


Figure 3.28. Analytical and numerical result of large 2D inhomogeneous problem in the interface ${\bf r}$



(a) E_{ρ} out of the interface

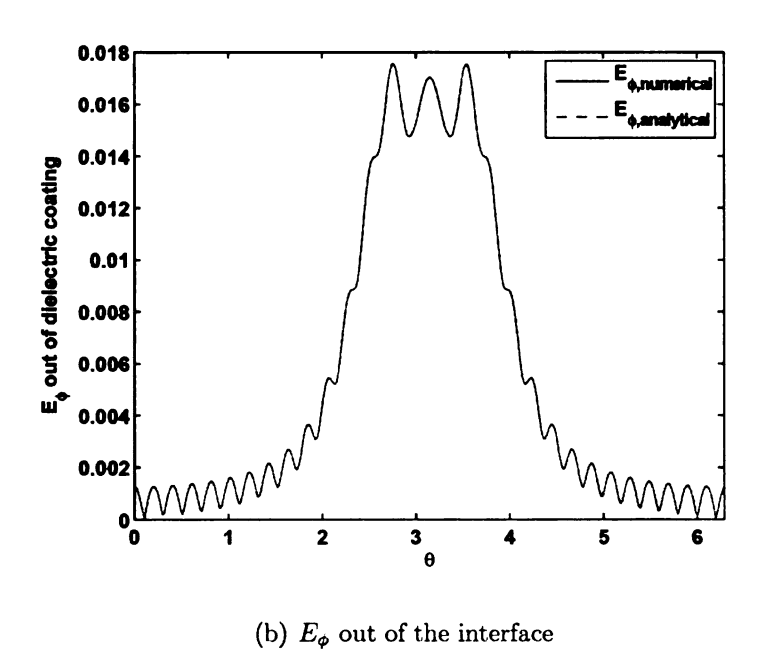


Figure 3.29. Analytical and numerical result of large 2D inhomogeneous problem out of the interface

3.5 Overcoming linear dependence and condition number issues

Another problem that plagues GFEM, as it does any higher order method is the condition number of the resulting system. Indeed, this is more of a problem here as opposed to classical FEM as the space of basis functions is not interpolatory. The vector basis functions in i^{th} patch $\psi_i(\mathbf{r})\nabla \times \left[\hat{c}v_{i,m}^{h,p}\right]$ and $\psi_i(\mathbf{r})\nabla \times \nabla \times \left[\hat{c}v_{i,n}^{h,p}\right]$ are not orthogonal. In fact, they may even be dependent on each other. Consequently, a good starting point to obtain a handle on the condition number is to redefine basis functions in each patch so that they are orthogonal to each other. To this end, we compute a symmetric matrix of inner product of basis functions $\{\mathbf{S}\}_i$ in the i^{th} patch as defined by

$$\{\mathbf{L}\}_{ii} = \int_{\Omega_i} d\Omega \{\mathbf{S}\}_i \{\mathbf{S}\}_i^T \tag{3.50}$$

where $\{S\}_i$ is a vector whose elements are all basis functions that are defined in the i^{th} patch. Representing the singular value decomposition of the above matrix as $\{L\}_{ii} = U_i^T D_i U_i$ where U_i is an orthogonal matrix, and D_i is a diagonal matrix that contains the singular values. We can then redefine the basis functions as $\{\tilde{S}\}_i = U_i \{S\}_i$. It is apparent from this redefinition that the inner product of any two basis in the domain Ω_i are orthogonal. The basis functions related to small singular values in D_i are dropped. These basis functions can be readily used in all the quantities derived earlier and has been found to considerably reduce the condition number of the resulting system. More specifically, consider the bilinear form $A_h(\mathbf{u}, \mathbf{w}) = \mathcal{F}_h(\mathbf{w})$ in (3.29). Using the span of basis functions defined earlier, one can rewrite (3.29) as a matrix equation of the form $\sum_j [A]_{ij} \{\mathbf{x}\}_j = \{\mathbf{f}\}_i$ where a $\{\mathbf{x}\}_j$ is a vector of unknowns coefficients of basis functions in Ω_j , sub-matrix $[A]_{ij} = A_h(\mathbf{u}, \mathbf{w})$ for $\mathbf{u}_{ap} \in \Omega_j$ and $\mathbf{w} \in \Omega_i$, and the corresponding right hand side, $\{\mathbf{f}\}_i = \mathcal{F}_h(\mathbf{w})$. It follows that given the redefinition of basis functions, one can alternatively redefine the vector of unknown coefficients as $\{\tilde{\mathbf{x}}\}_i = [U]_i \{\mathbf{x}\}_i$. Using

these definitions, matrix equation arising from the inner product can be written as

$$[\tilde{\mathbf{A}}_{ij}] = [\mathbf{U}]_i [\mathbf{A}]_{ij} [\mathbf{U}]_j^T$$

$$\{\tilde{\mathbf{f}}\}_i = [\mathbf{U}]_i \{\mathbf{f}\}_i$$
(3.51)

It is apparent from the preceding description that the SVD-based preconditioner is developed on a patch by patch basis. This implies that the number of operations scales as proportional to the number of patches in the domain. For instance, in a 2D problem, if there are N patches and p^{th} order basis functions are being used, then the total cost of performing the SVD scales as $\mathcal{O}(Np^6)$ and imposing required transformations scales as $\mathcal{O}(Np^4)$. This cost is derived using the fact that the matrices used in the transformation are block diagonal and not full. Given that $p = \mathcal{O}(1)$, the overall operation is typically proportional to the number of patches used in the domain. Thus, it is not very expensive to retrofit existing codes with this preconditioner and, in this case, considerably reduces the cost.

The error bound of the new set of basis functions can be obtained. Assuming that the threshold of singular value in $[D]_m$, used to remove the dependent basis functions, is defined as e_d . The approximated field can be represented by two set of basis functions as $\mathbf{u}_{ap} = \sum_k a_k \mathbf{S}_k = \sum_j c_j \tilde{\mathbf{S}}_j$. In each patch, we have $\{a\}_i^T = \{c\}_i^T [\mathbf{U}]_i$ where $\{a\}_i$ and $\{c\}_i$ are vectors representing the coefficients of original basis functions and reformatted basis functions in i^{th} patch respectively. In all N reformatted basis functions, we assume that N_1 of them are accounted with the singular values larger than e_d , then rest $N_2 = N - N_1$ of them are those which singular values are smaller than e_d which are removed as dependent basis functions. Number d_i denotes the singular value related to the basis function $\tilde{\mathbf{S}}_i$. For convenience, we assume that the first N_1 basis functions has singular value larger than e_d . Constant c_{max} represents the largest coefficient of reformatted basis

functions. The error bound can be derived as follows:

$$\|\mathbf{u} - \tilde{\mathbf{u}}_{ap}\|_{L^{2}(\Omega)} = \|\mathbf{u} - \sum_{i=1}^{N_{1}} c_{i} \tilde{\mathbf{S}}_{i}\|_{L^{2}(\Omega)}$$

$$= \|\mathbf{u} - (\sum_{i=1}^{N} c_{i} \tilde{\mathbf{S}}_{i} - \sum_{i=N_{1}+1}^{N} c_{i} \tilde{\mathbf{S}}_{i})\|_{L^{2}(\Omega)}$$

$$= \|\mathbf{u} - \sum_{i=1}^{N} c_{i} \tilde{\mathbf{S}}_{i}\|_{L^{2}(\Omega)} + \|\sum_{i=N_{1}+1}^{N} c_{i} \tilde{\mathbf{S}}_{i}\|_{L^{2}(\Omega)}$$

$$\leq \|\mathbf{u} - \mathbf{u}_{ap}\| + \sum_{i=N_{1}+1}^{N} c_{i} \|\tilde{\mathbf{S}}_{i}\|_{L^{2}(\Omega)}$$

$$\leq \|\mathbf{u} - \mathbf{u}_{ap}\|_{L^{2}(\Omega)} + \sum_{i=N_{1}+1}^{N} c_{i} \sqrt{d_{i}}$$

$$\leq \|\mathbf{u} - \mathbf{u}_{ap}\|_{L^{2}(\Omega)} + N_{2} c_{max} \sqrt{e_{d}}$$

$$(3.52)$$

Next, several results will be shown to demonstrate the efficacy of this SVD-based preconditioner. Figure 3.30 shows the condition number of the final system with different order of basis functions and different threshold e_d . Figure 3.30 shows that when the order of basis function increases, the condition number of the original matrix ($e_d = 0$) increases very fast, but with different threshold, the condition number increases slowly. Figure 3.31 shows the error of the solver with different threshold of preconditioner. It demonstrates that the errors are almost unchanged while the condition number of the system is reduced significantly. Figure 3.32 shows the condition number of the system with order of basis functions changing from 1 to 10. With different threshold, the condition number slowly increases.

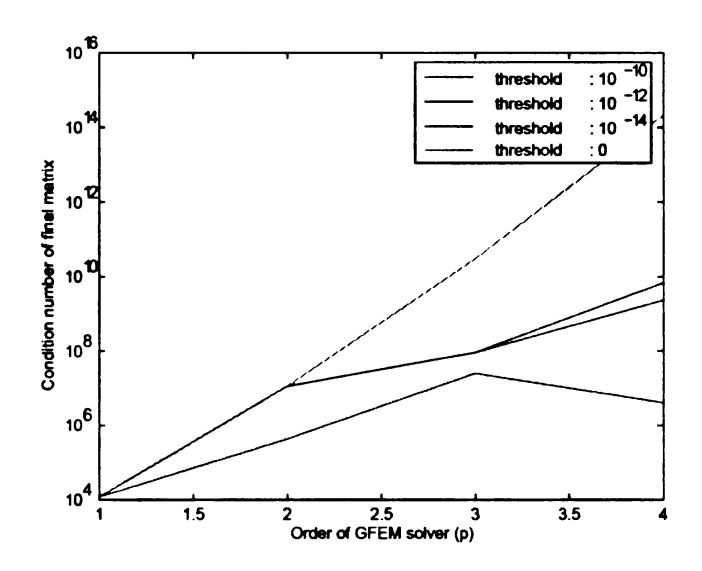


Figure 3.30. Condition number of system with differen order of basis functions (p = 1,...,4)

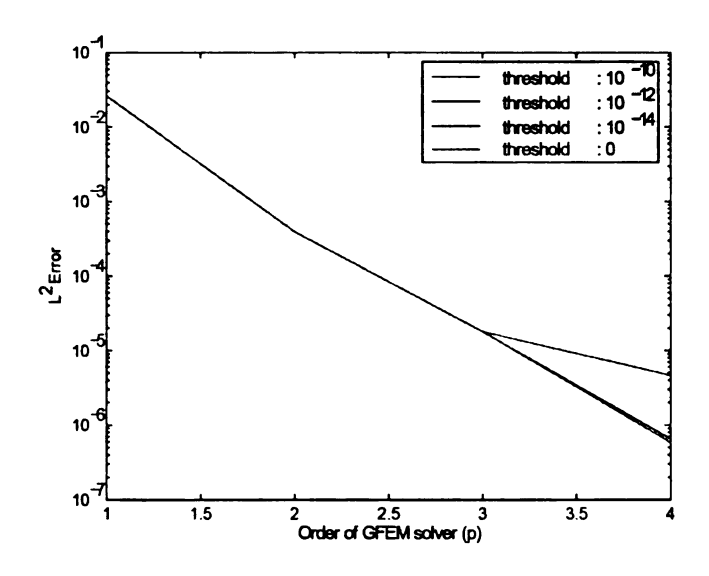


Figure 3.31. Error of the solver with differen order of basis functions

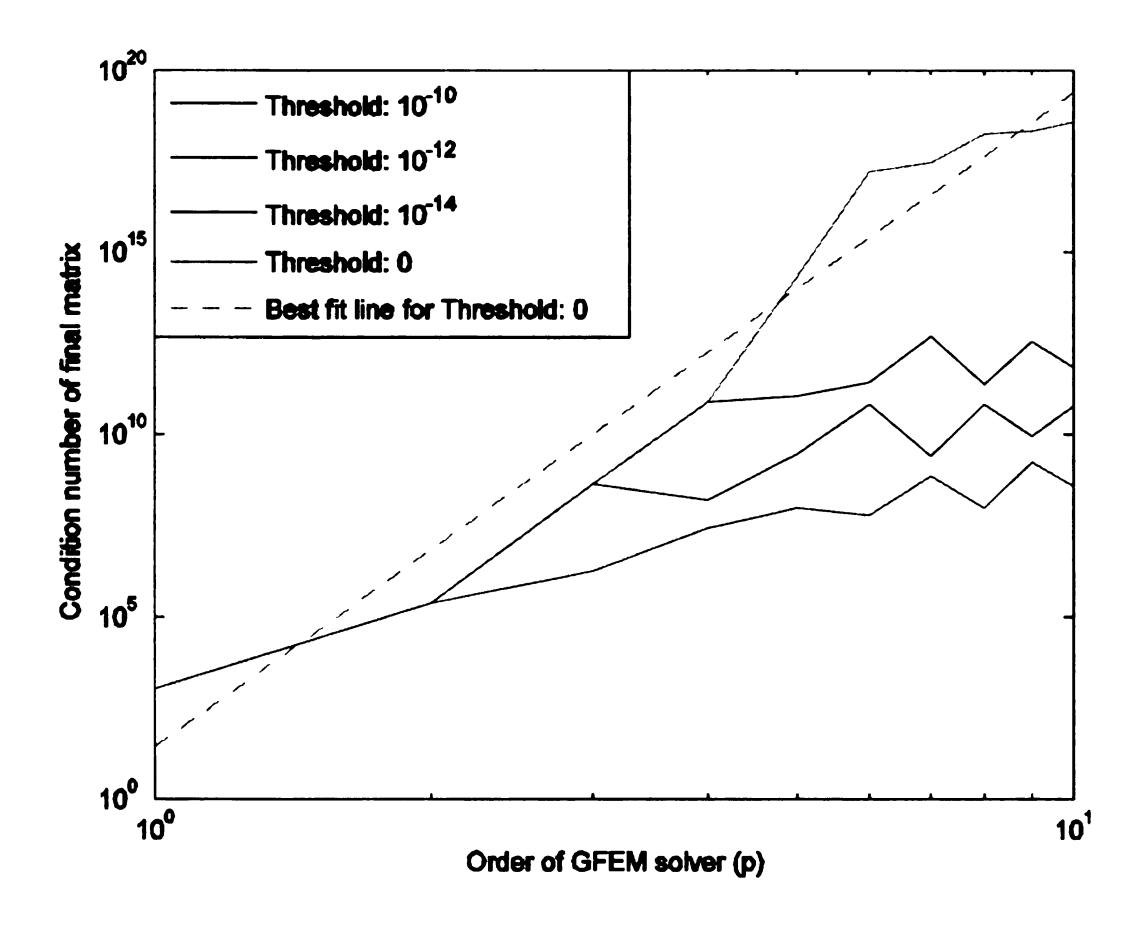


Figure 3.32. Condition number of system with different order of basis functions(p = 1,...,10)

CHAPTER 4

TIME DOMAIN GENERALIZED FINITE ELEMENT METHOD

4.1 Introduction

Transient analysis techniques that are based on differential equation based techniques have been popular, but this is largely due to finite difference time domain technique [65]. However, recent work in time domain finite element methods (TD-FEM) [1] has revived some of the interest in further development of this direction of research [66–68]. Recent developments in this area are truly exciting as they offer a viable and efficient alternative to FDTD. They inherently offer some advantages: (i) they conform to the object and (ii) it is possible to use higher order basis functions. An apparent disadvantage seems to be the fact that a straightforward approach implementation of TDFEM seems to be the cost required to obtain the solution at each time step. A novel approach to solving this problem was proposed in [1], and other recently developed methods permit more efficient time stepping.

The generalized finite element methods (GFEM) provide an intriguing analysis methodology, in that, it is a general framework for differential equation based analysis and permits the use of non-polynomial space of basis functions. Furthermore, the basis function space does not rely on an underlying mesh. This said, the enthusiasm has to be tempered largely due to the fact that while the potential of this method is considerable, progress still needs to be made to realize the kind of efficiency and flexibility that current day finite elements possess. The aim of this chapter is two-fold; (i) methods for time domain analysis using generalized finite element; and (ii) analysis that is easily portable to standard finite elements as well. Some of the inspiration for this work is drawn from our earlier work on time domain integral equations [69].

Classical TDFEM typically employs either central difference or the Newmark

method for time stepping; the latter is unconditionally stable, and both are accurate to second order. However, an alternative to these methods, is exploiting the fact that in any of these solver, we seek a response to a bandlimited source. This implies that one can exploit this to create both an alternative matching scheme, and well as a more efficient iterative scheme. Thus, the principal contributions of this chapter are as follows: (i) we will develop a time domain generalized finite element solver and prove/demonstrate convergence; (ii) we introduce a marching scheme based on approximate prolate spheroidal wave (APSW) functions and analyze stability; (iii) other marching schemes are analyzed for stability within the context of the TGFEM is provided; (iv) higher order convergence (time and space) is demonstrated. This chapter is organized as follows: Next, we will propose two high order time stepping schemes with error analysis. Then the stability analysis of the high order time stepping schemes will be provided. After that, we will propose one iterative solver. Finally, we will demonstrate the accuracy and stability of the technique with a host of numerical examples.

4.2 Formulation for Time domain GFEM solver

4.2.1 Discretization of time domain wave function

Consider a domain Ω_i whose boundary is denoted by $\partial\Omega := \Gamma = \bigcup_i \Gamma_i$. The electric (or the magnetic) field by $\mathbf{u}(\mathbf{r},t)$ satisfies the equation

$$\left(\nabla \times \left[\frac{1}{\alpha(\mathbf{r})}\nabla \times\right] + \gamma(\mathbf{r})\frac{\partial^{2}}{\partial t^{2}} + \beta(\mathbf{r})\frac{\partial}{\partial t}\right)\mathbf{u}(\mathbf{r},t) = -\frac{\partial \mathbf{f}(\mathbf{r},t)}{\partial t}$$

$$\mathcal{B}_{i}\left\{\mathbf{u}(\mathbf{r},t)\right\} = \mathbf{g}_{i}(\mathbf{r},t) \text{ for } \mathbf{r} \in \Gamma_{i}$$
(4.1)

where $\mathbf{f}(\mathbf{r},t)$ denotes the electric (or magnetic) source that is bandlimited to an angular frequency ω_{max} and is approximately quiescent for t < 0. In the above equations it is assumed that $\mathbf{r} \in \mathbb{R}^d$ for d = 2, 3, \mathcal{B}_i are differential operators, and $\mathbf{g}_i(\mathbf{r},t)$ is the function that is imposed on Γ_i . In what follows, we will describe the

manner in which solution to these equations may be obtained via the GFEM.

As is done in all discrete solution to PDEs, the function is represented in terms of space time basis functions of form

$$\mathbf{u}(\mathbf{r},t) = \sum_{j=1}^{N_t} \sum_{n=1}^{N_s} u_{jn} T(t - j\Delta_t) \mathbf{S}_n(\mathbf{r})$$
(4.2)

where N_t and N_s represent the number of temporal and spatial unknowns, T(t) and $\mathbf{S}_n(\mathbf{r})$ are the temporal and spatial basis functions, Δ_t is the time step size, and u_{jn} are the unknown coefficients need to be determined. The spatial basis functions are formulated in terms of GFEM space.

Next, we address the temporal basis functions or equivalently time stepping approaches. Three different types of time stepping approaches are investigated: (i) backward Lagrange; (ii) Newmark, and (iii) those resulting from using approximate prolate spheroidal wave (APSW) functions. As an aside, all time stepping schemes can be mapped into equivalent temporal basis functions. In what follows, we will use time stepping and temporal basis functions interchangeably. The APSW functions used here are those introduced by [70] and have been used extensively in the solution to time domain integral equations [69]:

$$T(t) = \frac{\sin(\chi \omega_{max} t)}{\chi \omega_{max} t} \frac{\sin\left[a\sqrt{(\frac{t}{N_p \Delta t})^2 - 1}\right]}{\sinh(a)\sqrt{(\frac{t}{N_p \Delta t})^2 - 1}}$$
(4.3)

In time domain, APSW function can be used as interpolatory function to the uniform time step size. χ is oversampling factor such that the sampling frequency $\omega_s = \chi \omega_{max}$ and $\Delta_t = \pi/\omega_s$. APSW function also has compact support. p is the half-width of the prolate, and T(t) = 0 for $|t| > (N_p + 1/2)\Delta_t$. $a = \pi N_p(\chi - 1)/\chi$ is the time bandwidth product. The error of approximation based on the APSW function

can be represented as

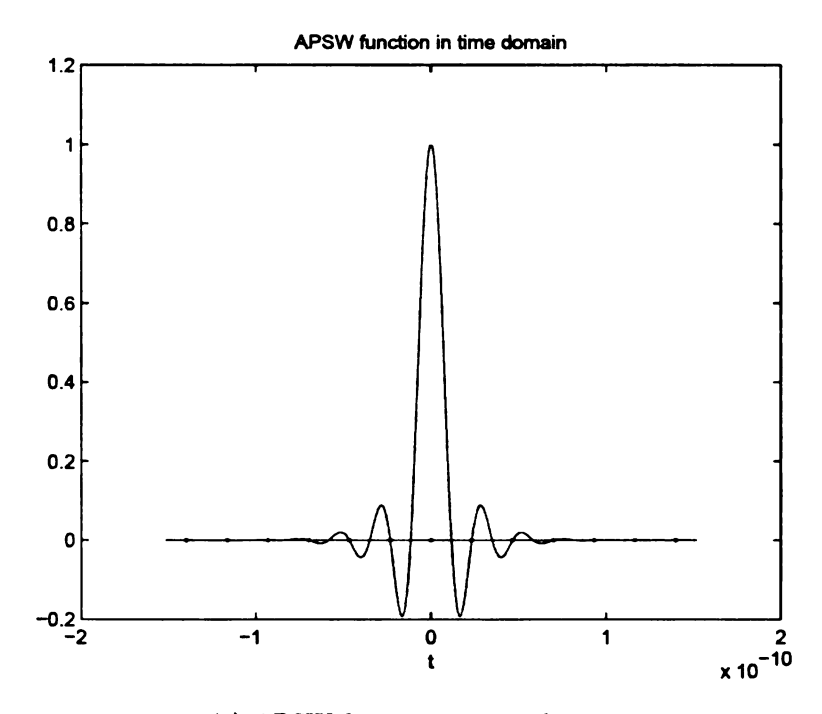
$$|f(t) - \sum_{k=-N}^{N} f(k\Delta t)T(t - k\Delta t)| \le \frac{M}{Sinh(a)} \sim O(e^{-Np\pi(\chi - 1)/\chi})$$
(4.4)

This function is band-limited to ω_{max} Figure 4.1 shows the APSW function in time and frequency domain. While these functions are bandlimited and approximately time-limited, they do not satisfy the march condition, i.e., they do not results in causal system that would enable a marching-on-in-time process. Means to overcome this have been prescribed [69], and will be summarized in the next subsection.

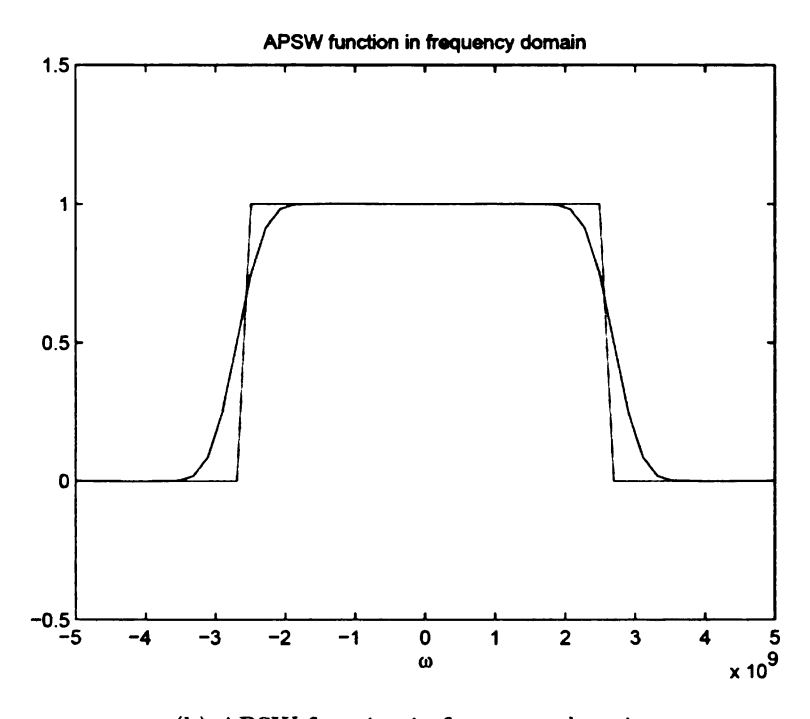
Lagrange polynomials can also be used as high order temporal function. Following definition shows that it can also be used as the interpolatory function in time domain.

$$T(t) = \frac{(t - \Delta t)(t - 2\Delta t)\cdots(t - p\Delta t)}{p!(\Delta t)^p}$$
(4.5)

But when order p is increased, the function is getting more and more oscillatory, e.g. the function is not band-limited. This makes the final system unstable. This property will be shown in the result section.



(a) APSW function in time domain



(b) APSW function in frequency domain

Figure 4.1. APSW function in time and frequency domain

4.2.2 Causal system for time domain wave equation

Finally, to derive the MOT system, we will use the approximation space defined earlier in (4.1). It will be assumed that the boundary condition on different portions of are defined to be either of the Dirichlet or Newmann type, i.e., $[\nabla \times \mathbf{u}(\mathbf{r},t)] \times \hat{n} = \mathbf{g}_1(\mathbf{r},t)$ and $\hat{n} \cdot \mathbf{u}(\mathbf{r},t) = g_2(\mathbf{r},t)$ are imposed on Γ_n , $\mathbf{u}(\mathbf{r},t) \times \hat{u}(\mathbf{r}) = \mathbf{g}_3(\mathbf{r},t)$ is imposed on Γ_d . Using Gelerkin testing in space results in the following bilinear form:

$$\begin{split} \mathcal{A}_{h}(\mathbf{u}, (\mathbf{S}_{m}(\mathbf{r}), t)) &= \mathcal{F}_{h} \\ \mathcal{A}_{h}(\mathbf{u}, (\mathbf{S}_{m}(\mathbf{r}), t)) &= \int_{\Omega} d\Omega \frac{1}{\alpha(\mathbf{r})} (\nabla \times \mathbf{S}_{m}(\mathbf{r})) \cdot (\nabla \times \mathbf{u}(\mathbf{r}, t)) \\ &+ \int_{\Omega} d\Omega \gamma(\mathbf{r}) \mathbf{S}_{m}(\mathbf{r}) \cdot \frac{\partial^{2} \mathbf{u}}{\partial t^{2}} (\mathbf{r}, t) \\ &+ \int_{\Omega} d\Omega \beta(\mathbf{r}) \mathbf{S}_{m}(\mathbf{r}) \cdot \frac{\partial \mathbf{u}}{\partial t} (\mathbf{r}, t) \\ &+ c_{1} \int_{\Omega} d\Omega (\nabla \cdot \mathbf{S}_{m}(\mathbf{r})) (\nabla \cdot \mathbf{u}(\mathbf{r}, t)) \\ &+ \int_{\Gamma_{d}} d\Gamma \frac{1}{\alpha(\mathbf{r})} (\nabla \times \mathbf{S}_{m}(\mathbf{r})) \cdot (\mathbf{u}(\mathbf{r}, t) \times \hat{n}) \\ &+ \int_{\Gamma_{d}} d\Gamma \frac{1}{\alpha(\mathbf{r})} (\mathbf{S}_{m}(\mathbf{r}) \times \hat{n}) \cdot (\nabla \times \mathbf{u}(\mathbf{r}, t)) \\ &+ c_{2} \int_{\Gamma_{n}} d\Gamma (\mathbf{S}_{m}(\mathbf{r}) \times \hat{n}) (\mathbf{u}(\mathbf{r}, t) \times \hat{n}) \\ &+ c_{3} \int_{\Gamma_{d}} d\Gamma (\mathbf{S}_{m}(\mathbf{r}) \times \hat{n}) \cdot (\mathbf{u}(\mathbf{r}, t) \times \hat{n})) \\ &\mathcal{F}_{h} &= -\int_{\Omega} d\Omega \mathbf{S}_{m}(\mathbf{r}) \cdot \frac{\partial \mathbf{J}_{1}}{\partial t} (\mathbf{r}, t) + \int_{\Gamma_{n}} d\Gamma \mathbf{S}_{m}(\mathbf{r}) \cdot \mathbf{g}_{1}(\mathbf{r}, t) \\ &+ c_{2} \int_{\Gamma_{n}} d\Gamma g_{2}(\mathbf{r}, t) (\mathbf{S}_{m}(\mathbf{r}) \times \hat{n}) \\ &+ \int_{\Gamma_{d}} d\Gamma \frac{1}{\alpha(\mathbf{r})} \mathbf{g}_{3}(\mathbf{r}, t) \cdot [\nabla \times \mathbf{S}_{m}(\mathbf{r}) \times \hat{n}] \\ &+ c_{3} \int_{\Gamma_{d}} d\Gamma \mathbf{g}_{3}(\mathbf{r}, t) \cdot (\mathbf{S}_{m}(\mathbf{r}) \times \hat{n}) \end{split}$$

where c_1 , c_2 and c_3 are constants to include penalty terms and additional boundary condition respectively (we have shown in [71] that while these terms are not

absolutely necessary for h-, p- convergence, the convergence is smoother if these conditions are imposed).

Substituting (4.2) to (4.6) and using point testing in time, results in an MOT equations. For different time stepping schemes (equivalently temporal different basis functions), these equations may be written as $\sum_{j=-\kappa_1}^{\kappa_2} \mathbf{Z}_j \mathbf{I}_{i-j} = \mathbf{V}_i$. In this equation, $\begin{bmatrix} I_j \end{bmatrix}_n = u_{jn}$, $[V_i]_m = \mathcal{F}_m|_{t=t_i}$, and $\mathcal{Z}_i = \mathcal{A}|_{t=t_i}$, $\kappa_1 + \kappa_2 + 1$ is the number of time steps included in the temporal support of the time basis function. When using backward Lagrange or Newmark time stepping schemes, the resulting system of equations is causal, e.g. $\kappa_1 = 0$. This is not the case when using APSW functions. The solution to this problem maybe obtained using an extrapolation scheme prescribed by either [69] or [72] to make the MOT system causal. More specifically, extrapolation coefficients h_p^q is applied to approximate the unknown vector I_{i-j} with j < 0 based on the N_{samp} solved vector I_{i-j} with $j \ge 0$ and $N_{samp} \le \kappa_2 + 1$.

$$\mathbf{I}_{j+p} = \sum_{q=1-N_{samp}}^{0} h_p^q \mathbf{I}_{j+q}$$
 (4.7)

Explicit expression for the matrices can be easily obtained. As is evident from the above exposition, these equations can be used in a stepwise manner to obtain the fields for all time. Next, the error bound of the time domain GFEM solver will be analyzed.

4.2.3 Error bound of Time domain GFEM solver

The error bound of this time domain solver can be analyzed. We assume $\hat{f}(x)$ and $\hat{g}(x)$ are approximation of linear operators f(x) and g(x). Given the error of the approximation

$$f(x) = \hat{f}(x) + e(f(x))$$

$$g(x) = \hat{g}(x) + e(g(x))$$
(4.8)

Then the error of approximation of operator f(g(x)) is

$$f(g(x)) = f(\hat{g}(x) + e(g(x)))$$

$$= f(\hat{g}(x)) + f(e(g(x)))$$

$$= \hat{f}(\hat{g}(x)) + e(f(\hat{g}(x)) + f(e(g(x))))$$

$$= \hat{f}(\hat{g}(x)) + O(e(f(\hat{g}(x)))) + O(e(g(x)))$$

$$= \hat{f}(\hat{g}(x)) + O(e(f(g(x)) + e(g(x)))) + O(e(g(x)))$$

$$= \hat{f}(\hat{g}(x)) + O(e(f(g(x)))) + O(e(g(x))) + O(e(f(e(g(x)))))$$

$$\approx \hat{f}(\hat{g}(x)) + O(e(f(g(x)))) + O(e(g(x)))$$

$$(4.9)$$

The difference between both sides of \approx is small when e(g(x)) << g(x) and e(f(x)) << f(x). The theorem shows that the error of two operators can be approximated by the summation of the error of two operators. So in (4.6), errors of the \mathcal{A}_h and \mathcal{F}_h are

$$e(\mathcal{A}_h) = O(e(\nabla \times \mathbf{u})) + O(e(\mathbf{u})) + O(e(\nabla \cdot \mathbf{u})) + O(e(\mathbf{u} \times \hat{n})) + O(e(\mathbf{u} \cdot \hat{n}))$$

$$+ O(e(\frac{\partial^2}{\partial t^2} f(t))) + O(e(\frac{\partial}{\partial t} f(t))) + O(e(f(t)))$$

$$e(\mathcal{F}_h) = O(e(\mathbf{u})) + O(e(\mathbf{u} \cdot \hat{n})) + O(e(\mathbf{u} \times \hat{n})) + O(e(\nabla \times \mathbf{u} \times \hat{n}))$$

$$(4.10)$$

In [73], the order of the error of GFEM basis functions $O(e(\mathbf{u}))$ is the same as error of local approximation function. In the above formulas, $O(e(\mathbf{u}))$, $O(e(\mathbf{u} \times \hat{n}))$ have the same order accuracy and $O(e(\nabla \times \mathbf{u} \times \hat{n}))$, $O(e(\nabla \times \mathbf{u}))$ and $O(e(\nabla \cdot \mathbf{u}))$ are one order lower.

In time domain, $O(e(\frac{\partial^2}{\partial t^2}f(t)))$, $O(e(\frac{\partial}{\partial t}f(t)))$, O(e(f(t))) are used to represent the error of the numerical approximation of the time domain operators. The follows are the errors of different time stepping schemes:

Backward Difference:

$$O(e(\frac{\partial^2}{\partial t^2}f(t))) = O(\Delta t)$$

$$O(e(\frac{\partial}{\partial t}f(t))) = O(\Delta t)$$

$$O(e(f(t))) = 0$$
(4.11)

Forward Difference:

$$O(e(\frac{\partial^2}{\partial t^2}f(t))) = O(\Delta t)$$

$$O(e(\frac{\partial}{\partial t}f(t))) = O(\Delta t)$$

$$O(e(f(t))) = 0$$
(4.12)

Central Difference:

$$O(e(\frac{\partial^2}{\partial t^2}f(t))) = O((\Delta t)^2)$$

$$O(e(\frac{\partial}{\partial t}f(t))) = O((\Delta t)^1)$$

$$O(e(f(t))) = 0$$
(4.13)

p-order Lagrange polynomials interpolation:

$$O(e(\frac{\partial^2}{\partial t^2}f(t))) = O((\Delta t)^{p-1})$$

$$O(e(\frac{\partial}{\partial t}f(t))) = O((\Delta t)^p)$$

$$O(e(f(t))) = O(((\Delta t)^{p+1}))$$
(4.14)

Approximate prolate spheroidal wave(APSW) functions with width parameter

$$O(e(\frac{\partial^2}{\partial t^2}f(t))) = O(\frac{1}{\Delta t^2}e^{-\pi^2 N/\omega_0 \Delta t})$$

$$O(e(\frac{\partial}{\partial t}f(t))) = O(\frac{1}{\Delta t}e^{-\pi^2 N/\omega_0 \Delta t})$$

$$O(e(f(t))) = O(e^{-\pi^2 N/\omega_0 \Delta t})$$
(4.15)

4.3 Analysis of stability

The analysis of stability is a very important issue in this time-marching scheme. The criteria of stability in discrete signal system is utilized in this paper to analyze whether and when the system is stable. The bilinear form equation (4.6) can be expressed as:

$$[\mathbf{S}]\{\mathbf{u}(t_s)\} + [\mathbf{Q}]\{\ddot{\mathbf{u}}(t_s)\} = \mathbf{f}(t_s) \tag{4.16}$$

where $(i-1)\Delta t < t_s \le i\Delta t$ and the current time can be represented as $t_s = i\Delta t + t'$. Approximating the time domain result by temporal basis function T(t) where T(t) = 0 for $|t| > (N + \frac{1}{2})\Delta t$, the equation can be discretized further as:

$$\sum_{j=i-N}^{i+N} [S] \{I\}_j T(-j\Delta t + t_s) + \sum_{j=i-N}^{i+N} [Q] \{I\}_j T(-j\Delta t + t_s) = \{V(t_s)\}$$
 (4.17)

With extrapolation algorithm in (4.7), this equation can be rewritten as:

$$\sum_{j=i-N}^{i} ([\mathbf{S}]\{\mathbf{I}\}_{j} \bar{a}_{j-i+N} + [\mathbf{Q}]\{\mathbf{I}\}_{j} \bar{b}_{j-i+N}) = \{\mathbf{V}(t_s)\}$$
(4.18)

where

$$\bar{a}_{i} = \begin{cases} T((N-i)\Delta t + t') \\ (i = 0, \dots, N - N_{samp}) \\ T((N-i)\Delta t + t') + \sum_{j=N+1}^{2N} T((N-j)\Delta t + t')h_{j-N}^{i-N} \\ (i = N+1-N_{samp}, \dots, N) \end{cases}$$
(4.19)

$$\bar{b}_{i} = \begin{cases} \ddot{T}((N-i)\Delta t + t') \\ (i = 0, \dots, N - N_{samp}) \\ \ddot{T}((N-i)\Delta t + t') + \sum_{j=N+1}^{2N} \ddot{T}((N-j)\Delta t + t')h_{j-N}^{i-N} \\ (i = N+1-N_{samp}, \dots, N) \end{cases}$$
(4.20)

The period time Δt should be extracted from \bar{a}_i and \bar{b}_i , so by stretching the temporal function $\tilde{T}(t) = T(\frac{t}{\Delta t})$ and using $\tilde{t}' = \frac{t'}{\Delta t}$, The following equation with normalized form is obtained:

$$\sum_{i=0}^{N} ([\mathbf{S}]a_i + \frac{[\mathbf{Q}]b_i}{(\Delta t)^2}) \{\mathbf{I}\}_{i+j} = \{\mathbf{V}(t_s)\}$$
(4.21)

where

$$a_{i} = \begin{cases} \tilde{T}((N-i) + \tilde{t}') \\ (i = 0, \dots, N - N_{samp}) \\ \tilde{T}((N-i) + \tilde{t}') + \sum_{j=N+1}^{2N} \tilde{T}((N-j) + \tilde{t}') h_{j-N}^{i-N} \\ (i = N+1 - N_{samp}, \dots, N) \end{cases}$$
(4.22)

$$b_{i} = \begin{cases} \ddot{T}((N-i) + \tilde{t}') \\ (i = 0, \dots, N - N_{samp}) \\ \ddot{T}((N-i) + \tilde{t}') \sum_{j=N+1}^{2N} \ddot{T}((N-j) + \tilde{t}') h_{j-N}^{i-N} \\ (i = N+1 - N_{samp}, \dots, N) \end{cases}$$
(4.23)

The z-transform of the left side of the above equation result in the equation:

$$\{\sum_{i=0}^{N} ([\mathbf{S}]a_i + \frac{[\mathbf{Q}]b_i}{(\Delta t)^2})z^i\}\{\mathbf{I}\}_j = 0$$
(4.24)

or

$$-\frac{\sum_{i=0}^{N} b_i z^i}{\sum_{i=0}^{N} a_i z^i} \{ \mathbf{I} \}_j = (\Delta t)^2 [\mathbf{Q}]^{-1} [\mathbf{S}] \{ \mathbf{I} \}_j$$
 (4.25)

		i = 0	i = 1	i = 2	i = 3	i=4	i = 5	i=6
$N_{samp} =$	a_i	0.0	0.0	0.0	0.0	0.0	0.0	1.0
4	b_i	-6.01e-5	1.04e-3	-8.93e-3	-0.973	3.964	-4.976	1.994
$N_{samp} =$	a_i	0.0	0.0	0.0	0.0	0.0	0.0	1.0
5	b_i	1.0-6.01e-5	1.04e-3	0.912	-4.658	9.489	-8.660	2.915

Table 4.1. The coefficients of characteristic equation

It's easy to find that $-(\sum_{i=0}^N b_i z^i)/(\sum_{i=0}^N a_i z^i)$ is the eigenvalue of matrix $(\Delta t)^2[\mathbf{Q}]^{-1}[\mathbf{S}]$ and written as λ , then

$$\sum_{i=0}^{N} (b_i + \lambda a_i) z^i = 0 (4.26)$$

The condition of stability for the above system, or called the λ -system, is that all the roots of equation (4.26) are in the unit circle. If there is a number λ_{max} when $\forall \lambda \in [0, \lambda_{max}]$, all roots of z are in the unit circle, e.g. λ -system is stable, then the time stepping scheme is conditionally stable with the criteria $\Delta t < \sqrt{(\lambda_{max})/(\rho([\mathbf{Q}]^{-1}[\mathbf{S}]))}$. Analysis of the stability by characteristic equation (4.26) w.r.t z can be transferred to the characteristic equation w.r.t. w using $z = \frac{1+w}{1-w}$, where the stability criteria is that all roots of w should lies at the left side of the complex plane. Then Routh criteria can be utilized to analyze the stability of the system.

An experiment will be presented to demonstrate the feasibility of the above scheme. In the experiment, APSW function is chosen as temporal basis function with testing point t'=0, the parameter chosen is $\Delta t=2.33\times 10^{-11}s$, $N_{samp}=4$, N=6. The coefficients of characteristic equation is shown in the Table 4.1. When $\lambda \in [0,100]$, Figure 4.2 shows the stability of λ -system based on both Rough criteria and the numerical solution of λ -system. When Rough criteria is implemented, value 1 shows that the λ -system is unstable and value 0 represents that the system is

stable. It shows that $\forall \lambda \in [0, 100]$, the λ -system is stable. The appropriate Δt can be chosen to make the approach stable. In the same figure, with different λ , the largest amplitude of roots of z in Figure 4.2 is computed by intrinsic subroutine in Matlab. From the figure, we can see that they match with each other. Another experiment is also presented with $N_{samp} = 5$ and all other parameter unchanged. The coefficients of characteristic equation is also shown in the table. From the Figure 4.3, We can obtain the conclusion that there is no λ_{max} can be chosen so that $\forall \lambda \in [0, \lambda_{max}]$, the system is stable. So the time-marching system is unconditioned unstable. Figure 4.4 and Figure 4.5 show the same results with smaller region of λ which make the details of the figures around the origin clearer.

4.4 Iterative Solver

The main bottleneck in using TD(G)FEM as opposed to FDTD is the fact that the resulting systems are not explicit. This problem is exacerbated if the basis functions are higher order. One way to overcome this problem in TDFEM is to develop basis function that are orthogonal in each subdomain [1]. While this approach is efficient, it does sacrifice higher order spatial convergence. Using a SVD approach to define orthogonal basis functions in TDGFEM permits higher order convergence. Another fact that can be exploited is the fact that the signals analyzed are bandlimited. This implies that one can make use of extrapolation schemes described earlier, but within the iterative scheme. We shall dwell on the latter in a little more detail.

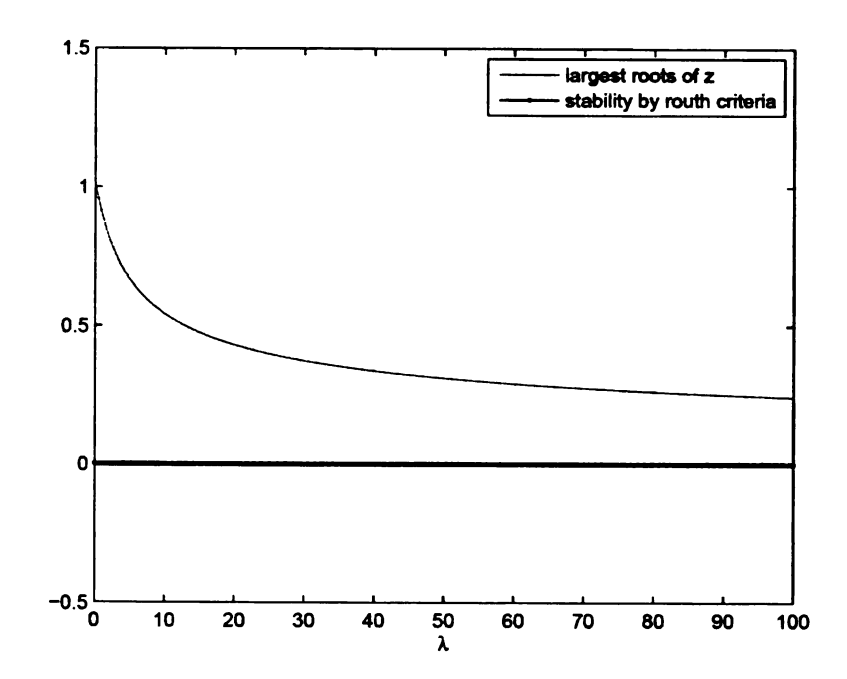


Figure 4.2. Stability of system with $N_{samp} = 4$

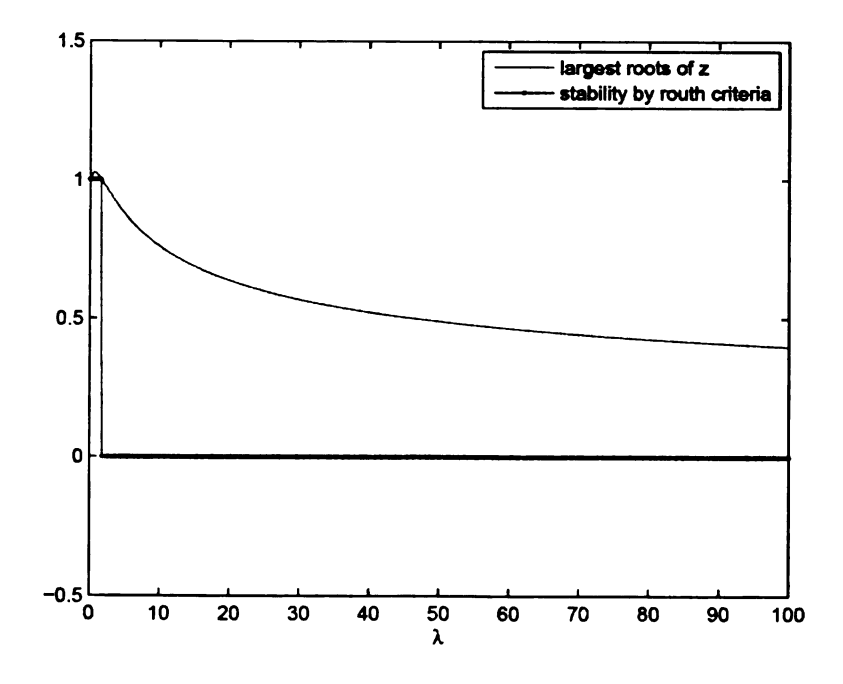


Figure 4.3. Stability of system with $N_{samp}=5$

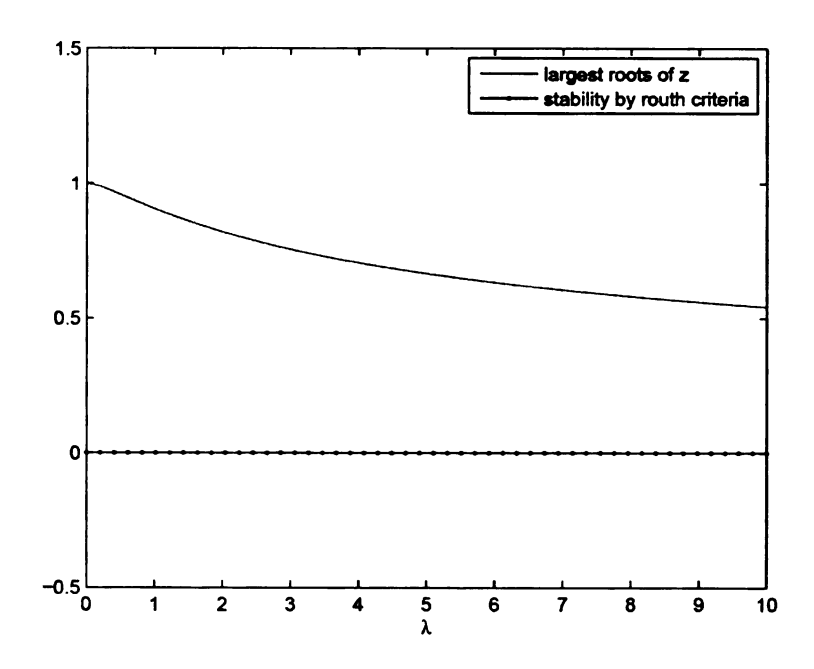


Figure 4.4. Stability of system with $N_{samp}=4$

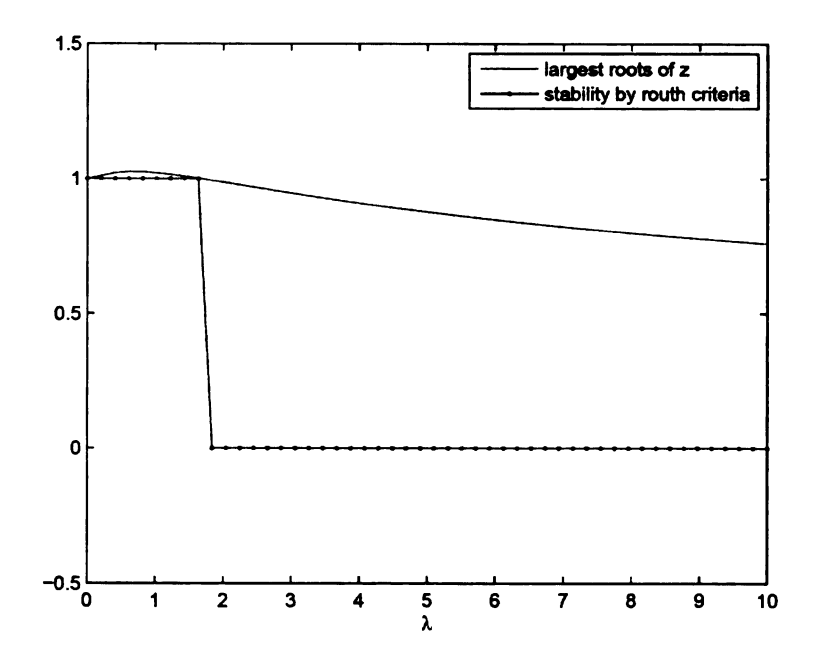


Figure 4.5. Stability of system with $N_{samp}=5$

At any instant of time t_i , the MOT system of equations can be written as $[\mathbf{Z}]_0\{\mathbf{I}\}_i=\{\widetilde{\mathbf{V}}\}$. It follows from the above arguments that $\{\mathbf{I}\}_i$ can be estimated in terms of $\{\mathbf{I}\}_j$ for $j=i-N_{ex}-1,...,i-1$. Next, the matrix $[\mathbf{Z}]_0$ can be subdivided into submatrices $[\mathbf{Z}]_{0,mn}$ where the subscript $\{mn\}$ indicates an interaction between the m^{th} and n^{th} patch. In terms of sub-matrices, the iteration can be re-written as $[\mathbf{Z}]_{mm}\{\mathbf{I}\}_i=\{\widetilde{\mathbf{V}}\}_i-\partial_{mn}[\mathbf{Z}]_{mn}\{\widetilde{\mathbf{I}}\}_i$ where $\{\widetilde{\mathbf{I}}\}_i$ is an extrapolated estimate of $\{\mathbf{I}\}_i$. This provides the first step of the iterative solver. One can build upon this to provide the next guess, and so on. This iterative process is rapidly convergent for an L_2 error norm of 10^{-8} . It is not as robust for lower error requirements.

4.5 Numerical Experiments

In what follows, we shall present a series of numerical experiments that will serve to demonstrate the accuracy and stability of the time domain GFEM presented in this paper. These fall into three classes: First, we will focus on the stability issue when different boundary conditions are imposed in homogeneous domain. Second, we will demonstrate h-, p- convergence of spatial basis functions. Then, the convergence of TDGFEM for different temporal schemes in two- or three-dimensions, homogeneous or inhomogeneous domain is demonstrated. Finally, we will shows the results of TDGFEM with iterative solver.

First, consider a homogeneous rectangular computational domain $\Omega=(0,1)^2$ with boundary $\Gamma=\bigcup_i^4\Gamma_i$ where $\{\Gamma_1:\mathbf{r}\in 0\times (0,1)\},\ \{\Gamma_2:\mathbf{r}\in (0,1)\times 1\},\ \{\Gamma_3:\mathbf{r}\in 1\times (0,1)\},\ \{\Gamma_4:\mathbf{r}\in (0,1)\times 0\}.$ In this domain, it is assumed that the electric field is of the form

$$\mathbf{E}(\mathbf{r},t) = \hat{y}2(t + \frac{x - x_0}{c})/\tau^2 exp\{-(t + \frac{x - x_0}{c})^2/\tau^2\}$$
 (4.27)

where $x_0 = 5.5$ and $\tau = 3.15 \times 10^{-9} s$. The solution to (4.1) is solved by imposing the analytical solution as either Neumann, Dirichlet or Impedance boundary condition.

In this experiment, all nodes are distributed uniformly, and rectangular patches are used. The size of each patch is chosen to be 1.5 times the distance between the nodes. The weight functions $W_i(\mathbf{r})$ is a tensor product rooftops, and the local approximation function $v_{i,m}(\mathbf{r})$ and $v_{i,n}(\mathbf{r})$ are tensor product of Legendre polynomials. The parameters of spatial basis functions are $h=0.38\lambda$ and p=3. APSW functions are used for as temporal basis. The half width of prolate function N_p and the number of sample points for extrapolation N_{samp} are 6 and 4, respectively. The time step size is $\Delta t = 2.33 \times 10^{-11} s$. Linear equation is solved by SVD techniques. Figure 4.6, Figure 4.7, Figure 4.8 shows analytical and numerical results at location (0.44, 0.44) with Dirichlet boundary condition, Neumann boundary condition and impedance boundary condition. From these figures, we can see when Dirichlet boundary condition and Neumann boundary condition are imposed, the solutions are corrupted by interior resonance modes. As is expected, unique solutions are obtained when using the impedance boundary condition.

Next, we will demonstrate the h- and p- convergence of spatial basis functions in time domain GFEM solver. In this experiment, the rectangular computation domain and other parameters about meshes (size of the meshes, distribution of the nodes) are exactly the same with the last example, so as the electric field solution of the time domain wave equation. Impedance boundary condition is imposed. When temporal basis functions are the same APSW functions with those in the last example, spatial basis functions are changing with $h=0.76\lambda,0.38\lambda,0.25\lambda$ and p=1,2. Temporal basis functions and time step size are identical to those used earlier. The total number of time steps is 6000. The results are L^2 norm of relative error evaluated at uniformly distributed 10×10 sample points at all 6000 time steps. Linear equation is solved by SVD techniques, too. Figure 4.9 demonstrates the h-, p- convergence of the spatial basis functions.

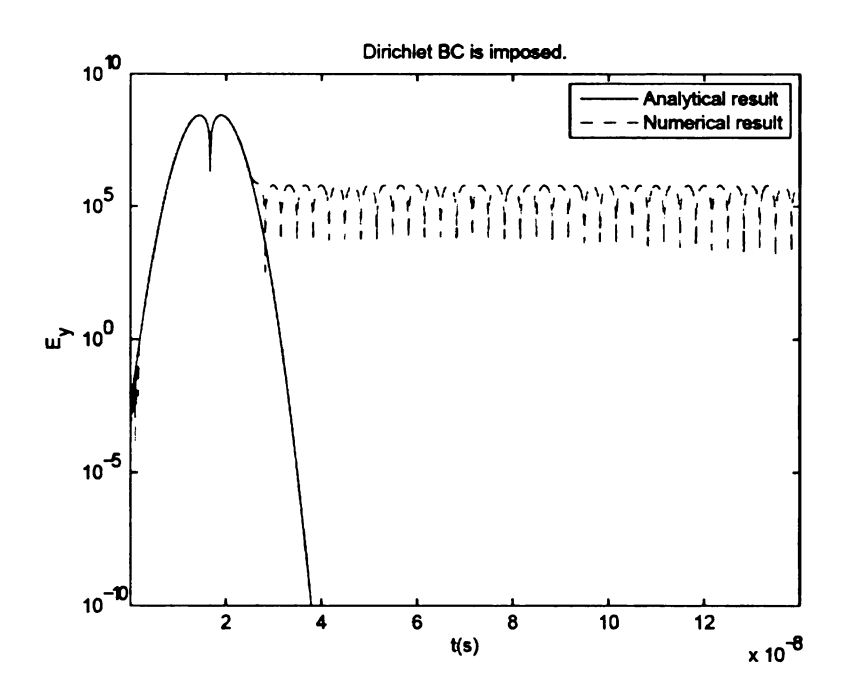


Figure 4.6. Analytical and numerical result with Dirichlet BC

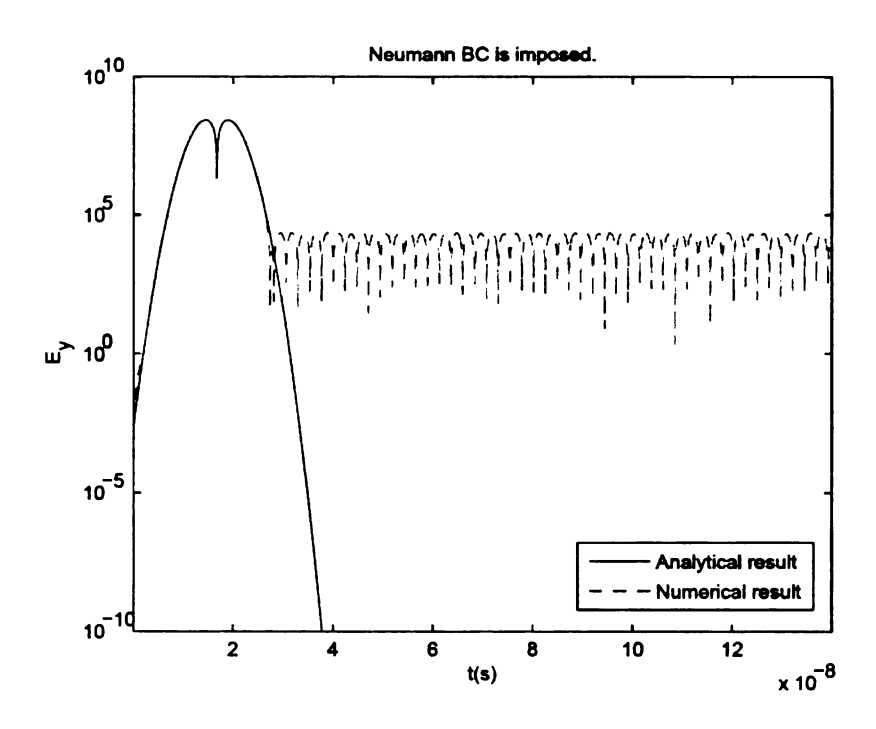


Figure 4.7. Analytical and numerical result with Neumann BC

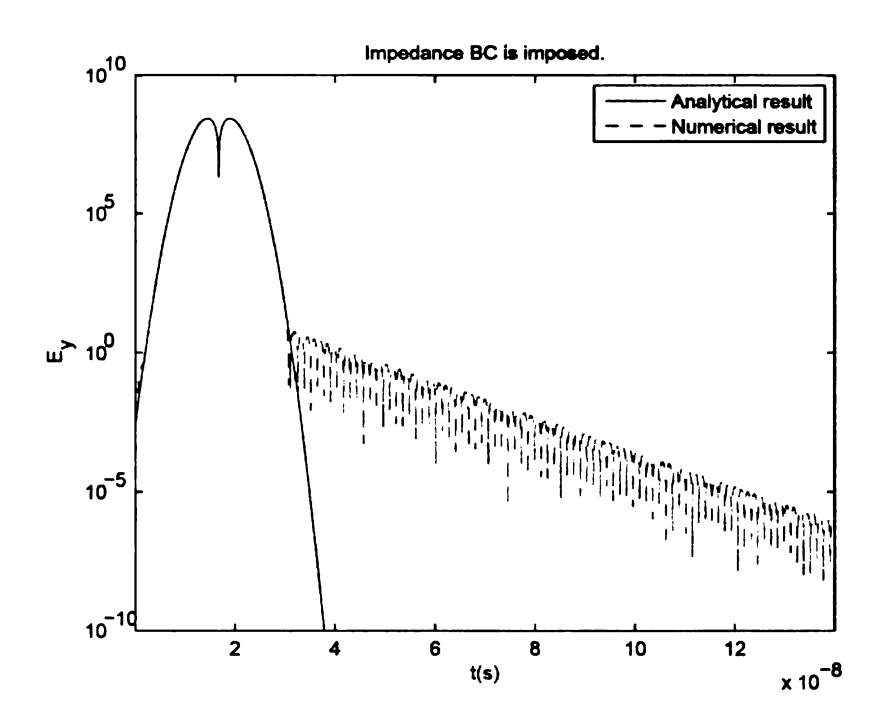


Figure 4.8. Analytical and numerical result with Impedance BC

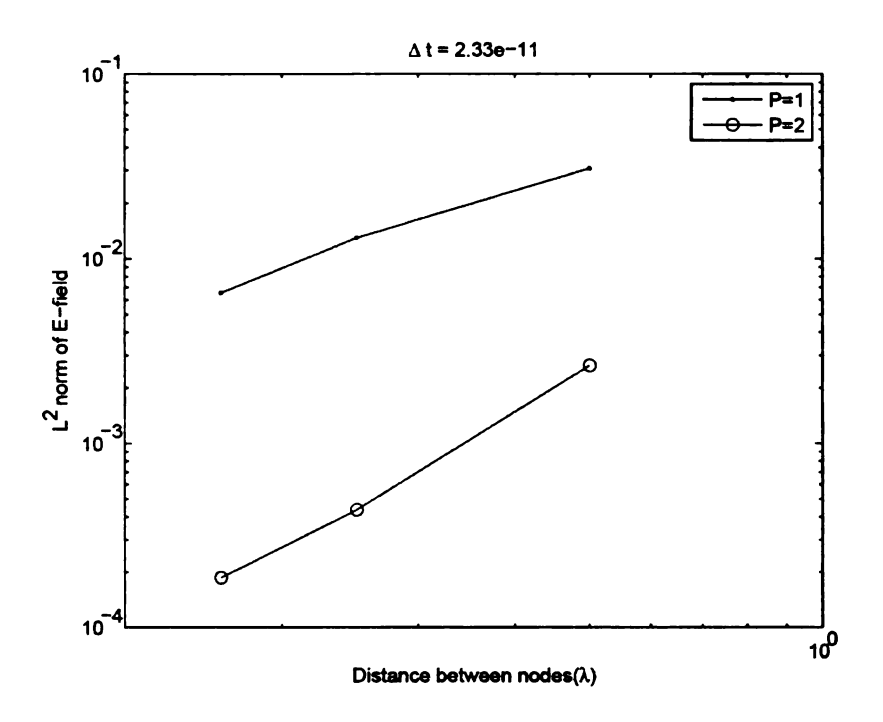


Figure 4.9. h-p- convergence of the spatial basis function

In the next series of examples, we will demonstrate the convergence of different temporal schemes in two- or three-dimension, homogeneous or inhomogeneous domain. Three kinds of temporal schemes are tested: scheme based on APSW functions, scheme based on lagrange polynomials and Newmark scheme. First, in 2D homogeneous domain, the electric field solution of the time domain wave equation, the computation domain and parameters for the mesh constructor are the same as in the last example, the spatial basis functions are also defined in the same way with $h=0.38\lambda$ and p=3. Impedance boundary condition is imposed. When APSW functions are used as temporal basis functions, the half width is varied from 3 to 6 and the number of sample points for extrapolation $N_{samp}=4$. When Lagrange polynomials are used, the order changed from 3 to 4, and Newmark - β method is used, β is chosen as 0.4, 0.6, 0.8. The time step size is $\Delta t=2.33\times 10^{-11}s$. The results are L^2 norm of relative error evaluated at uniformly distributed 10×10 sample

points at all 6000 time steps. Figure 4.10 shows the errors of all three schemes. From the figure, we can see the error is reduced with the increasing of the Lagrange polynomials' order and the half width of the APSW functions. The errors of Newmark $-\beta$ method are almost the same with different β . When we increase the number of sample points for extrapolation N_{samp} beyond 4, the system is unstable. This unlike what is observed in time domain integral equation. This is the principal reason for the lack of convergence of this scheme.

Next, we will demonstrate the similar thing in 2D inhomogeneous media. Consider a 2D inhomogeneous domain, the computational domain is defined by $\Omega=\Omega^++\Omega^-$ with $\Omega^+=(0,1)\times(0.5,1)$ and $\Omega^-=(0,1)\times(0,0.5)$. The relative permitivity in Ω^+ and Ω^- are chosen to be $\varepsilon_r=1,3$, respectively. The fields are as follows: $\forall \mathbf{r}\in\Omega^+$ the electric field is $\mathbf{E}(\mathbf{r},t)=\hat{x}\{2(t+\frac{y-y_0}{c})/\tau^2exp[-(t+\frac{y-y_0}{c})^2/\tau^2]+2R(t-\frac{(y-0.5)}{c}+\frac{y-y_0}{c})/\tau^2exp[-(t-\frac{(y-0.5)}{c}+\frac{y-y_0}{c})^2/\tau^2]\}$, and $\forall \mathbf{r}\in\Omega^-$ the electric field is $\mathbf{E}(\mathbf{r},t)=\hat{x}2T(t+\frac{y-0.5}{c}\sqrt{3}+\frac{y-y_0}{c})/\tau^2exp[-(t+\frac{y-0.5}{c}\sqrt{3}+\frac{y-y_0}{c})^2/\tau^2]$ where $R=\frac{1-\sqrt{3}}{1+\sqrt{3}}, T=\frac{2}{1+\sqrt{3}}, y_0=5.5$ and $\tau=3.15\times10^{-9}s$. The solution to (4.1) is solved by imposing the analytical solution as impedance boundary condition. The mesh parameters (size of the meshes, distribution of the nodes), the basis functions in spatial domain and temporal basis in time domain are identical to those in the last example. The results are L^2 norm of relative error evaluated at uniformly distributed 10times10 sample points at all 6000 time steps. Figure 4.11 shows that the result is similar to those obtained in two dimension homogeneous simulation.

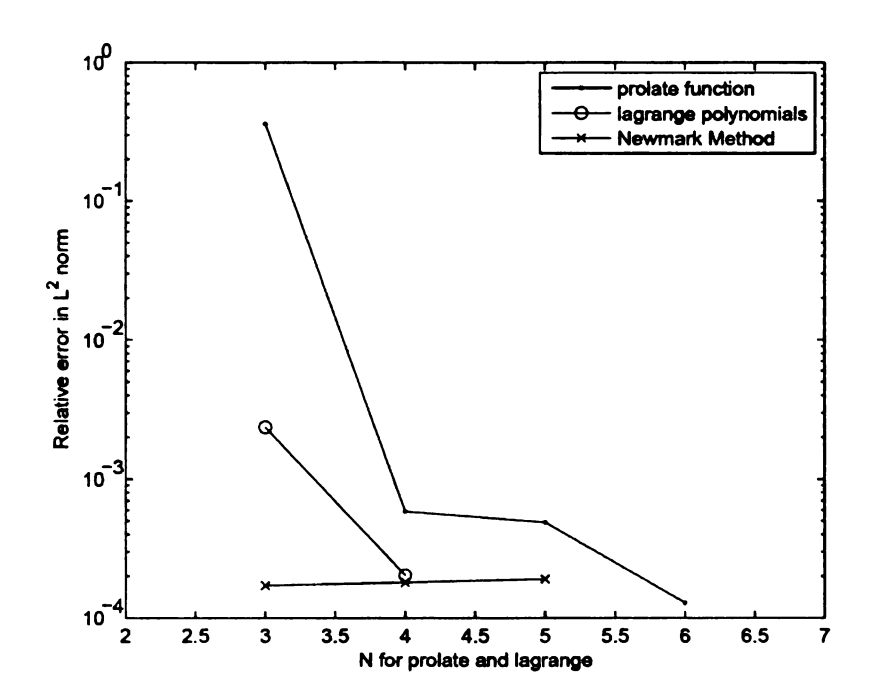


Figure 4.10. Convergence of different temporal scheme in 2D homogeneous problem

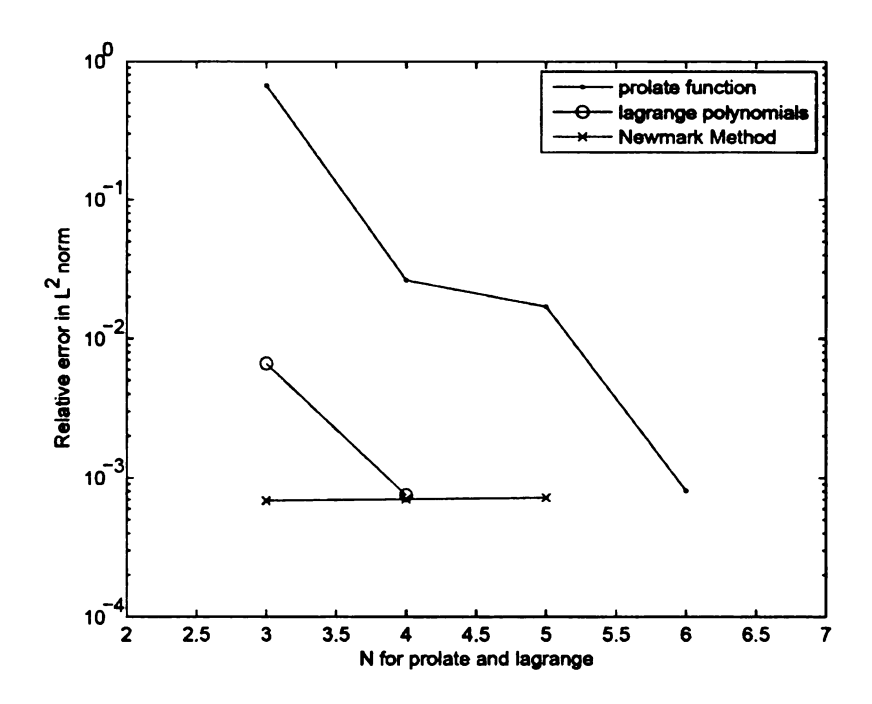


Figure 4.11. Convergence of different temporal scheme in 2D inhomogeneous problem

Next, we will demonstrate the similar thing in 3D homogeneous domain. Consider a homogeneous computation domain $\Omega^+ = (0,1) \times (0,1) \times (0,1)$. In this domain, it is assumed that the electric field is of the form $\mathbf{E}(\mathbf{r},t) = \hat{y}2(t+\frac{x-x_0}{c})/\tau^2 \exp\{-(t+\frac{x-x_0}{c})^2/\tau^2\}$ where $x_0=5.5$ and $\tau=3.15\times 10^{-9}s$. All other parameters, viz., distribution of nodes, overlap, definition of spacial basis functions and temporal basis functions, time step size, etc, are identical to those used earlier and just extend to 3D case. and the L^2 error norm is evaluated at $5\times 5\times 5$ uniformly distributed sample points. The results shown in Figure 4.12 demonstrate the convergence of TDGFEM solver in 3D.

Next, we will demonstrate the feasibility of the solver in 3D inhomogeneous domain. Consider a inhomogeneous computation domain $\Omega=\Omega^++\Omega^-$ with $\Omega^+=(0,1)\times(0,1)\times(0,1)\times(0.5,1)$ and $\Omega^-=(0,1)\times(0,1)\times(0,0.5)$. The relative permittivity in Ω^+ and Ω^- are chosen to be $\varepsilon_r=1,3$, respectively. In this domain, it is assumed that the electric field is of the form $\mathbf{E}(\mathbf{r},t)=\hat{y}\{2(t+\frac{z-z_0}{c})/\tau^2exp[-(t+\frac{z-z_0}{c})^2/\tau^2]+2R(t-\frac{(z-0.5)}{c}+\frac{z-z_0}{c})/\tau^2exp[-(t-\frac{(z-0.5)}{c}+\frac{z-z_0}{c})^2/\tau^2]\}$, and $\forall \mathbf{r}\in\Omega^-$ the electric field is $\mathbf{E}(\mathbf{r},t)=\hat{y}2T(t+\frac{z-0.5}{c}\sqrt{3}+\frac{z-z_0}{c})/\tau^2exp[-(t+\frac{z-0.5}{c}\sqrt{3}+\frac{y-z_0}{c})^2/\tau^2]$ where $R=\frac{1-\sqrt{3}}{1+\sqrt{3}}, T=\frac{2}{1+\sqrt{3}}, z_0=5.5$ and $\tau=3.15\times10^{-9}s$. All other parameters, viz., distribution of nodes, overlap, definition of spatial basis functions and temporal basis functions, time step size, etc, are identical to those used earlier and as before the L^2 error norm is evaluated at $5\times5\times5$ uniformly distributed sample points. The results shown in Figure 4.13 also demonstrate the convergence of TDGFEM solver in 3D piecewise homogeneous domain.

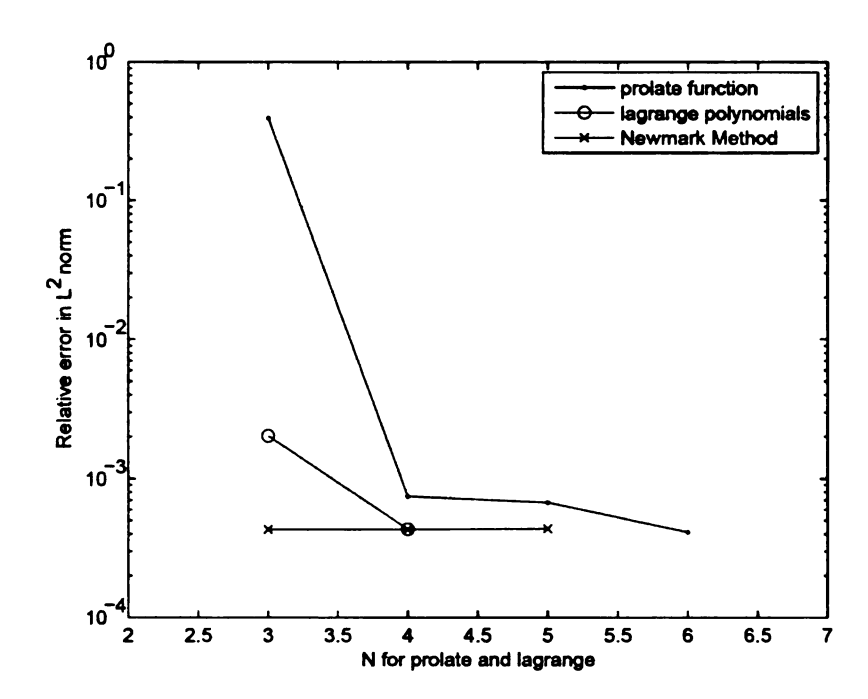


Figure 4.12. Convergence of different temporal scheme in 3D homogeneous problem

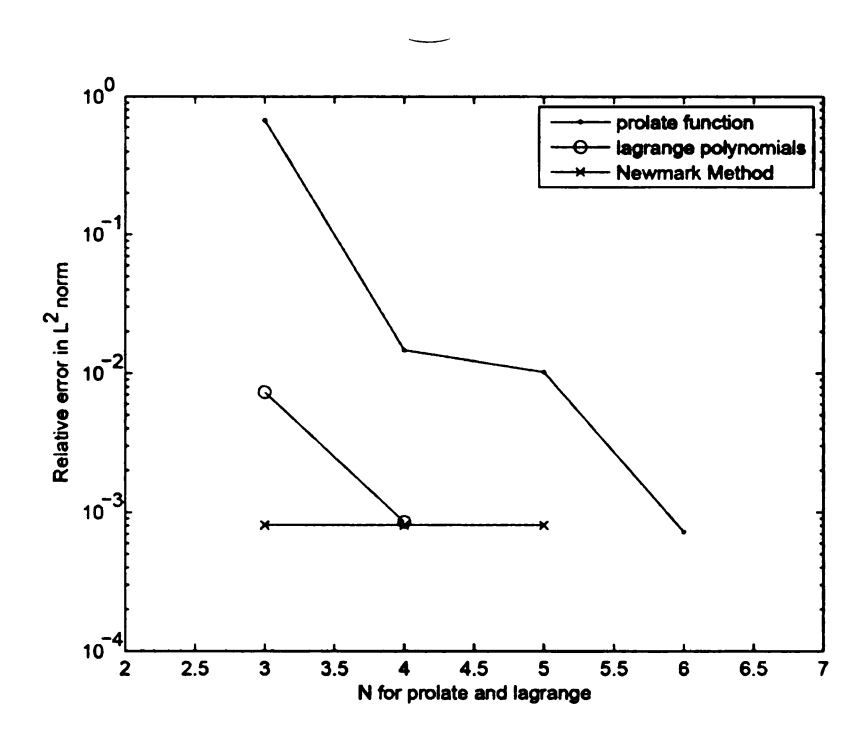


Figure 4.13. Convergence of different temporal scheme in 3D inhomogeneous problem

Next, we will demonstrate the feasibility of the time domain solver for scattering from PEC sphere. The radius of the PEC is 0.45 and the open domain is truncated by a concentric sphere with radius 0.65. In this domain, it is assumed that the incident electric field is of the form $\mathbf{E}(\mathbf{r},t)=\hat{y}2(t+\frac{x-x_0}{c})/\tau^2exp\{-(t+\frac{x-x_0}{c})^2/\tau^2\}$ where $x_0=7.5$ and $\tau=2.57\times 10^{-9}s$. The solution is solved by imposing the analytical total electric field as Dirichlet boundary condition. The parameters of spatial basis are $h=0.57\lambda$ and p=3. The time step size is $\Delta t=9.52\times 10^{-11}s$. All other parameters, viz., distribution of nodes, overlap, definition of spatial basis functions and temporal basis functions, etc, are identical to those used earlier. The L^2 error norm is evaluated at $13\times 13\times 13$ uniformly distributed sample points. The relative error is 1.1e-2. ?? shows analytical and numerical results at location (0.3, 0.3, 0.3). As shown, the result is good.

Next, iterative solver is implemented in the time domain GFEM solver. Considering a homogeneous rectangular computational domain $\Omega = (0,1)^2$ with boundary $\Gamma = \bigcup_i^4 \Gamma_i$ where $\{\Gamma_1 : \mathbf{r} \in 0 \times (0,1)\}$, $\{\Gamma_2 : \mathbf{r} \in (0,1) \times 1\}$, $\{\Gamma_3 : \mathbf{r} \in 1 \times (0,1)\}$, $\{\Gamma_4 : \mathbf{r} \in (0,1) \times 0\}$. In this domain, it is assumed that the electric field is of the form

$$\mathbf{E}(\mathbf{r},t) = \hat{y}2(t + \frac{x - x_0}{c})/\tau^2 exp\{-(t + \frac{x - x_0}{c})^2/\tau^2\}$$
 (4.28)

where $x_0 = 5.5$ and $\tau = 3.15 \times 10^{-9} s$. The solution to (4.1) is solved by imposing the analytical solution as Neumann boundary condition. In this experiment, as before, all nodes are distributed uniformly, and rectangular patches are used. The size of each patch is chosen to be 1.5 times the distance between the nodes. The weight functions $W_i(\mathbf{r})$ is a tensor product rooftops, and the local approximation function $v_{i,m}(\mathbf{r})$ and $v_{i,n}(\mathbf{r})$ are tensor product of Legendre polynomials. The parameters of spatial basis functions are $h = 0.38\lambda$ and p = 3. APSW functions are used for as temporal basis. The half width of prolate function p and the number of sample points for extrapolation N_{samp} are 6 and 4, respectively. The time step size is

 $\Delta t = 2.33 \times 10^{-11} s$. Iterative solver is used and

$$\frac{|[\mathbf{Z}]_0\{\mathbf{I}\}_i - \{\tilde{\mathbf{V}}\}|}{|\{\tilde{\mathbf{V}}\}|} < 1e^{-8} \tag{4.29}$$

is used as the ending criteria of the iterative solver. Figure 4.14 show the numerical results with relative error 1.4^{-3} . Figure 4.15 show the number of iterative steps in each time step. From the figure we can see that at the first few time steps, the numbers of iterative steps are large and then decrease as expected. For the first few time steps, the error of initial guess is large. When the initial guess is getting more and more accurate, the number of iterative steps decreases.

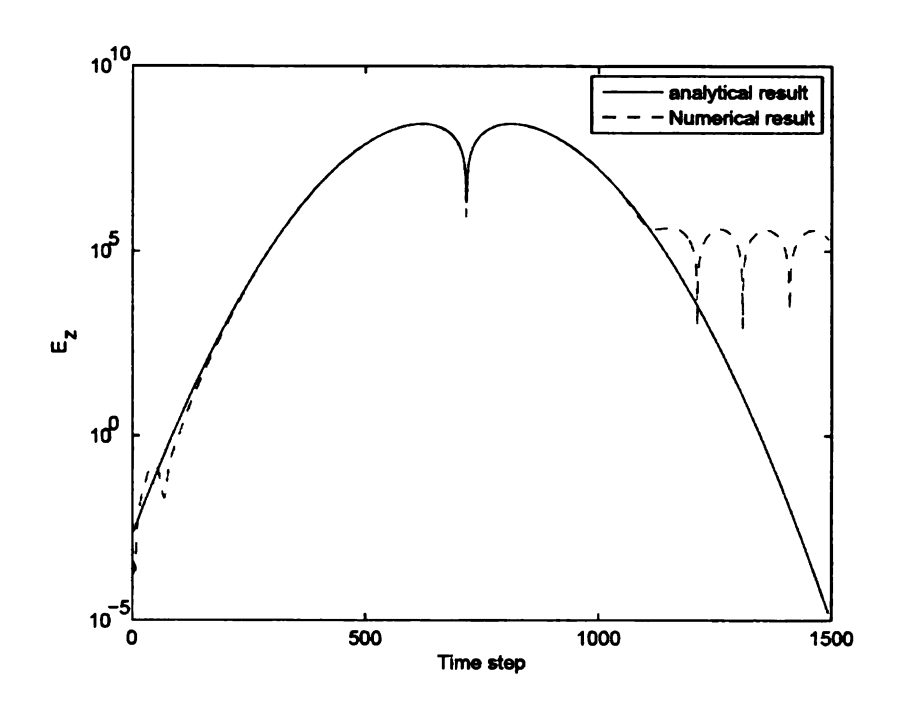


Figure 4.14. Error with iterative solver

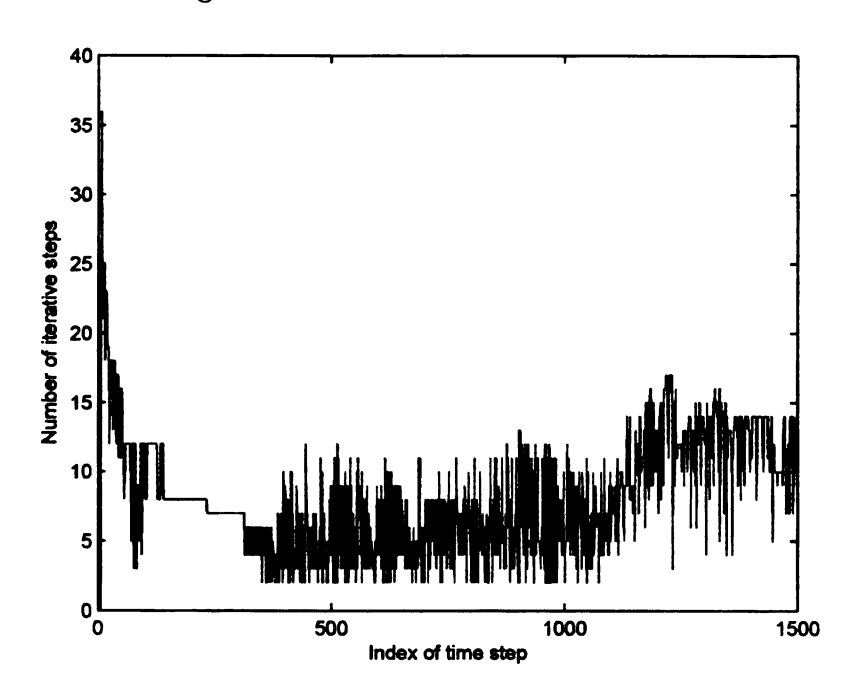


Figure 4.15. Number of iterative steps in each time step

CHAPTER 5

CONCLUSION AND AREAS FOR FUTURE WORK

Generalized finite element method (FEM) is a generalization of the classical finite element method. As a partition of unity-based solver, GFEM solver simplifies mesh generalization and enlarges the local approximation function space. At the same time, it maintains the h-, p- and hp- convergence in the computation domain. Vector GFEM solver can be developed in inhomogeneous domain to simulate the field which is divergence free and satisfy the continuity requirements on the material interface. This research has proved the convergence of the solver mathematically and demonstrated it in two dimension and three dimension simulations. We can solve wave equation with every boundary conditions encountered in the EM simulation for close domain and open domain. We also have developed an extension of GFEM solver to simulate the transient field. SVD-based preconditioner is utilized to solver the problem of the high condition number of the linear system when the high order numerical solver is utilized.

A summary of most important contributions in this research follows:

- Implementation of Nitsche's method to impose the essential boundary condition in GFEM solver. Convergence of the scalar and vector GFEM solver with this method is demonstrated in both 2D and 3D simulation.
- Development of the first hybrid GFEM-BI technique that enables the truncation of the computational domain, and demonstrated its h, p convergence properties. We have specified the manner in which different types of boundary integrals may be incorporated into the simulations. Validating the proposed technique for scattering from more complex shapes necessitated the development of GFEM-PML techniques.

- Development of an extension of GFEM to enable application to vector electromagnetic problems in piecewise homogeneous domain with smoothly curved interface. Basis functions can simulate the divergence free field which satisfy all the continuity requirements on the material interface. The convergence of this spurious-free solver is proved mathematically and demonstrated in 2D and 3D simulation.
- Application of GFEM solver to the problem where the geometry has singularity. The eigenfunction of the singular structure is used in local approximation.
 The advantage of GFEM solver is demonstrated compared with classical FEM solver.
- Development of time domain GFEM method for solving time domain differential equations. The method uses different kinds of high order time stepping scheme including Approximate prolate spheroidal wave functions. The accuracy of the solver is demonstrated in EM simulation in both 2D and 3D, homogeneous and inhomogeneous domain.
- Stability analysis of general high order time stepping solver are proposed and demonstrated with APSW-based time stepping schemes.
- Development of the svd-based preconditioner to high order numerical solver.
 The error bound and cost of this method is derived. We demonstrated that when the condition of the resulting system is improved dramatically, the accuracy of the solver are almost the same.

It also found that GFEM solver has the following advantage/disadvantage compared with classical FEM solver

Advantage:

• The mesh generation of GFEM is simpler than the classical FEM. The nodes's location and patches's size and shape can be chosen randomly. The edge of

patch is not necessary to conformal to the boundary of computation domain.

• A broader class of functions can be implemented to simulate the field in GFEM. When the same accuracy is required, GFEM solver results in smaller linear system. When simulating the fields, regular basis function in classic FEM is not as efficient as special basis functions in GFEM such as the eigenfunction-based basis function around the geometric singularity and the planewave-based basis function in a very smooth region. Though in FEM, singular basis function is also developed around the geometric singularity, there is limitation in the size of the mesh of singular basis function.

Disadvantage:

- It's more expensive to integrate the basis function and its derivative in GFEM
 when evaluating the matrix elements. Compared with the analytical integration in FEM, numerical integration in GFEM results in an additional burden.
 But the burden can be elevated when the nodes are distributed uniformly with
 the same shape and size of patches.
- Implementation of geometry information is more expensive in GFEM. In FEM, implementation of information of mesh is straightforward. In GFEM, more procedure is necessary to utilize the mesh information to GFEM solver.

Until now, vector GFEM solver has been developed for electromagnetic simulation with simple structure. Application of the technology to realistic problem implies the further research along the following which is necessary:

 Planewave-based basis function is much more efficient than the polynomials in the region where fields are smooth which has been demonstrated by two dimension homogeneous results. Augmenting the function space within planewave may be practical.

- When vector GFEM solver for curved material interface has been developed and demonstrated in 2D problem. Convergence of this solver should also be demonstrated in 3D.
- Vector GFEM solver has been developed for piecewise homogeneous domain with smooth curved material interface. Considering the material interface with geometric singularity such as vertex or edge, appropriate local approximation function has not been developed. This is a challenging problem. Based on the continuity requirements, the additional function for this material interface can be constructed as the eigenfunction of PEC with the same structure.
- Given meshes that describes the structure of the electromagnetic problem, the
 geometric information easily utilized by GFEM solver should be extracted from
 the mesh information. Those information should be able to be implemented
 by GFEM solver automatically.
- High order integration in the computation domain, e.g. volume integration, and on the boundary, e.g. surface integration, need to be implemented for high order solver. The quadrature rules of such integration can be derived by geometric transformation.

APPENDICES

Vita

Chuan Lu was born in Tianjin, P.R.C, on September 16, 1979. He received the B.S. degree in electrical engineering from Tsinghua University, Beijing in 2002. He is currently pursuing the Ph.D. degree in the Department of Electrical and Computer Engineering at the Michigan State University. Since 2002, he has been a Research Assistant at the Michigan State University. His research interests are in area of computational electromagnetics, especially differential equation-based numerical solver such as generalized finite element method.

A list of Chuan Lu's recent articles is given below:

Journal papers:

- 1. C. Lu and B.Shanker, "Analysis of complex structures using Generalized Finite Element Method," *IEEE Transactions on Antenna and Propagations*, In preparation.
- 2. O. Tuncer, C. Lu, B. Shanker and L. C. Kempel, "Dispersive Analysis of Vector Generalized Finite Element Method," *IEEE Transactions on Antenna and Propagations*, In preparation
- 3. C. Lu and B.Shanker, "Transient Analysis of Electromagnetic Fields using the Generalized Finite Element Methods," *IEEE Transactions on Antenna and Propagations*, Submitted.
- 4. **C. Lu** and B.Shanker, "Generalized Finite Element Method for Vector Electromagnetic Problems," *IEEE Transactions on Antenna and Propagations*, vol. 55, Issue 1, pp. 1369-1381, 2007.
- 5. C. Lu and B.Shanker, "Development of Hybrid Boundary Integral-Generalized (Partition of Unity) Finite Element Solvers for the scalar Helmholtz Equation," *IEEE Transactions on Magnetics*, vol. 43, Issue 3, March 2007 Page(s):1002 1012
- 6. Haixiang Cao, Lv Chuan, Jianguo Jiang and Tamasi, "Analysis of Power Loss and Choice of Parameter to over voltage-limited filter for PWM AC Inverter controlled motor," Transactions of China Electrotechnical Society, 2003

Conference papers:

- O. Tuncer, C. Lu, N. V. Nair, B. Shanker and L. Kempel, "Analysis of Error Propagation in Vector Generalized Finite Element Methods," *Internation Con*ference on Electromagnetics on Advanced Applications, Torino, Italy, September 2007
- 2. N. V. Nair, C. Lu, B. Shanker, "Differential and Integral Equation Solvers based on Generalized Moments and Partitions of Unity," *Internation Conference on Electromagnetics on Advanced Applications*, Torino, Italy, September 2007

- 3. C. Lu and B.Shanker, "Analysis of complex structures using Generalized Finite Element Method," North American Radio Science Meeting URSI-CNC/USNC, Ottawa, ON, Canada, 2007
- C. Lu and B.Shanker, "Transient Analysis of Electromagnetic Fields using the Generalized Finite Element Methods," North American Radio Science Meeting URSI-CNC/USNC, Ottawa, ON, Canada, 2007
- O. Tuncer, C. Lu, B. Shanker and L. C. Kempel, "Dispersive Analysis of Vector Generalized Finite Element Method," North American Radio Science Meeting URSI-CNC/USNC, Ottawa, ON, Canada, 2007
- 6. C. Lu and B.Shanker, "Development of Generalized Finite Element Method for Vector Electromagnetic Problems," *IEEE AP-S International Symposium on Antennas and Propagation and USNC/URSI, Albuquerque*, New Mexico, 2006
- 7. C. Lu, J. Villa and B. Shanker, "Application of Generalized Finite Element Method to Special Scattering Problem," *IEEE AP-S International Symposium on Antennas and Propagation and USNC/URSI*, Albuquerque, New Mexico, 2006
- 8. C. Lu, B. Shanker, E. Michielssen, "Development of Time Domain Generalized Finite Element Method for Vector Electromagnetic Problems," *IEEE AP-S International Symposium on Antennas and Propagation and USNC/URSI*, Albuquerque, New Mexico, 2006
- 9. H. Huang, C. Lu and B. Shanker, "Cartesian Harmonics and Fast Computation of Potentials of the Form," *IEEE AP-S International Symposium on Antennas and Propagation and USNC/URSI*, Albuquerque, New Mexico, 2006
- Z. Zeng, K. Arunachalam, C. Lu, B. Shanker, and L. Udpa, "Element-free Galerkin method in modeling microwave inspection of civil structures," Digest Book of the 12th Biennial IEEE Conference on Electromagnetic Field Computation-CEFC, Florida, USA, Apr.-May 2006
- 11. C. Lu and B.Shanker, "Development of Hybrid Boundary Integral-Generalized (Partition of Unity) Finite Element Solvers for Scalar Problems," *IEEE AP-S International Symposium on Antennas and Propagation and USNC/URSI*, Washington, DC, 2005
- 12. C. Lu and B.Shanker, "Solving Boundary Value Problems Using the Generalized (Partition of Unity) Finite Element Method," *IEEE AP-S International Symposium on Antennas and Propagation and USNC/URSI*, Washington, DC, 2005
- C. Lu and B.Shanker, "Towards the Development of Vector Generalized (Partition of Unity) Finite Element Method," IEEE AP-S International Symposium on Antennas and Propagation and USNC/URSI, Washington, DC, 2005

- 14. L. Chuan and B.Shanker, and L. Kempel, "Partition of Unity methods in electromagnetics," *Proceedings of the URSI-EM Theory Symposium*, p. 331, 2004.
- 15. Deng Wen; Lv Chuan; Jiang Jianguo; Huang Lipei; Tamai Shinzo, "Filter design of restraining over-voltage and bearing current in induction motor fed by PWM inverter," TENCON '02. Proceedings. IEEE Region 10 Conference on Computers, Communications, Control and Power Engineering, 2002

Bibliography

- [1] J. M. Jin, The Finite Element Method in Electromagnetics. New York: Wiley, 2002.
- [2] I. H. Shames and C. L. Dym, Energy and finite element methods in structural mechanics. Second edition. Hemisphere Publishing, New York, NY, 1984.
- [3] D. K. Gartling and J. N. Reddy, The Finite Element Method in Heat Transfer and Fluid Dynamics. CRC Press, 2001.
- [4] A. Konrad, "Vector variational formulation of electromagnetic fields in anisotropic media," *IEEE Trans. Microwave Theory Tech.*, vol. MTT-24, pp. 553-559, 1976.
- [5] B. M. A. Rahman and J. B. Davies, "Penalty function improvement of waveguide solution by finite elements," *IEEE Trans. Microwave Theory Tech.*, vol. MTT-32, pp. 922-928, 1984.
- [6] J. C. Nedelec, "Mixed finite elements in r^3 ," Numer. Meth., vol. 35, pp. 315–341, 1980.
- [7] M. L. Barton and Z. J. Cendes, "New vector finite elements for three-dimensional magnetic field computation.," J. Appl. Phys., vol. 61, pp. 3919–3921, 1987.
- [8] J. P. Webb and B. Forghani, "Hierarchal scalar and vector tetrahedra," *IEEE Trans. Magn.*, vol. MAG-29, pp. 1495–1498, 1993.
- [9] Z. J. Cendes, "Vector finite elemetrs for electromagnetic field," *IEEE Trans. Magn.*, vol. MAG-27, pp. 3958–3966, 1991.
- [10] R. D. Graglia, D. R. Wilton, and A. F. Peterson, "Higher order interpolatory vector bases for computational electromagnetics," *IEEE Transactions on An*tennas and Propagation, vol. 45, pp. 329–342, 1997.
- [11] W. Rachowicz and L. Demkowicz, "A three-dimensional hp-adaptive finite element package for electromagnetics." TICAM Report 00-04, 2000.
- [12] M. Costabel, M. Dague, and C. Schwab, "Exponential convergence of hp-fem for maxwell's equations with weighted regularization in polygonal domains," Mathematical Models and Methods in Applied Sciences, vol. 15, 2005. To Appear: paper available at http://perso.univ-rennes1.fr/monique.dauge/core/index.html.

- [13] D. Boffi, M. Costabel, M. Dague, and L. Demkowicz, "Discrete compactness for the hp version of rectangular edge finite elements." ICES Technical Report 04-29, 2004.
- [14] D.-K. Sun, L. Vardapetyan, and Z. Cendes, "Two-dimensional curl-conforming singular elements for fem solutions of dielectric waveguiding structures," *IEEE Transactions on Microwave Theory and Techniques*, vol. 53, pp. 984-992, 2005.
- [15] R. D. Graglia and G. Lombardi, "Singular higher order complete vector bases for finite methods," *IEEE Transactions on Antennas and Propagation*, vol. 52, pp. 1672–1685, 2004.
- [16] J. Jirousek and A. Venkatesh, "Hybrid-trefftz plane elasticity elements with p-method capabilities," *Int. J. Num. Meth. Eng.*, vol. 35, pp. 1443–1472, 1992.
- [17] J. S. Hesthaven and T. Warburton, "Nodal high-order methods on unstructured grids," *Journal of Computational Physics*, vol. 181, pp. 186–221, 2002.
- [18] I. Babuska and J. M. Melenk, "The partition of unity method," *International Journal for Numerical Methods in Engineering*, vol. 40, pp. 727-858, 1997.
- [19] T. Belytschko, Y. Krongauz, D. Organ, M. Fleming, and P. Krysl, "Meshless methods: An overview and recent developments," Comp. Meth. Appl. Mech., 1996.
- [20] L. B. Lucy, "A numerical approach to the testing of the fission hypothesis," *The Astronomical Journal*, vol. 82(12), pp. 1013-1024, 1977.
- [21] G. T. B. Nayroles and P. Villon, "Generalizing the finite element method:diffuse approximation and diffuse elements," *Computational Mechanics*, vol. 10, pp. 307–318, 1992.
- [22] Y. Y. L. T. Belytschko and L. Gu, "Element-free galerkin methods," International Journal for Numerical Methods in Engineering, vol. 37, pp. 229–256, 1994.
- [23] I. Babuska, U. Banerjee, and U. Osborn, Meshless and generalized FEM: A survey of some major results. Springer Verlag, 2002.
- [24] C. A. M. Duarte and J. T. Oden, "Hp clouds—an hp meshless method," Numerical Methods for Partial Differential Equations, vol. 12, pp. 673–705, 1996.
- [25] S. N. Atluri and S. P. Razek, *The Meshless Local Petrov-Galerkin(MLPG) Method.* Tech Science Press, 2002.
- [26] L. Xuan, B. Shanker, and L. Udpa, "A meshless element free galerkin method for nde applications," in *Proceedings of Appliced Computational Electromagnetics* Society, 2002.

- [27] L. Xuan, B. Shanker, Z. Zeng, and L. Udpa, "Element-free galerkin method in pulsed eddy currents," The International Journal of Applied Electromagnetics and Mechanics, vol. 19, pp. 463-466, 2004.
- [28] L. Xuan, Z. Zeng, B. Shanker, and L. Udpa, "Development of a meshless finite element model for nde applications," *IEEE Transactions on Magnetics*, vol. 40, pp. 12–20, 2004.
- [29] L. Xuan, Z. Zheng, B. Shanker, and L. Udpa, "Meshless method for numerical modeling of pulsed eddy currents," *IEEE Transaction on Magnetics*, vol. 40, pp. 3457 – 3462, 2004.
- [30] L. Chuan, B. Shanker, and L. Kempel, "Partition of unity methods in electromagnetics," in *Proceedings of the URSI-EM Theory Symposium*, p. 331, 2004. See the technical report series @ECE, Michigan State University for a full version of the paper or the lead PIs website.
- [31] Z. Zeng, L. Xuan, B. Shanker, L. Kempel, and L. Udpa, "Development of vector basis function for meshless efg method." Presented at URSI, 2003, 2003.
- [32] I. Tsukerman, "A flexible local approximation method for electro- and magnetostatics," *IEEE Transactions on Magnetics*, vol. 40, pp. 941 944, 2004.
- [33] A. Plaks, I. Tsukerman, and G. F. B. Yellen, "Generalized finite-element method for magnetized nanoparticles," *IEEE Transactions on Magnetics*, vol. 39, pp. 1436 1439, 2003.
- [34] I. Tsukerman, "Spurious numerical solutions in electromagnetic resonance problems," *IEEE Transaction on Magnetics*, vol. 39, pp. 1405 1408, 2003.
- [35] I. Tsukerman, "General tangentially continuous vector elements," *IEEE Transactions on Magnetics*, vol. 39, pp. 1215 1218, 2003.
- [36] L. Proekt, S. Yuferev, I. Tsukerman, and N. Ida, "Method of overlapping patches for electromagnetic computation near imperfectly conducting cusps and edges," *IEEE Transaction on Magnetics*, vol. 38, pp. 649 652, 2002.
- [37] L. Proekt and I. Tsukerman, "Method of overlapping patches for electromagnetic computation," *IEEE Transaction on Magnetics*, vol. 38, pp. 741 744, 2002.
- [38] Z. Zeng, B. Shanker, and L. Udpa, "Modeling microwave nde using the element free galerkin method-development of perfectly matched layers for domain truncation," in *Proceedings of the Tenth International Workshop on Electromagnetic Non-destructive Evaluation*, 2004.
- [39] T. F. M. Hara, T. Wada and F. Kikuchi, "A three dimensional analysis of rf electromagnetic fields by the finite element method," *IEEE Trans. Mag-19*, vol. 6, pp. 2417–2420, 1983.

- [40] J. P. Webb, "The finite element method for finding modes of dielectric-loaded cavities," *IEEE Trans. MTT-33*, vol. 7, pp. 635–639, 1985.
- [41] I. Bardi and O. Biro, "An efficient finite-element formulation without spurious modes for anisotropic waveguides," *IEEE Transactions on Microwave Theory and Techniques*, vol. 39, pp. 1133–1139, 1991.
- [42] M. E. K. Hayata, M. Koshiba and M. Suzuki, "Vectorial finite element method without any spurious solutions for dielectric waveguiding problems using transverse magnetic field component," *IEEE Trans. MTT-34*, vol. 11, pp. 1120–1124, 1986.
- [43] A. Konrad, "On the reduction of the number of spurious modes in vectorial finite element solution of three-dimensional cavities and waveguides," *IEEE Trans. MTT-34*, vol. 2, pp. 224–227, 1986.
- [44] S. N. Atluri and S. Shen, The Meshless Local Petrov Galerkin Method. Tech. Sci. Press, 2002.
- [45] J. M. Melenk and I. Babuska, "The partition of unity finite element method: Basic theory and applications," Comput. Methods Appl. Mech. Engr., vol. 139, pp. 289-314, 1996.
- [46] G. C. Hsiao and R. E. Klienmann, "Mathematical foundations for error estimation in numerical solutions of integral equations in electromagnetics," *IEEE Trans. Antennas Propag.*, vol. 45, pp. 316–328, 1997.
- [47] M. Griebel and M. A. Schweitzer, "Particle-partition of unity methods for pdes," SIAM J. Sci. Compt, vol. 22, pp. 853–890, 2002.
- [48] D. Shepard, "A two-dimensional interpolation function for irregularly spaced data," in *Proceeding of ACM*, p. 517?24, 1968.
- [49] C. A. Duarte, "The hp cloud method," Dissertation, 1996.
- [50] M. Griebel and M. A. Schweitzer, Meshless Methods for Partial Differential Equations. Springer Verlag, 2002.
- [51] S. Mendez and A. Huerta, "Imposing essential boundary conditions in mesh-free methods," Computer Methods in Applied Mechanics and Engineering, vol. 193, pp. 1257–1275, 2004.
- [52] J. Pitkäranta, "Boundary subspaces for the finite element method with lagrange multipliers," *Numer. Math.*, vol. 33, pp. 273–289, 1979.
- [53] J. Pitkäranta, "Local stability conditions for the babuska method of lagrange multipliers," *Math. Comput.*, vol. 35, pp. 1113–1129, 1980.
- [54] J. Pitkäranta, "The finite element method with lagrange multiplier for domain with corners," *Math. Comput.*, vol. 37, pp. 13–20, 1981.

- [55] R. Stenberg, "On some techniques for approximating boundary conditions in the finite element method," *Journal of Computational and Applied Mathematics*, vol. 63, pp. 139–148, 1995.
- [56] L. F. Canino, J. J. Ottusch, M. A. Stalzer, J. L. Visher, and S. M. Wandzura, "Numerical solution of the helmholtz equation in 2d and 3d using a high-order nystrm discretization," J. Comput. Phys., vol. 146, pp. 627–663, 1998.
- [57] W. C. Chew, Waves and fields in inhomogeneous media. New York: IEEE Press, 1995.
- [58] W. C. Chew and W. H. Weedon, "A 3d perfectly matched medium from modified maxwell's equations with stretched coordinates," *Microw. Opt. Technol. Lett.*, vol. 7, pp. 599-604, 1994.
- [59] Y. Saad, Iterative Methods for Sparse Linear Systems. New York: PWS Publishing Company, 1996.
- [60] V. Rokhlin, "Rapid solutions of integral equations of scattering theory in two dimensions," J. Comput. Phys., vol. 86, pp. 414–439, 1990.
- [61] R. F. Harrington, *Time Harmonic Fields in Electromagnetics*. IEEE Press Series on Electromagnetic Wave Theory, Wiley-IEEE Press, 2001.
- [62] J. A. Stratton, *Electromagnetic Theory*. New York, New York: McGraw-Hill, 1941.
- [63] C. Lu and B. Shanker, "Development of hybrid boundary integral-generalized (partition of unity) finite element solvers for the scalar helmholtz equation," technical report, Michigan State University, 2005. Submitted to IEEE Magnetics.
- [64] J. A. Chatterjee and J. L. Volakis, "Computation of cavity reasonances using edge-based finite elements," *IEEE Transactions on Microwave Theory and Techniques*, vol. 40, pp. 2106–2108, 1992.
- [65] K. S. Kunz and R. J. Luebbers, The Finite-Difference Time-Domain Method in Electromagnetics. CRC, 1993.
- [66] L. E. R. Petersson and J. M. Jin, "Analysis of periodic structures via a time-domain finite-element formulation with a floquet abc," *IEEE Transactions on Antennas and Propagation*, vol. 54, pp. 933-944, 2006.
- [67] Z. Lou and J. M. Jin, "A novel dual-field time-domain finite-element domain-decomposition method for computational electromagnetics," *IEEE Transactions on Antennas and Propagation*, vol. 54, pp. 1850–1862, 2006.
- [68] Z. Lou and J. M. Jin, "Modeling and simulation of broad-band antennas using the time-domain finite element method," *IEEE Transactions on Antennas and Propagation*, vol. 53, pp. 4099–4110, 2006.

- [69] D. S. Weile, G. Pisharody, N.-W. Chen, B. Shanker, and E. Michielssen, "An exponentially convergent scheme for the solution of the time-domain integral equations of electromagnetics," *IEEE Trans. Antennas Propagat.*, 2004.
- [70] J. J. Knab, "Interpolation of band-limited functions using the approximate prolate series," *IEEE Trans. Inform. Theory*, vol. IT-25, pp. 717-720, 1979.
- [71] C. Lu and B. Shanker, "Generalized finite element method for vector electromagnetic problems," tech. rep., Michigan State University, 2005.
- [72] J. A. Cadzow, "Extrapolation procedure for band-limited signals," *IEEE Trans. Acoust.*, Speech, Singal Processing, vol. 27, pp. 4–12, 1979.
- [73] C. Lu and B. Shanker, "Generalized finite element method for vector electromagnetic problems," *IEEE Transaction on Antennas and Propagation*, vol. 55, pp. 1369–1381, 2007.

